UILU-ENG-74-2020

CIVIL ENGINEERING STUDIES

HYDRAULIC ENGINEERING SERIES NO. 30

TURBULENT JETS IN CROSSING PIPE FLOW

by
A. M. GER and E. R. HOLLEY

Sponsored by
NATIONAL SCIENCE FOUNDATION
RESEARCH GRANT NSF-GK-24931

DEPARTMENT OF CIVIL ENGINEERING
UNIVERSITY OF ILLINOIS AT URBANA-CHAMPAIGN
URBANA, ILLINOIS
AUGUST 1974

UILU-ENG-74-2020

TURBULENT JETS

IN CROSSING PIPE FLOW

by

A. M. Ger and E. R. Holley

Sponsored by
National Science Foundation
Research Grant NSF-GK-24931

DEPARTMENT OF CIVIL ENGINEERING
UNIVERSITY OF ILLINOIS AT URBANA-CHAMPAIGN
URBANA, ILLINOIS
AUGUST, 1974

Abstract

TURBULENT JETS IN CROSSING PIPE FLOW

A. M. Ger and E. R. Holley
Department of Civil Engineering
University of Illinois at Urbana-Champaign

The objective of this study is to develop a mathematical model to simulate the steady flow field and associated concentration distributions resulting from a round, turbulent jet injected into a crossing pipe flow. The jet may be either buoyant or nonbuoyant. The tracer is conservative. In the developed model, the flow field is divided into three regions and each region treated separately. The three regions are flow establishment region, near field region, and far field region. Basically, the flow is treated as a jet in a crossflow in the first two regions, and as the diffusion of a passive conservative tracer in the far field region. The nonuniform velocity distribution of the crossing pipe flow is considered by letting the pipe flow velocity vary across the pipe according to a power law. The turbulence of crossflow is also taken into account by the consideration of a far field region. Also, the effects of pipe turbulence in the near field region are inherently reflected by the experimentally evaluated entrainment and drag coefficients.

The accuracy of the proposed model has been checked with the experiments. It has been found that by dividing analysis into regions a good representation of the flow field and associated concentration distributions was achieved. The near field region in which jet is active represents a very small fraction (less than 2 percent) of the total mixing distance, which is defined as the flow distance

required for the concentration distribution to become uniform within some specified tolerance. However, the initial jet mixing and the jet penetration (advection of jet away from the wall of the pipe) in the near field region are responsible for a reduction in the mixing distance compared to a simple source at the pipe wall. Defining the momentum flux ratio as the ratio of the initial momentum of the jet to momentum of the pipe flow, there exists an optimum momentum flux ratio (numerically equal to 0.0156) for which the reduction in mixing distance is maximized. The major part of the mixing is accomplished by the turbulent diffusion associated with the far field region.

Examples are given to demonstrate the application of jet injections both to discharge measurements and to the use of a pipe segment as a mixing chamber.

ACKNOWLEDGMENTS

This report is the completion report for National Science Foundation Research Grant NSF-GK-24931 entitled "Tracer Mixing for Discharge Measurements in Pipes". The support of the National Science Foundation for this research is gratefully acknowledged.

This report is essentially the same as the doctoral thesis entitled "Turbulent Jets in Crossing Pipe Flow" submitted by A. M. Ger.

TABLE OF CONTENTS

LIST OF TABLES

LIST OF FIGURES

LIST OF SYMBOLS

A	Pipe cross-sectional area; a constant
B	Dimensionless jet radius
C_D, C_t	Drag coefficients
D	Pipe diameter
D_r	Ratio of pipe to injection hole diameter
E	Entrainment
$\mathbb{F}_d$	Densimetric Froude number
F_x	x-component of drag force
F_y	y-component of drag force
I	Intercept of L vs. log σ curve
L	Dimensionless mixing distance
M	Momentum flux ratio
Q	Pipe flow rate
Q_j	Flow rate in the jet
R	Pipe radius
$\mathbb{R}$	Reynolds number
S_d	Standard error of discrepancy
U_a	Dimensionless ambient velocity
U_s	Dimensionless velocity excess
X, X_1, X_2	Dimensionless coordinates
Y	Dimensionless coordinate
a_t	Attenuation of the recorder
b	Nominal jet radius

b_e	Nominal jet radius at the end of the flow establishment region
c	Concentration of tracer
$\overline{c}$	Cross-sectional average concentration
c_p	Background concentration
c_s	Centerline concentration
d	Injection hole diameter
e_1, e_2, e_3	Mass diffusivities
$\bar{\bar{e}}_2$	Average radial mass diffusivity
f	Friction factor
f_i	i-th component of body force
g	Gravitational acceleration
k	Velocity ratio
k_r	Mass diffusivity
m_ℓ	Total mass loss
p	Pressure
q	Injection rate
s	Coordinate along the jet trajectory
t	Travel time
u, u_1	Axial velocity
u_a	Ambient velocity
u_e	Entrainment velocity
u_j	Jet centerline velocity
u_o	Injection velocity

u_s	Centerline velocity excess
$\bar{\bar{u}}$	Average pipe velocity
u_*	Shear velocity
u_i'	Turbulent velocity fluctuations in i-th direction
x, x_1, x_2, x_3	Coordinates
x_m	Mixing distance
y	coordinate
α, α_*	Entrainment coefficients
δ_o	Specific weight of the injection solution
δ	Actual time-mean deflection recorded
δ_*	Apparent time-mean deflection recorded
ε	Eddy viscosity
$\bar{\bar{\varepsilon}}$	Average eddy viscosity
η	Diffusivity ratio
θ	Jet deflection angle
θ_e	Jet deflection angle at end of flow establishment region
θ_o	Initial jet deflection angle
λ	Turbulent Schmidt number
μ	Viscosity
ρ	Local jet density
ρ_a	Ambient density
ρ_o	Injection solution density
σ, σ_k	Standard deviation; periphery of control volume
σ_c	Standard deviation of concentration

$\Delta x_1, \Delta x_2, \Delta x_3$ Step sizes

$\Delta\delta$ Difference in specific weight of the injection solution and the ambient fluid

$\Delta\rho$ Density disparity between the jet and the ambient fluid

$\Delta\rho_0$ Initial density disparity

$\Delta\rho_s$ Centerline density disparity

1. INTRODUCTION

1.1. Definition of the Problem

Several of the possible means of discharge measurement in a pipe require either a significant head loss or interruption of service. The techniques which produce a head loss may not be economical since a portion of the available head is wasted. On the other hand, it may not be feasible to interrupt service very often, so that techniques requiring this interruption could be used only occasionally. Thus, a measurement technique which is econimical and which requires no interruption of flow was needed. Tracer techniques were introduced because they meet both requirements [Clayton, et al., 1968].

The basis of the tracer technique with a continuous, steady injection rate is the mass balance of the tracer which is injected into the flow. By knowing the mass injection rate, M_{IN}, and measuring the concentration at a section after the tracer becomes "uniformly" mixed with the flow, the discharge Q in the pipe can be determined [Bureau of Reclamation, 1966]:

$$M_{IN} = M_{OUT} \tag{1-1}$$

$$Qc_p + qc_o = (Q+q)\,\overline{c} \tag{1-2}$$

or rearranging,

$$Q = q\,(c_o-\overline{c})/(\overline{c}-c_p) \tag{1-3}$$

where q is the injection volume flux rate (or discharge), c_0 is the concentration (mass of tracer/unit volume of solution) of the tracer in the injected fluid, and $\overline{c}$ is the concentration (mass of tracer/unit volume of solution) of the tracer after adequate mixing takes place. In Eq. 1-3, the tracer is assumed to be conservative.

1.1.1. Mixing Distance

The distance required for the adequate mixing to take place is known as the "mixing distance." By measuring the concentration at a distance equal to or greater than the mixing distance, it is sufficient to make the measurement at only one point in the cross section, i.e., one measurement at any point in the cross section is then representative of the average concentration. Thus, prediction of the mixing distance constitutes a most critical part of the tracer techniques.

The knowledge of the mixing distance also has direct applications in several other industrial and ecological control processes. For example, the chlorination of a water supply can be performed in a segment of the main pipe rather than in a separate mixing facility. The mixing distance will determine the length of the main pipe required before any branching in order to prevent excessive or deficient chlorination in the individual branches. Similarly, in the treatment of industrial plant effluents with chemical additives, neutralization of ecologically harmful waste material can be accomplished in a segment of the outlet pipe. Again, the mixing distance will determine the length of pipe needed before discharge into the atmosphere or a body of water.

In much of this report, the injected fluid is called a "tracer" simply for convenience. All of the considerations related to mixing apply equally to injections for discharge measurements or for any other purpose.

1.1.2. Type of Injection

There have been several analytical and laboratory investigations for some injection systems in straight pipes with fully-established turbulent pipe flow (Chapter 2). For some situations, these studies [Clayton, et al., 1968; Clayton and Evans, 1967; Evans, 1968; Filmer and Yevdjevich, 1966] allow an accurate prediction of the mixing distance. However, due to several difficulties involved, many of the situations investigated in the analytical and laboratory studies cannot reasonably be applied in field or prototype situations. Among these difficulties are (a) the injection system (e.g., a ring source or a symmetrical centerline injection) may not be suitable for field measurements and (b) the pipeline may not have a uniform straight section as long as the required mixing distance for a specific type of injection.

The simplest possible set up (and one which is suitable for field measurements as well as laboratory measurements) is a single-point injection at the pipe wall and a single-point sampling, also at the pipe wall. However, for a "simple source" at the wall, the mixing distance is approximately 200 pipe diameters for a smooth pipe and a Reynolds number of about 100,000. ("Simple source" is used to refer to a tracer source issuing into the pipe flow with no initial mixing.) Any reduction in the mixing distance may increase the applicability of tracer techniques in discharge measurements and provide a greater opportunity for using segments of existing pipes for accomplishing mixing. A turbulent jet, with or without buoyancy, located at the wall of the pipe, rather than a simple source, may be used to inject the tracer (or other substance) and thereby reduce the mixing distance. A jet perpendicular to the pipe wall will transport the injected fluid away from the wall and cause some initial mixing. This initial mixing and the transport of the injected fluid away from the pipe wall decrease the amount of mixing which must be accomplished by the pipe flow and therefore reduce the mixing distance.

If the behavior of the jet is partially governed by a density disparity between the jet and the ambient fluid, the jet is said to be buoyant. A convenient parameter to assess the importance of buoyancy in jet flows is the jet densimetric Froude number $\mathbb{F}_d$ defined as:

$$\mathbb{F}_d = u_o/(|\Delta\rho| gd/\rho_a)^{1/2} \tag{1-4}$$

where u_o is the jet injection velocity, $\Delta\rho$ is the density disparity between the jet and the ambient fluid, ρ_a is the ambient density, g is the local acceleration of gravity, and d is the diameter of the injection hole. For large $\mathbb{F}_d$ (>>1), the jet is considered to be inertially dominated with negligible influence of buoyancy. For $\mathbb{F}_d$ near unity buoyancy becomes the dominating aspect of the flow. Should $\mathbb{F}_d$ be in the order of unity at the injection point, it would be hard to consider the effluent as a jet. If buoyancy is to be considered as helping to transport the injected fluid away from the pipe wall, then the injection should be made vertically from the top of the pipe if the injected fluid is heavier than the ambient or vertically from the bottom if the injected fluid is lighter.

1.2. The Objectives of This Study

The general objective of this study was to investigate the behavior of a fluid injected as a turbulent jet, with or without buoyancy, perpendicular to the pipe wall into fully-established turbulent flow in a pipe. The results were used to evaluate the use of turbulent jets as tracer sources for discharge measurements in pipes and as means for accomplishing mixing within a pipe flow. More specifically, the individual objectives are

1. To develop a mathematical model which would provide a solution for the behavior of the injected fluid (Chapter 3).
2. To conduct experiments to check the accuracy of the mathematical model (Chapters 4 and 5).
3. To experimentally observe and evaluate the reduction in mixing distance due to use of a jet, with or without buoyancy, in comparison to mixing distance due to other types of injection systems (Chapter 5).
4. To make recommendations for use of this injection technique in field applications (Chapter 6).

2. PHYSICAL PROCESS AND LITERATURE REVIEW

2.1 General Description of the Flow Field

2.1.1 Similarity to Jet in a Crossflow

The behavior of either a nonbuoyant or a buoyant jet injected perpendicularly from the pipe wall into a crossflow in a pipe is similar in many respects to that of a jet injected into a uniform, unconfined crossflow. The differences resulting from the existence of the confining boundary (the pipe wall) are

1. The pressure gradient along the pipe axis.
2. The nonuniform velocity distribution of the crossflow in a pipe.
3. The ambient turbulence.
4. The limited supply of ambient flow for potential entrainment by the jet.

2.1.2 The Flow Field

As a jet enters a crossflow in a pipe, the jet behaves initially as if it were in a stagnant ambient fluid since the crossflow velocity is small in comparison with the jet velocity. However, as the jet penetrates into the crossflow, the interaction of the jet and the crossflow causes the jet to be deflected in the direction of the crossflow. The rate of deflection is dependent on the net effect of momentum and buoyancy of the jet, the pressure force on the jet, and the entrainment.

2.1.2.1 Pressure Force

There is a drag-type pressure force on the jet. On the upstream side of the jet, the crossflow is partially stagnated. On the downstream side some separation of the ambient flow takes place. Thus, the pressure around the jet continuously decreases from the upstream side of the jet to the downstream side. This change is in addition to any pressure gradient impressed by the ambient flow. Due to both effects, there is a net pressure force on the jet. Normally, the drag-type pressure force is larger than that associated with the ambient pressure gradient.

2.1.2.2 Entrainment

The shearing between the crossflow and the jet causes entrainment of crossflow by the jet. As the jet deflects, there will be a component of crossflow velocity along the jet axis and another component normal to the axis. The velocity difference between the jet velocity and the component of the crossflow velocity in the direction of the jet axis gives rise to a free-jet type entrainment. On the other hand, the normal component of the crossflow velocity generates a vortex pair in the wake behind the jet and disturbs the jet boundary. This produces strong mixing and causes further entrainment of ambient fluid.

The existence of the pipe wall places a potential limit on the supply of ambient flow for entrainment by the jet. However, as long as the volume flux of the jet is small compared to the ambient volume flux, this limitation on the supply of ambient flow is probably not significant.

2.1.3 Three Principal Flow Regions

For a round turbulent jet, with or without buoyancy, discharging through a circular hole at the wall into a fully-established turbulent pipe flow, three principal regions can be distinguished in the jet flow (Fig. 1). In the present work, these regions are identified as (a) the flow establishment region, (b) the near field region, and (c) the far field region. Basically, the transport of the tracer can be treated as a jet in a crossflow in the flow establishment and near field regions, and as the turbulent diffusion of a passive tracer in a pipe flow in the far field region. The general characteristics of each region are discussed below. Quantitative definitions for each region are given in Chapter 3 (Sections 3.2.3, 4, 5).

2.1.3.1 The Flow Establishment Region

As the jet penetrates into the fully-established turbulent pipe flow, a diffusion zone is formed around the periphery of the jet by the shear between the jet and ambient fluid. This diffusion zone grows both inward toward the jet axis and outward. Eventually at some distance along the jet axis the diffusion zone reaches the jet axis, after which the jet centerline velocity starts to decrease. The region between the jet outlet and the jet cross section where the diffusion zone reaches the jet axis is called the flow establishment region. The main

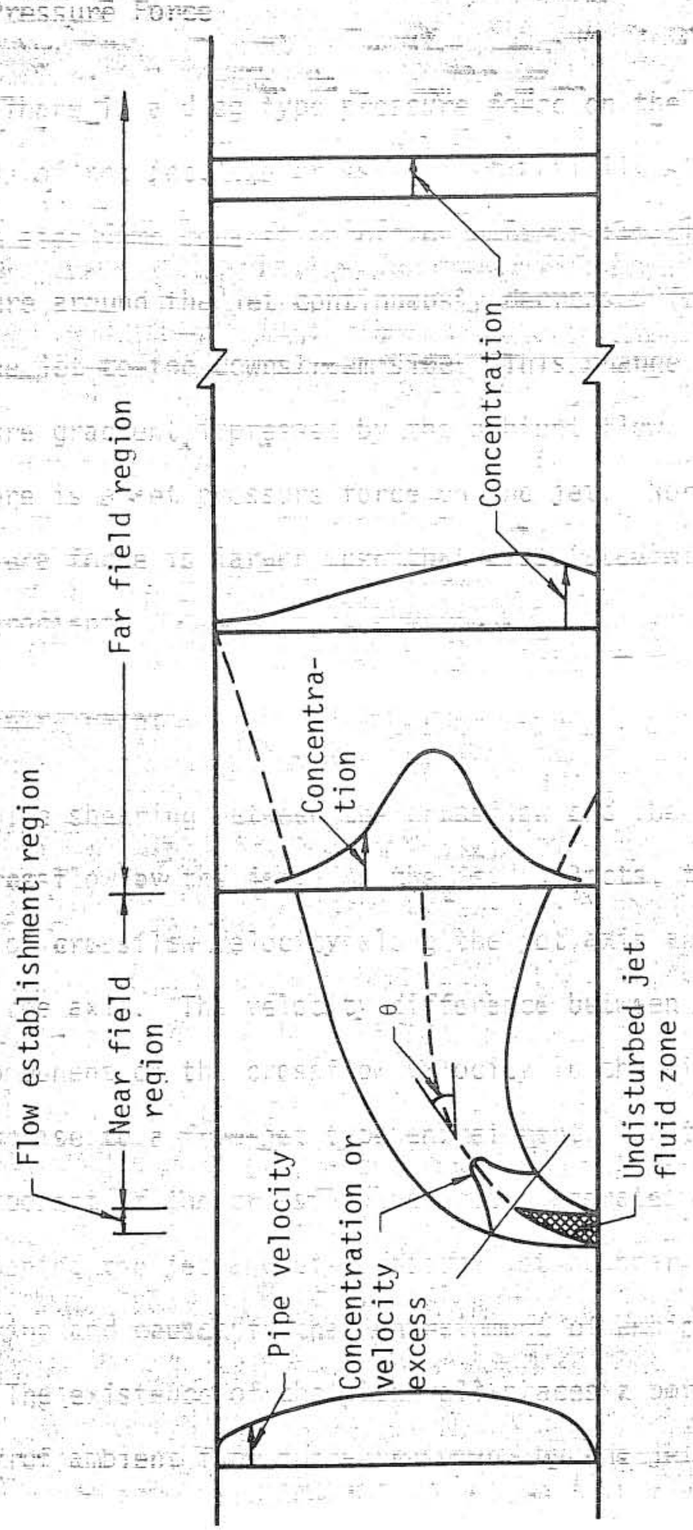

FIGURE 1: Flow regions

characteristic of this region is the undisturbed jet fluid zone (Fig. 1).

For a buoyant jet, the jet possesses a density disparity as well as a velocity excess. However, in the flow establishment region, unless the densimetric Froude number is close to unity, no appreciable influence of the density disparity is observed [Abraham, 1965].

2.1.3.2 The Near Field Region

The flow region between the end of flow establishment region and the point at which jet is practically dissipated will be called the near field region. In this region, the distributions of momentum and any density disparity each can be assumed to be self similar (Section 2.2.1). At the beginning of the near field region, the jet mixing action dominates the transport mechanism, but the jet gradually is slowed down by the entrainment of the ambient flow (Section 2.2.2). As the jet bends over and becomes aligned with the crossflow in the pipe, the jet is eventually dissipated and the ambient flow characteristics become the dominant factors in the transport mechanism (Section 3.2.4.2).

2.1.3.3 The Far Field Region

The flow region downstream of the near field region is called as the far field region. As noted earlier, in this region, the jet is practically dissipated; there is no residual effect of the previous jet behavior other than that the initial distribution of the tracer within the pipe cross section at the beginning of this region is a result of the jet behavior in the first two regions. The behavior of the tracer in the far field region is governed by the velocity and the turbulent diffusion of the pipe flow. Due to turbulent mixing in the pipe flow, the variation in concentration of tracer within a pipe cross section continually decreases along the pipe axis and eventually the adequate mixing is achieved. The length of this region is much greater than that of the other two regions, as will be seen in Section 5.4.5.

2.1.4 Jet Penetration and the Mixing Distance

Since, in the far field region, the transport of the tracer is governed solely by the pipe flow characteristics, the length of this region for a given flow is dependent solely upon the distribution of the tracer concentration at the beginning of the region. In other words, the location of the jet center relative to the pipe center at the end of the near field region is of primary importance as far as the magnitude of the mixing distance is concerned. For jet centers located close to the pipe wall, one would expect longer mixing distances as compared to the jet center close to the pipe center based on the different mixing distances for simple sources located at the pipe wall as compared to the case for those on the pipe centerline (Section 5.5). Defining the jet penetration as the distance between the jet center at the end of the near field region and the injection side of the pipe wall, it is to be expected that there exists an optimum penetration for which the mixing distance is minimized. The penetration represents the effect of the jet characteristics on the mixing distance. In Chapter 5 (Section 5.4.1) the dependence of the jet penetration on both the jet and the pipe flow characteristics is discussed.

2.2 Jets in Crossflow

Most of the studies [Baines and Pratte, 1967; Fan, 1967; Keffer, 1969; Abraham, 1969; Keffer and Baines, 1963; Motz and Benedict, 1970; Lin, 1971; Chan and Kennedy, 1972] on turbulent jets in uniform, unconfined crossflows are semiempirical in nature. A summary of previous work is given by Fan [1967] and Chan and Kennedy [1972]. Some parts of the literature review given here have been abstracted from these previous reviews.

The mathematical models given in the literature [Fan, 1967; Abraham, 1969; Motz and Benedict, 1970; Chan and Kennedy, 1972] are Morton Type [Morton, 1959] integral approaches which require experimental determination of some unknown parameters such as the entrainment coefficient (Section 2.2.2) and the drag coefficient (Section 2.2.3). These mathematical models assume similar velocity excess profiles and density disparity profiles (if any) in the jet and result in a set of simultaneous differential equations. Solution of these equations gives the trajectory of the jet, the decay of both the velocity excess and the density disparity, and the variation in the nominal radius of the jet. The nominal radius of the jet is normally assumed to be the point where the jet velocity excess is some arbitrary fraction of the jet centerline velocity excess. The same type of definition is adopted in this study.

2.2.1 Similarity

Similarity profiles for velocity excess and density disparity distributions have often been used in the analytical treatment of the flow of a jet, after an appropriate system of coordinates was chosen [Baines and Pratte, 1967; Fan, 1967; Keffer, 1969; Chan and Kennedy, 1972; Hirst, 1972]. However, two inherent features of the flow, namely nonuniform crossflow and the variation in the entrainment around the periphery of a jet cross section, make the assumption of similarity profiles not strictly valid. Nevertheless, in this study, similarity profiles are assumed since it has been shown in previous studies that similarity assumptions produced reasonably good agreement between theoretical predictions and experimental data. The most commonly used similarity profile is the Gaussian distribution [Fan, 1967; Keffer, 1969; Keffer and Baines, 1963; Chan and Kennedy, 1972], although there is at least one case in which a "top-hat" profile has been used [Carter, 1969].

2.2.2 Representation of Entrainment

Entrainment, E, is the change in the volume flux in the jet along the jet trajectory:

$$E = \frac{dQ_j}{dx_1} \tag{2-1}$$

where Q_j is the discharge or volume flux in the jet and x_1 is the coordinate along the jet trajectory. The gradient dQ_j/dx_1 has frequently been related to a representative entrainment velocity, u_e, by

$$\frac{dQ_j}{dx_1} = 2\pi b\ u_e \qquad (2\text{-}2)$$

where b is the nominal radius of the jet, which is defined quantitatively in Section 3.2.3. Thus, by combining Eq. 2-1 and Eq. 2-2, the entrainment process can also be represented in terms of the representative entrainment velocity [Morton, 1959], u_e, as

$$E = 2\pi b\ u_e \qquad (2\text{-}3)$$

2.2.2.1 Entrainment Velocity in the Case of Stagnant Ambient Fluid

For the case of a free jet in an unbounded stagnant ambient fluid, it is well established [Morton, 1959] that

$$u_e = \alpha_* u_j \qquad (2\text{-}4)$$

where u_j is the jet centerline velocity and α_* is an entrainment coefficient. Since the ambient fluid is stagnant at infinity, u_j is also a measure of the velocity difference between the jet and ambient fluid.

2.2.2.2 Entrainment Velocity in the Case of Interacting Crossflow

For the case of a jet in a crossflow, Eq. 2-3 is normally assumed to still be valid, but the formulation of the entrainment velocity, u_e, has been the subject of much speculation. Even with all this speculation and attention to u_e, the detailed mechanisms of entrainment are among the least understood aspects of the jet in a crossflow.

As mentioned earlier, the entrainment process in the case of an interacting crossflow can be viewed as consisting of two parts; one part is due to the difference between the jet velocity and the component of the crossflow parallel to the jet, the other is due to the normal component of the crossflow.

Fan [1967] represented E in terms of the magnitude of the vector difference between the two characteristic velocities:

$$E = 2\pi b\alpha|\bar{u}_j - \bar{u}_a| \tag{2-5}$$

where $\bar{u}_j$ is the jet centerline velocity vector, $\bar{u}_a$ is the crossflow velocity vector and α is an entrainment coefficient (which is not normally the same as α_* in Eq. 2-4). He therefore had a single entrainment coefficient representing the combined effect of both aforementioned types of entrainment. In this study, the entrainment mechanism is defined according to Eq. 2-5 following Fan [1967]. This choice is due merely to the convenience of the form and the success which Fan had for the situations which he investigated.

Other investigators have used other representations for u_e. For example, Keffer and Baines [1963] expressed u_e in terms of the scalar difference of the jet centerline velocity, u_j, and the ambient velocity, u_a. Others [Lin, 1971; Platten and Keffer, 1968; Keffer, 1962; Hoult et al., 1969] expressed u_e in terms of a linear combination of the axial and normal components of the vector difference between the jet and the crossflow velocities. Thus, they ended up with two coefficients representing the free-jet type and crossflow-type entrainments. Hirst [1972] later assumed that the entrainment into the jet in a crossflow depends on the local densimetric Froude number. He obtained a relation for u_e involving four entrainment coefficients.

The tendency in the past work has been to consider the entrainment coefficients as constant along the jet trajectory. Abraham [1965] argued that the entrainment coefficient could not be assumed constant, particularly in solving buoyant jet problems. He pointed out that the behavior of the vertical buoyant jet in a homogeneous stagnant environment was initially like a nonbuoyant jet and later a plume. Since jets and plumes have different entrainment coefficients, he suggested an approximate method to account for this variation in the entrainment coefficient. Fan and Brooks [1966] later showed that the use of a constant entrainment coefficient produced as good a fit to data as the use of Abraham's method. In this study, therefore, the entrainment coefficient, α, is assumed to be constant along the jet trajectory.

2.2.3 Drag Force on the Jet

Several of the investigators cited above [Lin, 1971; Platten and Keffer, 1968; Keffer, 1962; Hoult et al., 1969] have not considered the influence of the drag in their solutions for the behavior of the jet in a crossflow. Their main argument for omitting it was that there is no significant effect of the drag on the jet after it becomes nearly parallel to the crossflow.

Some investigators [Fan, 1967; Abraham, 1969; Motz and Benedict, 1970; Chan and Kennedy, 1972], on the other hand, did include the effects of both the drag and the entrainment in their analysis. They treated the jet as an obstruction in the crossflow. The drag then was represented as

$$dF = C_t \rho_a u_a^2 b dx_1 \tag{2-6}$$

where dF is an increment of drag force acting on the elemental jet volume with a nominal radius b and thickness dx_1 along the jet axis, ρ_a is the ambient density, u_a is the ambient velocity, and C_t is the drag coefficient.

Abramowich [1963] also treated the jet as an obstruction in the crossflow and used the same type of definition for the drag as given in Eq. 2-6. But, unlike other investigators, he did not include the effect of entrainment in his treatment. Therefore, he obtained drag coefficients which are much larger than those coefficients observed by others because the drag coefficients in his representation also reflect the effect of entrainment.

In this study, the concept of a jet being an obstruction is employed. Furthermore, C_t in Eq. 2-6 is replaced by $C_D \sin^2 \theta$ after Abramowich [1963], where θ is the jet deflection angle (Fig. 1) and C_D is a drag coefficient which is assumed to be constant along the trajectory of the jet. Thus, the following relation for the drag force is used:

$$dF = C_D \rho_a u_a^2 \sin^2 \theta \ b \ dx_1 \tag{2-7}$$

The quantity $u_a \sin \theta$ is the component of the ambient flow normal to the jet axis. The form of Eq. 2-7 assures that dF approaches zero as the jet becomes aligned with the ambient flow. This fact and the previous success with the use of expressions such as Eq. 2-7 by other investigators are the reasons that Eq. 2-7 will be used in this study.

2.3 Turbulent Mass Diffusion in Pipe Flow

Considerations in this section relate to the far field region and are therefore concerned with pipe flow. None of the considerations relate to the mechanics of jets injected into the flow.

General treatment of the subject of turbulent diffusion may be found in Bird et al. [1960], Hinze [1959], and Monin and Yaglom [1972], among others. The mass transport equation for a tracer is obtained from considering the mass balance of the tracer. For the case of steady, established turbulent pipe flow of an incompressible fluid, the mass balance equation in cylindrical coordinates for a steady state tracer distribution becomes [Hinze, 1959]

$$\frac{\partial}{\partial x_1}(cu) = \frac{\partial}{\partial x_1}\left(e_1\frac{\partial c}{\partial x_1}\right) + \frac{1}{x_2}\frac{\partial}{\partial x_2}\left(e_2 x_2\frac{\partial c}{\partial x_2}\right) + \frac{1}{x_2^2}\frac{\partial}{\partial x_3}\left(e_3\frac{\partial c}{\partial x_3}\right) \quad (2\text{-}8)$$

where u is the axial velocity, c is the concentration of the tracer (mass/volume), and e_1, e_2, and e_3 are the turbulent mass diffusivities in x_1 (longitudinal), x_2 (radial), and x_3 (circumferential) directions. The nonuniform nature of diffusion coefficients and the axial velocity causes difficulty in analytically solving Eq. 2-8 for appropriate boundary conditions.

Many investigators have solved Eq. 2-8, which is elliptic in nature, by making assumptions in addition to those inherent in the equation. Most investigators consider the axisymmetrical case which reduces Eq. 2-8 to

$$\frac{\partial}{\partial x_1}(cu) = \frac{\partial}{\partial x_1}(e_1\frac{\partial c}{\partial x_1}) + \frac{1}{x_2}\frac{\partial}{\partial x_2}(e_2 x_2\frac{\partial c}{\partial x_2}) \qquad (2\text{-}9)$$

In Carslaw and Jaeger [1965] and Crank [1964], several analytical solutions to Eq. 2-9 have been presented for various boundary conditions using the assumption of isotropy (i.e., $e_1 = e_2$), constant diffusion coefficients, and uniform velocity distribution. These assumptions limit the potential applicability of the solutions for use in practical problems.

Neglecting the effect of axial diffusion for steady state conditions, Eq. 2-9 is further reduced to

$$\frac{\partial}{\partial x_1}(cu) = \frac{1}{x_2}\frac{\partial}{\partial x_2}(e_2 x_2\frac{\partial c}{\partial x_2}) \qquad (2\text{-}10)$$

Jordan [1961] and Bernard and Wilhelm [1950], among others, solved the above equation for a continuous centerline point source in a fully-established pipe flow. They assumed the velocity u and diffusion coefficient e_2 as constant and obtained

$$c = 1 + \sum_{n=1}^{\infty} \exp\left(-\frac{e_2\alpha_n^2 x_1}{R^2\bar{\bar{u}}}\right)\frac{J_o(\alpha_n x_2/R)}{J_o^2(\alpha_n)} \qquad (2\text{-}11)$$

where c is the concentration of the tracer normalized with respect to the cross-sectional average concentration $\bar{c}$, $\bar{\bar{u}}$ is the cross-sectional average velocity, R is the pipe radius, and α_n is the n-th positive root of

$$J_o(\alpha R) = 0 \tag{2-12}$$

Equation 2-12 is derived from the boundary condition that there be no radial mass transfer across the pipe wall. For large x_1 values ($x_1 > 60R$), the first term of the series in Eq. 2-11 approximates the series sum with more than 99 percent accuracy. Therefore, for $x_1 > 60R$, neglecting all but the first term of the series, Eq. 2-11 reduces to

$$c = 1 + \exp\left(- \frac{e_2 \alpha_1^2 x_1}{R^2 \bar{\bar{u}}}\right) \frac{J_o(\alpha_1 x_2/R)}{J_o^2(\alpha_1)} \tag{2-13}$$

Jordan [1961] also solved Eq. 2-10 for a continuously emitting axisymmetrical ring source. Assuming uniform velocity and diffusivity, he obtained

$$c = 1 + \sum_{n=1}^{\infty} \exp\left(- \frac{e_2 \alpha_n^2 x_1}{R^2 \bar{\bar{u}}}\right) \frac{J_o(\alpha_n x_2/R)\ J_o(\alpha_n R_o/R)}{J_o^2(\alpha_n)} \tag{2-14}$$

where R_o is the radius of the injection ring.

As mentioned earlier, analytical integration of Eqs. 2-9 and 2-10 is normally not possible except when uniform velocity and diffusivities are assumed. Thus, several investigators used numerical integration techniques to obtain solutions of Eqs. 2-9 and 2-10. Fahien and Smith [1955] solved Eq. 2-10 numerically, allowing both the velocity and the radial diffusifity to vary with radial position. They considered a certerline injection into a fully-established pipe flow. Evans [1966] later numerically solved Eq. 2-9 for a centerline injection into a fully-established pipe flow. He found that the effect of the term involving e_1 in Eq. 2-9 is small compared to other terms for steady state conditions and thus can be neglected for the range of Reynolds number (4×10^3 to 10^7) which he considered. Seagrave [1960], using a different mathematical technique arrived at the same conclusion. However, at small Reynolds number ($<4 \times 10^3$), Roley [1960] has shown that the magnitude of the axial diffusion becomes comparable with the magnitude of the convective transport and therefore the axial diffusion term cannot be neglected. Since transition from laminar to turbulent flow normally takes place at Reynolds numbers of approximately 2×10^3, this range of turbulent flows for which axial diffusion must be included in is relatively insignificant in many situations.

2.3.1 Turbulent Mass Diffusivity in Radial Direction

The analogy between mass and momentum transport in turbulent pipe flow is commonly used to relate the turbulent mass diffusivity to flow characteristics. Values so obtained for the radial mass diffusivity have been compared with data as discussed below.

Using the logarithmic velocity distribution and the linear shear stress variation in the radial direction, it can be shown [Schlichting, 1968] that the eddy viscosity (or turbulent momentum diffusivity), ε, is

$$\varepsilon = K u_* R \left(\frac{x_2}{R}\right)\left(1 - \frac{x_2}{R}\right) \qquad (2\text{-}15)$$

where K is von Karman's constant, u_* is the shear velocity, x_2 is the radial distance, and R is the radius of the pipe. Sometimes $\bar{\bar{\varepsilon}}$, the cross-sectional average value of ε, is used:

$$\bar{\bar{\varepsilon}} = K u_* R/6 \tag{2-16}$$

Substituting

$$u_* = \bar{\bar{u}} \sqrt{f/8} \tag{2-17}$$

where $\bar{\bar{u}}$ is the cross-sectional average velocity and f is the Darcy-Weisbach friction factor, and assuming K = 0.4, Eq. 2-16 becomes

$$\bar{\bar{\varepsilon}} = 0.0236 \sqrt{f}\, \bar{\bar{u}}\, R \tag{2-18}$$

The turbulent Schmidt number λ represents the ratio of turbulent diffusivity of momentum ε to turbulent diffusivity of mass e_2, i.e.,

$$\lambda = \varepsilon/e_2 \tag{2-19}$$

Thus, from Eqs. 2-15, 2-16, and 2-19, one obtains

$$e_2 = \frac{K u_* R}{\lambda} \left(\frac{x_2}{R}\right) \left(1 - \frac{x_2}{R}\right) \tag{2-20}$$

and

$$\bar{\bar{e}}_2 = 0.0236 \sqrt{f}\, \bar{\bar{u}}\, R/\lambda \tag{2-21}$$

Evans [1966] experimentally observed that the turbulent Schmidt number, λ, increased from 0.65 at a Reynolds number of 10,000 to approximately unity at Reynolds numbers of 50,000 and 100,000. Bonin et al.

[1957] also found that the turbulent Schmidt number was 0.65 at Reynolds number of 10,000. However, the highest value observed by them was 0.8 at Reynolds number about 56,000.

Evans [1966] used a parabolic diffusivity distribution across the pipe radius (Eq. 2-20) with $\lambda = 1$ to numerically calculate concentration distributions. When he compared these with some measurements, he found some discrepancies near the injector at the pipe center. He then concluded that a parabolic diffusivity is present in the outer half of the pipe radius but in the inner half, e_2 falls to some positive value rather than decreasing to zero at the pipe centerline, as would be predicted by Eq. 2-20. This conclusion is in good agreement with the variation of ε along the radius as given in Schlichting [1968] from Nikuradze's data for smooth pipes. Thus, in this study, Eq. 2-20 is modified as follows:

$$e_2 = \frac{Ku_*R}{\lambda} \left[\frac{x_2}{R} \left(1 - \frac{x_2}{R}\right) + \beta\left(\frac{x_2}{R}\right)\right] \tag{2-22}$$

with

$$\beta\left(\frac{x_2}{R}\right) = \begin{cases} 0.0 & \text{if } x_2/R > 0.5 \\ 0.075 \left(0.5 - \frac{x_2}{R}\right) & \text{if } x_2/R \le 0.5 \end{cases} \tag{2-23}$$

Equation 22 gives a nonzero value for e_2 at the centerline. Equation 2-23 was selected so that the magnitude of ε at the centerline ($0.15\ \varepsilon_{max}$) is in agreement with that obtained from Nikuradze's data. The average value $\bar{\bar{e}}_2$ from Eq. 2-22 is

$$\bar{\bar{e}}_2 = 0.0251\,\bar{\bar{u}}\,\sqrt{f}R/\lambda \qquad (2\text{-}24)$$

2.3.2 Turbulent Mass Diffusivity in Circumferential Direction

Because of the lack of knowledge on the turbulent momentum diffusivity in the circumferential direction in pipes, the analogy between the turbulent transfer of mass and momentum cannot be directly used to relate the turbulent mass diffusivity in the circumferential direction to flow characteristics. It will be assumed that turbulent mass diffusivities in the radial and circumferential directions have similar spatial variations. Thus, introducing a constant of proportionality (η), these two diffusivities will be related as

$$e_3 = \eta e_2 \qquad (2\text{-}25)$$

where e_2 and e_3 are the radial and circumferential diffusivities, respectively. The proportionality constant η was evaluated experimentally as discussed in Section 5.3.2.

3. THEORETICAL ANALYSIS

3.1 Objectives

The goal of this chapter is to present a mathematical treatment of the general, steady flow field and associated tracer concentration distributions resulting from a round, turbulent jet injected into a crossing pipe flow. The jet may be either buoyant or nonbuoyant. The tracer is conservative. The applicable equations are conservation of volume flux, conservation of momentum flux, and conservation of mass. The nonlinear nature of the resulting partial differential equations, the lack of knowledge about the pressure field and the turbulent stresses, and the boundary conditions imposed by the presence of the pipe wall make it impossible to obtain a complete solution either analytically or numerically. To overcome these difficulties, the three regions of the flow field cited previously are treated separately as presented below.

3.2 Mathematical Model

3.2.1 General Assumptions

The general assumptions underlying the analysis made in the present investigation are listed as follows:

1. The flow field is steady.
2. The fluids are incompressible.
3. The turbulent Schmidt number is unity.
4. The diffusion along the axis of the jet trajectory and

along the pipe axis is much smaller than the axial convection and can therefore be neglected.

Other assumptions are presented below where they enter into the presentation.

3.2.2 Mass and Density Disparity Conservation

Mixing of the jet with the pipe flow can be considered as a binary mixing process. Thus, for the jet component of the mixture, the following continuity equation may be written [Bird et al., 1960]

$$\nabla_i (u_i \rho_J) = e_i \nabla_i^2 \rho_J \qquad (3\text{-}1)$$

where ∇_i is the i-th component of ∇ operator, u_i is the i-th component of mass averaged velocity vector, ρ_J is the mass of jet component per unit volume of the mixture, and e_i is the diffusivity along the i-th direction and is assumed to be constant. The density ρ of the mixture is

$$\rho = \rho_J + \rho_A \qquad (3\text{-}2)$$

with

$$\rho_J = x\rho_j \qquad (3\text{-}3)$$

$$\rho_A = (1-x)\rho_a \qquad (3\text{-}4)$$

where ρ_A is the mass of ambient component per unit volume of the mixture, ρ_J is the mass of jet component per unit volume of the mixture, ρ_a is the ambient density, and x is the by weight fraction of the jet fluid in the mixture. Thus, combining Eqs. 3-2, 3-3, and 3-4, it may be shown that

$$x = \frac{\Delta\rho}{\Delta\rho_o} \tag{3-5}$$

with

$$\Delta\rho = \rho_a - \rho \tag{3-6}$$

$$\Delta\rho_o = \rho_a - \rho_j \tag{3-7}$$

where $\Delta\rho$ is the local density disparity associated with the jet and $\Delta\rho_o$ is the initial density disparity. Substituting Eqs. 3-3 and 3-5 into Eq. 3-1, one obtains

$$\nabla_i(u_i\Delta\rho) = e_i\nabla_i^2\Delta\rho \tag{3-8}$$

Equation 3-8 is equivalent to Eq. 3-1 and expresses the conservation of density disparity ($\Delta\rho$). In other words, conservation of density disparity is equivalent to conservation of mass.

Consider a control volume ¥ which is a curved, circular cylinder whose ends are perpendicular to the jet axis and whose lateral boundary is concentric with the jet axis. Take the volume integral of Eq. 3-8 over this control volume ¥. After using the Gaussian Theorem, the result may be written as

$$\int_S \Delta\rho u_j n_j dS = \int_{¥} e_i\nabla_i^2\Delta\rho d¥ \tag{3-9}$$

where S is the total surface area of the control volume ¥ and n_j is the unit normal vector along the j-th direction. There is experimental evidence [Fan, 1967; Keffer, 1969] that the effect of curvature of the jet trajectory may be neglected. Therefore, the following conversion formulae may be used:

$$\int_{V} (\ \ )dV = \int_{x_1}^{x_1+\Delta x_1} \int_{A} (\ \ )_1 \, dAdx_1 \tag{3-10}$$

$$\int_{S} (\ \ )dS = \int_{x_1}^{x_1+\Delta x_1} \int_{\sigma} (\ \ )d\sigma dx_1 + \int_{A} (\ \ )n_1 dA$$

$$= \int_{x_1}^{x_1+\Delta x_1} \int_{\sigma} (\ \ )d\sigma dx_1 + \int_{A} (\ \ )_1 dA]_{x_1}^{x_1+\Delta x_1} \tag{3-11}$$

where A is the cross-sectional area of V at any x_1 and σ is the periphery of V at any axial position. The radius of V is taken large enough so that $\Delta\rho \simeq 0$. Thus, using the above conversion formulae, Eq. 3-9 can be rewritten,

$$\int_{x_1}^{x_1+\Delta x_1} \int_{\sigma} \Delta\rho u_j n_j d\sigma dx_1 + \int_{A} \Delta\rho u_1 dA]_{x_1}^{x_1+\Delta x_1} = 0 \tag{3-12}$$

where the term involving e_1 has been dropped in accordance with the previous assumption. Dividing Eq. 3-12 by Δx_1 and taking the limit as Δx_1 approaches to zero, one obtains

$$\int_{\sigma} \Delta\rho u_j n_j d\sigma + \frac{d}{dx_1} \int_{A} \Delta\rho u_1 dA = 0 \qquad (3\text{-}13)$$

Since $\Delta\rho$ is assumed to diminish to zero on σ, Eq. 3-13 reduces to

$$\frac{d}{dx_1} \int_{A} \Delta\rho u_1 dA = 0 \qquad (3\text{-}14)$$

Integration of Eq. 3-14 gives

$$\int_{A} \Delta\rho u_1 dA = \text{constant} \qquad (3\text{-}15)$$

Eq. 3-15 is the integral form of conservation of density disparity flux.

3.2.3 Flow Establishment Region

A definition sketch for this region is shown in Fig. 2. The point 0 defines the end of the flow establishment region whereas $0'$ is the injection point.

Application of conservation of density disparity (Eq. 3-15) between sections $0'$ and 0 (Fig. 2) gives

$$\frac{\pi d^2}{4} u_o \Delta\rho_o = \int_{A|_{x_1 = x_e}} u_1 \Delta\rho dA \qquad (3\text{-}16)$$

where u_o is the initial velocity of the jet and is assumed to be uniformly distributed, $\Delta\rho_o$ is the initial density disparity and is also assumed to be uniformly distributed, d is the diameter of the injection hole, x_e is the length of the flow establishment region along the trajectory.

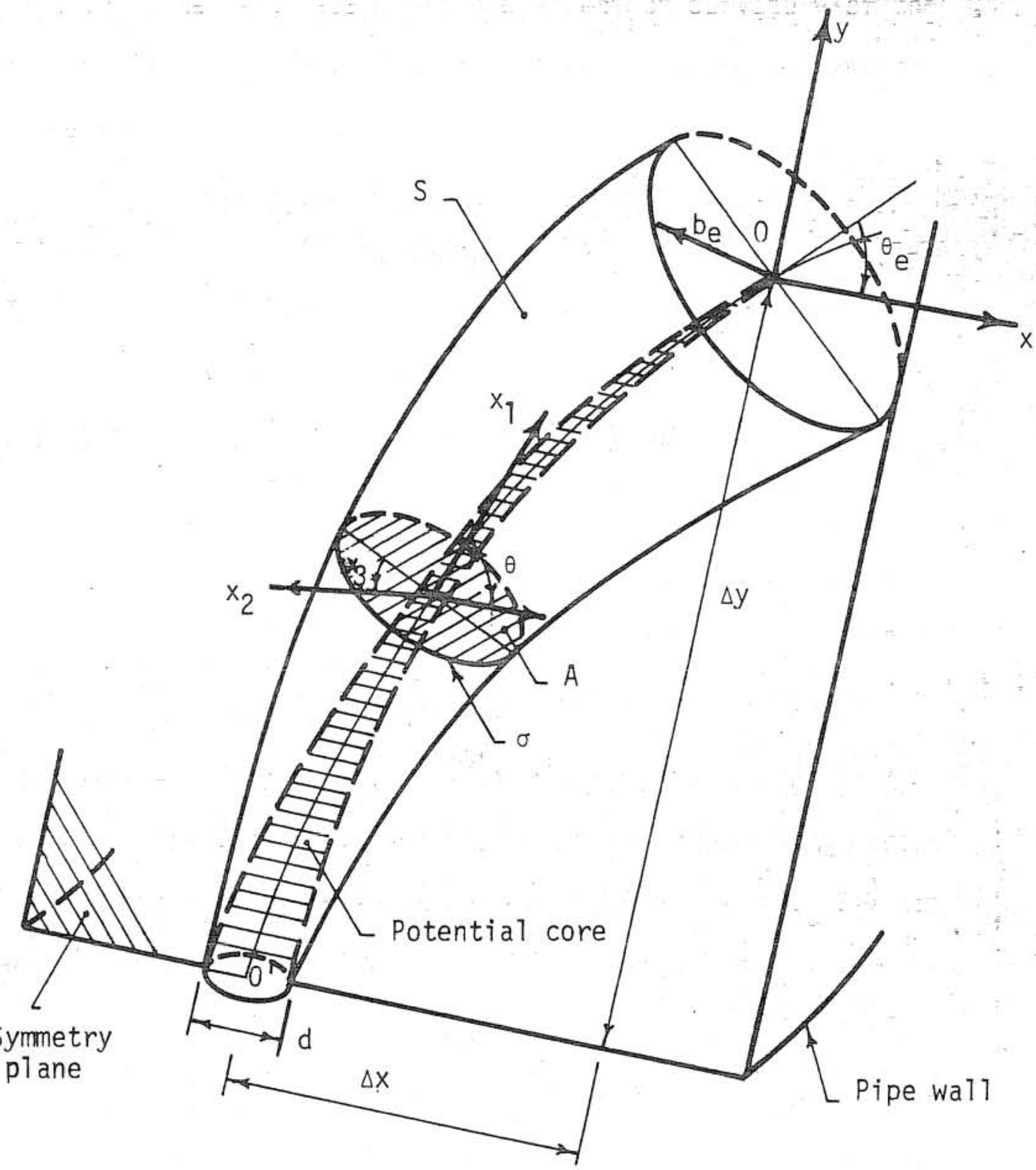

FIGURE 2: Definition sketch for flow establishment region

At the downstream end of the flow establishment region the profiles of velocity excess and density disparity are each assumed to be self-similar. Since there are indications that the Gaussian function closely approximates the velocity excess and density disparity profiles [Abraham, 1969; Fan, 1967; Hirst, 1972; Keffer, 1969; Motz and Benedict, 1970; Naudascher, 1967], the following relations are used (assuming a turbulent Schmidt number of unity):

$$u_1 - u_a \cos\theta = u_s \exp\left(-\frac{x_2^2}{b^2}\right) \tag{3-17}$$

$$\Delta\rho = \Delta\rho_s \exp\left(-\frac{x_2^2}{b^2}\right) \tag{3-18}$$

where u_1 is the jet velocity at any radial distance x_2 from the jet centerline, θ is the angle of deflection measured relative to the pipe axis, $u_1 - u_a \cos\theta$ is the velocity excess, u_s is the centerline velocity excess, $\Delta\rho$ is the density disparity (i.e., the absolute value of the density at any point in the jet minus the ambient density), $\Delta\rho_s$ is the centerline density disparity, and b is the nominal radius of the jet. The nominal radius of the jet, b, is defined as being equal to $\sqrt{2}\,\sigma$ where σ is the standard deviation of the velocity excess distribution. Thus, neglecting the variation in the ambient velocity u_a with x_2 at a given value of x_1, and using the fact that $u_s = u_o$ and $\Delta\rho_s = \Delta\rho_o$ at $x_1 = x_e$ (i.e., at the end of the undisturbed core of the jet), Eq. 3-16 becomes

$$\frac{\pi d^2}{4} u_o \Delta\rho_o = \int_{A|_{x_1=x_e}} [u_a|_{x_1=x_e} \cos\theta_e + u_o \exp(-\frac{x_2^2}{b_e^2})]$$

$$\cdot \Delta\rho_o \exp(-\frac{x_2^2}{b_e^2})\, dA \qquad (3\text{-}19)$$

Substituting $dA = x_2 dx_2 dx_3$, carrying out the integration in Eq. 3-19 and letting $b = b_e$ at $x_1 = x_e$, b_e is found to be

$$b_e = d\sqrt{k/2(k + \frac{u_a|_{x_1=x_e}}{\bar{\bar{u}}} \cos\theta_e)} \qquad (3\text{-}20)$$

where k is the ratio of the initial jet velocity u_o to average pipe velocity $\bar{\bar{u}}$, and θ_e is the angle of deflection at the end of the near field region.

Using the experimentally established fact that the density disparity does not play an important role in the dynamics of the flow in the region of flow establishment for buoyant jets [Stoy and Ben-Haim, 1973; Nece and Littler, 1973], the data of Fan [1967], and Motz and Benedict [1970] for nonbuoyant jets in crossflows can be used to evaluate θ_e, giving

$$\theta_e = \theta_o (0.9 - 0.7/k) \qquad (3\text{-}21)$$

where θ_o is the initial angle of deflection, which is $\pi/2$ for the present studies. The negligible influence of buoyancy also means that these relationships for the flow establishment region are valid for any inclination of the pipe axis with respect to the horizontal.

The distances x_e observed for jets in crossflows are smaller than the corresponding distances observed for jets in stagnant ambient fluids due to the increased entrainment of the ambient fluid when a crossflow exists [Fan, 1967; Keffer, 1969; Nece and Littler, 1973]. A study of the data from the same sources [Fan, 1967; Keffer, 1969; Nece, 1973] has further shown that $\Delta y \approx 3d$ and $\Delta x < 5d$, where Δy and Δx are the projections of x_e as shown in Fig. 2. A distance of $\Delta x = 5d$ is negligibly small compared with the total mixing distance and thus Δx will be taken as zero; Δy is taken as 3d. Since the dimensions of the jet near the injection location is small compared to the pipe radius, the above values obtained for injections from the flat surfaces are taken as fixed values. Thus, the calculations for the near field region are begun at $\Delta y = 3d$ and $\Delta x = 0$ with b_e and θ_e given by Eqs. 3-20 and 3-21 respectively and the velocity and density disparity distributions given by Eqs. 3-17 and 3-18.

3.2.4 Near Field Region

A definition sketch for the near field region is shown in Fig. 3. The equations used in this region are conservation of volume flux (Eq. 3-22), conservation of density disparity flux (Eq. 3-15), and conservation of momentum flux (Eq. 3-28). To overcome the difficulties met in solving these equations simultaneously, integral type equations are derived, resulting in a set of ordinary differential equations which can be integrated numerically. This latter set of equations has been shown [Fan, 1967; Keffer, 1969] to be a good approximation to the original set

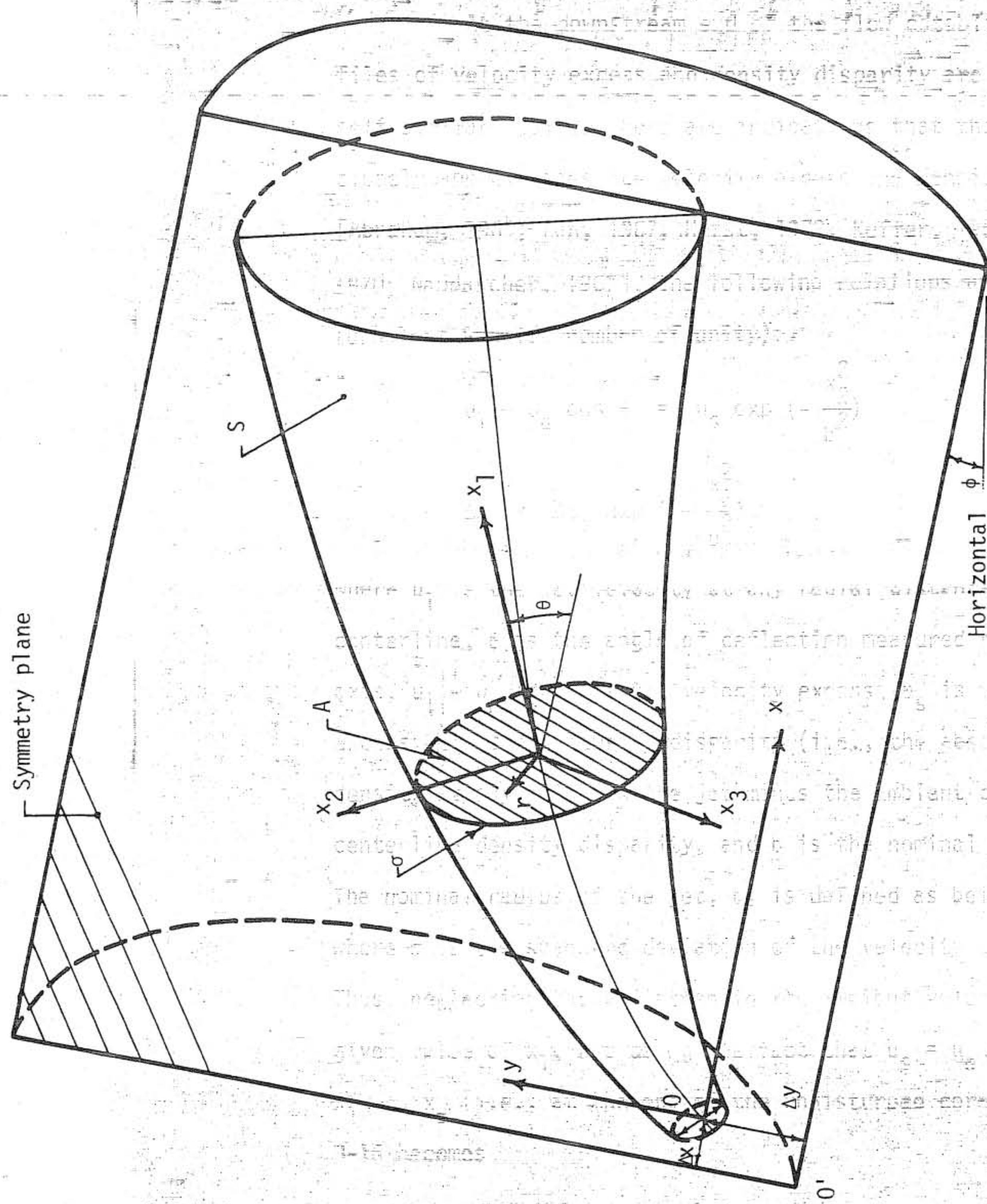

FIGURE 3: Definition sketch for the near field region

of point equations (Eqs. 3-15, 3-22, and 3-31). In the near field region, the coordinate axes (x_1, x_2, x_3, Fig. 3) are defined differently from those in the flow establishment region considered in the previous section. For the near field region x_1, x_2 and x_3 are a rectangular set of coordinates. The analytical considerations presented below assume that the effect of curvature of the jet trajectory is negligible on the dynamics of the flow.

The general conservation of volume flux may be written as

$$\nabla_i u_i = 0 \tag{3-22}$$

Consider the control volume defined in the preceding section. Integrating over the control volume and applying Gaussian transformation yield

$$\int_S u_j n_j \, dS = 0 \tag{3-23}$$

Using relation 3-11, one obtains

$$\int_{x_1}^{x_1+\Delta x_1} \int_\sigma (u_j n_j) \, d\sigma dx_1 + \int_A u_1 dA \Big]_{x_1}^{x_1+\Delta x_1} = 0 \tag{3-24}$$

Dividing by Δx_1 and taking the limit as Δx_1 approaches to zero, Eq. 3-24 becomes

$$\int_\sigma u_j n_j \, d\sigma + \frac{d}{dx_1} \int_A u_1 dA = 0 \tag{3-25}$$

In Eqs. 3-23, 3-24, and 3-25, the previous definitions for S, A, and σ still apply. After rearranging Eq. 3-25 and defining $u_e = -u_j n_j$, the result is

$$\frac{d}{dx_1} \int_A u_1 dA = \int_\sigma u_e d\sigma = E \tag{3-26}$$

where u_e is the component of velocity vector normal to the periphery σ of the cross-sectional area A, u_1 is the component of the velocity vector along the jet trajectory, and E is the entrainment. The periphery σ is assumed to be circular in shape, and the radius of the circle for the integration over σ is arbitrarily chosen to be $\sqrt{2}$ b, as is the normal practice [Fan, 1967; Hirst, 1972; Motz and Benedict, 1970].

Equation 3-26 is the one dimensional form of conservation of volume flux; the rate of change of volume flux within the jet along the trajectory is equal to the lateral inflow or entrainment, E.

The integral form of conservation of density disparity flux derived previously (Eq. 3-15) is also applicable in the near field region; in the derivation no restrictions were made to limit the applicability of the equation in the near field region. Thus, from Eq. 3-15,

$$\int_A \Delta\rho u_1 dA = \text{constant} \tag{3-27}$$

where

$$u_1 = u_a \cos\theta + u_s \exp\left(-\frac{r^2}{b^2}\right) \tag{3-28}$$

$$\Delta\rho = \Delta\rho_s \exp\left(-\frac{r^2}{b^2}\right) \tag{3-29}$$

$$r^2 = x_2^2 + x_3^2 \tag{3-30}$$

Equation 3-27 merely expresses the fact that the density disparity flux within the jet is invariant or that the mass flux must be conserved.

The steady state momentum equation may be written as [Hinze, 1959]

$$\rho u_j \frac{\partial u_i}{\partial x_j} = \rho f_i - \frac{\partial p}{\partial x_i} + \frac{\partial}{\partial x_j}[-\rho \overline{u_i' u_j'}] \tag{3-31}$$

where f_i is the component of body force along x_i, p is the pressure, u_i' is the turbulent fluctuation of x_i-velocity component and $\rho \overline{u_i' u_j'}$ are the Reynolds stresses. In Eq. 3-31, the viscous stresses are not considered since their magnitude is much smaller than their turbulent counterparts.

Integrating over the control volume, and applying the Gaussian transformation to Eq. 3-31, the x_1- and x_2- momentum equations in integral form are obtained:

x_1-component

$$\int_S \rho u_1 u_j n_j dS = \int_V \rho f_1 dV - \int_S p n_1 dS + \int_S (-\rho \overline{u_1' u_j'}) n_j dS \tag{3-32}$$

x_2-component

$$\int_S \rho u_2 u_j n_j dS = \int_{\forall} \rho f_2 d\forall - \int_S p n_2 dS + \int_S (-\rho \overline{u_2' u_j'}) n_j dS \quad (3\text{-}33)$$

The x_3-momentum equation in integral form vanishes because of the assumed symmetry condition which implies that the net momentum flux vector is in the plane of symmetry (Fig. 3).

It is convenient to consider the conservation of momentum along the x- and y-directions where x is parallel to the pipe axis, and y is orthogonal to x and is in the plane of the centerline trajectory of the jet (Fig. 3). The two coordinate systems, namely, (x_1, x_2, x_3) system and the (x,y) system, are related to each other by the deflection angle θ so that

$$\frac{dx}{dx_1} = \cos\theta \quad (3\text{-}34)$$

$$\frac{dy}{dx_1} = \sin\theta \quad (3\text{-}35)$$

The x- and y-momentum equations in integral form can then be written from Eqs. 3-32 and 3-33 as

x-component

$$\left(\int_S \rho u_1 u_j n_j dS\right)\cos\theta - \left(\int_S \rho u_2 u_j n_j dS\right)\sin\theta = \int_{\forall} f_x d\forall$$
$$- \left(\int_S p n_1 dS\right)\cos\theta + \left(\int_S p n_2 dS\right)\sin\theta$$
$$+ \left(\int_S -\rho \overline{u_1' u_j'} n_j dS\right)\cos\theta - \left(\int_S -\rho \overline{u_2' u_j'} n_j dS\right)\sin\theta \quad (3\text{-}36)$$

y-component

$$(\int_S \rho u_1 u_j n_j dS) \sin\theta + (\int_S \rho u_2 u_j n_j dS) \cos\theta = \int_{\forall} f_y d\forall$$

$$- (\int_S p n_1 dS) \sin\theta - (\int_S p n_2 dS) \cos\theta$$

$$+ (\int_S \overline{-\rho u_1' u_j'} n_j dS) \sin\theta + (\int_S \overline{-\rho u_2' u_j'} n_j dS) \cos\theta \qquad (3\text{-}37)$$

where f_x and f_y are components of body force in x and y directions, respectively. Using Eqs. 3-10 and 3-11, and then dividing by Δx_1 and taking the limit as Δx_1 appraoches to zero, the integral form of the x-momentum equation reduces to:

$$\frac{d}{dx_1} \int_A \rho(u_1^2 + \overline{u_1'^2}) \cos\theta \, dA = \int_\sigma -\rho(u_1 \cos\theta - u_x \sin\theta) u_j n_j d\sigma$$

$$+ \int_A f_x dA - \frac{d}{dx_1} \int_A p \cos\theta \, dA - \int_\sigma p \cos\theta \, d\sigma$$

$$+ \int_\sigma [\overline{-\rho u_1' u_j'} n_j \cos\theta - (\overline{-\rho u_2' u_j'}) n_j \sin\theta] d\sigma \qquad (3\text{-}38)$$

where u_1 is given by Eq. 3-17, and

$$u_2 = -u_a \sin\theta \qquad (3\text{-}39)$$

$$f_x = \Delta\rho \, g \sin\phi \qquad (3\text{-}40)$$

The angle ϕ is the angle between pipe axis and the horizontal defined as shown in Fig. 3. Substituting Eqs. 3-28 and 3-39 into the first term on the right hand side of Eq. 3-38, and dropping $\overline{u_1'^2}$ from the right hand side since $\overline{u_1'^2}$ is much smaller than u_1^2 [Naudascher, 1967; Robertson, 1965], Eq. 3-38 reduces to

$$\frac{d}{dx_1}\int_A \rho u_1^2 \cos\theta \, dA = \int_\sigma -\rho u_a u_j n_j d\sigma + \int_A f_x dA + F_x \tag{3-41}$$

where

$$F_x = -\frac{d}{dx_1}\int_A p \cos\theta \, dA - \int_\sigma p \cos\theta \, d\sigma + \int_\sigma [-\rho \overline{u_1' u_j'} n_j \cos\theta + \rho \overline{u_2' u_j'} n_j \sin\theta] d\sigma \tag{3-42}$$

F_x contains the terms which cannot be evaluated independently because of insufficient information. F_x represents the x component of the total drag force exerted by the ambient flow on the jet. Equation 3-41 is further simplified by assuming the value of u_a on the periphery σ can be replaced by the ambient velocity which would have existed on the center-line trajectory if the jet had not been there:

$$\frac{d}{dx_1}\int_A \rho u_1^2 \cos\theta \, dA = \rho u_a E + \int_A f_x dA + F_x \tag{3-43}$$

In a similar fashion, the integral form of y-momentum equation becomes

$$\frac{d}{dx_1}\int_A \rho u_1^2 \sin\theta \, dA = \int_A f_y dA + F_y \tag{3-44}$$

where

$$f_y = \Delta\rho \ g \cos \phi \tag{3-45}$$

$$F_y = -\frac{d}{dx_1}\int_A p \sin \theta \ dA - \int_\sigma p \sin \theta \ d\sigma$$
$$+ \int_\sigma (-\rho\overline{u_1 u_j} n_j \sin \theta - \rho\overline{u_1 u_j} n_j \cos \theta) d\sigma \tag{3-46}$$

F_y represents the y component of the total drag force exerted on the jet.

The simplified equations of conservation (Eq. 3-26, 3-27, 3-43, and 3-44) together with corrdinate transformation relations (Eqs. 3-34 and 3-35) constitute the system of equations to be solved simultaneously to define the flow field. These equations are essentially the same ones which were used by several investigators [Fan, 1967; Chan and Kennedy, 1972] previously. However, in the present work, the effect of the pipe velocity distribution on u_a is included in the analysis.

The number of unknowns in the above set of equations is greater than the number of equations by two. This lack of closure necessitates the use of some kind of phenomenological relationships for the entrainment and drag terms, E and F respectively. With reference to the definitions of E and F which were introduced in the preceding Chapter (Eqs. 2-5 and 2-7), the following relationships were defined:

$$E = 2\pi b\alpha(u_a^2 \sin^2 \theta + u_s^2)^{1/2} \tag{3-47}$$

$$F_x = \sqrt{2}\, C_D\, b\rho_a u_a^2 \sin^3 \theta \tag{3-48}$$

$$F_y = \sqrt{2}\, C_D\, b\rho_a u_a^2 \sin^2 \theta \cos \theta \tag{3-49}$$

where α is the entrainment coefficient and C_D is the drag coefficient. Both coefficients were experimentally evaluated as presented in Chapter 5.

The flux of any specific tracer contained in the jet should also be conserved; since Eq. 3-14 is valid for any scalar property being transported [Bird et al., 1960; Hinze, 1959], the conservation of concentration flux equation for a conservative tracer becomes

$$\frac{d}{dx_1} \int_A c u_1 \, dA = 0 \tag{3-50}$$

where c is the concentration (mass/volume) of the tracer. If the tracer is also responsible for the density differences, then c and $\Delta\rho$ can be assumed to be linearly related for small $\Delta\rho/\rho_a$. Thus, the concentration distribution is also assumed to be Gaussian:

$$c = c_s \exp\left(-\frac{r^2}{b^2}\right) \tag{3-51}$$

where c_s is the centerline concentration and r is the radial distance from the trajectory.

The applicable equations in the near field region are then obtained by substituting Eqs. 3-28, 3-29, 3-40, 3-45, 3-47, 3-48, 3-49, and 3-51 into Eqs. 3-26, 3-27, 3-43, 3-44, and 3-50:

$$\frac{d}{dx_1} [b^2(2u_a \cos \theta + u_s)] = 2\alpha b(u_a^2 \sin^2 \theta + u_s^2)^{1/2} \tag{3-52}$$

$$\Delta\rho_s \; b^2(2u_a \cos\theta + u_s) = \text{constant} \tag{3-53}$$

$$\frac{d}{dx_1}\left[\frac{b^2}{2}(2u_a \cos\theta + u_s)^2 \cos\theta\right] = 2\alpha b u_a (u_a^2 \sin^2\theta + u_s^2)^{1/2}$$

$$+ b^2 g \frac{\Delta\rho_s}{\rho_a} \sin\phi + \frac{\sqrt{2}\, C_D}{\pi} b u_a^2 \sin^3\theta \tag{3-54}$$

$$\frac{d}{dx_1}\left[\frac{b^2}{2}(2u_a \cos\theta + u_s)^2 \sin\theta\right] = \frac{b^2}{g} \frac{\Delta\rho_s}{\rho_a} \cos\phi$$

$$- \frac{\sqrt{2}\, C_D}{\pi} b u_a^2 \sin^2\theta \cos\theta \tag{3-55}$$

$$c_s \; b^2(2u_a \cos\theta + u_s) = \text{constant} \tag{3-56}$$

$$\frac{dx}{dx_1} = \cos\theta \tag{3-57}$$

$$\frac{dy}{dx_1} = \sin\theta$$

In obtaining the above set of equations, any influence of the variations of density on the inertial terms has been neglected, but has been retained in the buoyancy terms. This is commonly called the Boussinesq approximation. Furthermore, the turbulent Schmidt number has been taken as unity.

Integration of Eqs. 3-52 to 3-58, using the conditions at the end of the flow establishment region as boundary conditions (Section 3.2.4.1) and using the pipe velocity distribution for u_a gives the variation of u_s, b, $\Delta\rho_s$, and c_s and gives the trajectory of the jet. Equation

3-53, with appropriate initial conditions (Section 3.2.4.1), may be used to eliminate $\Delta\rho_s$ in Eqs. 3-54 and 3-55. Thus, there are only five unknowns (u_s, b, θ, x, and y) remaining in the system of five simultaneous ordinary differential equations (Eqs. 3-52, 3-54, 3-55, 3-57, 3-58). However, α and C_D must be obtained empirically (Section 5.4.3). After solving this system, $\Delta\rho_s$ and c_s can be obtained from Eqs. 3-53 and 3-56 with the appropriate initial conditions (Section 3.2.4.1).

3.2.4.1 Initial and Boundary Conditions

The initial conditions given at the end of the flow establishment region are

$$\left.\begin{aligned} u_s &= u_o \\ b &= b_e \\ \Delta\rho_s &= \Delta\rho_o \\ \theta &= \theta_e \\ c_s &= c_o \\ x &= 0 \\ y &= 0 \end{aligned}\right\} \quad \text{at } x_1 = 0 \qquad (3\text{-}59)$$

Although the above mathematical model is essentially an initial value problem, the presence of the confining boundary (i.e., the pipe wall) provides two boundary conditions which also must be satisfied. These boundary conditions are the nonslip condition for the velocity on the boundary and the condition that the radial mass transport must be zero at the boundary. This second condition will be called the reflective nature of the boundary. As long as the jet centerline stays more than $3b/\sqrt{2}$ (3σ) away from the pipe wall, these boundary conditions are not violated since at a radial distance of $3b/\sqrt{2}$, the magnitude of both velocity excess and the concentration can be considered as diminished to zero.

The fact that the wall confines the flow field imposes another constraint, namely that the total discharge past successive cross sections along the pipe axis must be constant downstream of the jet. As the jet entrains the ambient fluid, the discharge in the jet increases. This increase in the jet discharge will be compensated by a reduction in the discharge outside the jet. For all the cases investigated experimentally in this work, the reduction in the discharge is always less than 0.5 percent of the undisturbed pipe flow rate. Therefore in formulating the mathematical model for the near field region, the reduction in the pipe discharge is neglected.

3.2.4.2 The Definition of the End of the Near Field Region

The end of the near field region is defined arbitrarily as the pipe cross section at which the centerline velocity excess is less than or equal to 1 percent of the average pipe velocity and the centerline density disparity, if any, is less than or equal to 1 percent of the original value at the injection point, provided that the jet centerline is more than $3b/\sqrt{2}$ distance away from the pipe wall. The condition on the location of the jet centerline will be met in many cases of practical interest. If it is not met for some given set of parameters, that particular case cannot be analyzed by the mathematical model presented in this work. (For jets with a density disparity, a local densimetric Froude number defined as $\mathbb{F}_d = u_a/\sqrt{\Delta\rho_s \; g \; b/\rho_a}$ could have been used to define the point at which any density effects have disappeared rather than using the 1 percent criterion stated above. However, since there is no data to indicate the appropriate critical value of such a Froude number, the 1 percent value on $\Delta\rho$ was used instead.)

3.2.4.3 Method of Integration

The set of applicable equations have no explicit solution; a numerical integration is required. The equations were first normalized by using initial or average values to give dimensionless parameters as follows:

$$\left.\begin{aligned} U_s &= u_s/\bar{\bar{u}} \\ U_a &= u_a/\bar{\bar{u}} \\ B &= b/b_e \\ s &= 2\alpha x_1/b_e \end{aligned}\right\} \qquad (3\text{-}60)$$

$$\left.\begin{aligned} X &= 2\alpha x/b_e \\ Y &= 2\alpha y/b_e \end{aligned}\right\}$$

The distribution of u_a is given in Eq. 3-76. The set of equations (Eqs. 3-52, 3-54, 3-55, 3-57, and 3-58) were then transformed into a more convenient form for numerical integration:

$$\frac{dM}{ds} = R_1 \tag{3-61}$$

$$\frac{dN}{ds} = R_2 \cos\theta + R_3 \sin\theta \tag{3-62}$$

$$\frac{d\theta}{ds} = (R_3 \cos\theta - R_2 \sin\theta)/N \tag{3-63}$$

$$\frac{dX}{ds} = \cos\theta \tag{3-64}$$

$$\frac{dY}{ds} = \sin\theta \tag{3-65}$$

where

$$M = B^2(2U_a \cos\theta + U_s) \tag{3-66}$$

$$N = B^2(2U_a \cos\theta + U_s)^2 \tag{3-67}$$

$$R_1 = B(U_a^2 \sin^2\theta + U_s^2)^{1/2} \tag{3-68}$$

$$R_2 = 2U_a R_1 + D \sin\phi + C_D U_a^2 B \sin^3\theta \tag{3-69}$$

$$R_3 = D \cos\phi - C_D' U_a^2 B \sin^2\theta \cos\theta \quad (3\text{-}70)$$

$$D = (g\, \Delta\rho_o\, b_e/(\alpha\rho_a\, \bar{\bar{u}}^2))(2U_a \cos\theta + U_s) \quad (3\text{-}71)$$

$$C_D' = \sqrt{2}\; C_D/(\alpha\pi) \quad (3\text{-}72)$$

The initial conditions at s = 0 are

$$\begin{aligned} M(0) &= 2U_a\big|_{s=0} \cos\theta_e + k \\ N(0) &= M^2(o) \\ \theta(0) &= \theta_e \\ x(0) &= 0 \\ y(0) &= 0 \end{aligned} \quad (3\text{-}73)$$

where k is the ratio of initial jet velocity to ambient velocity, i.e.,

$$k = u_o/\bar{\bar{u}} \quad (3\text{-}74)$$

Equations 3-61 to 3-65 were integrated numerically on an IBM 360/75 digital computer using a subroutine [Ger and Holley, 1974] which is similar in structure to the subroutine "RKGS" of IBM [1972] and which is based on the fourth order Runge-Kutta formulae with the modification due to Gills [IBM, 1972; Collatz, 1960; Milne, 1970]. The accuracy and the step size are automatically controlled. The integration stops at the terminal point of the near field region.

3.2.5 Far Field Region

In the far field region, the study of the behavior of the tracer is assumed to be the study of mixing of a passive tracer in a turbulent pipe flow. In this region, in addition to the assumptions cited in Section 3.2.1, it is assumed that there are no residual effects of the jet and tracer from the near field region other than the distribution of the tracer within the cross section at the beginning of the far field region. In fact, this assumption is the definition of the far field region. The following assumptions are implications of the definition of the far field region:

1. There is no appreciable density difference between the jet fluid and that flowing in the pipe.
2. The pipe velocity profile is fully established and undisturbed by the presence of the jet.
3. There is no change in the pressure distribution due to presence of jet upstream of the far field region.
4. Disturbances in the turbulence structure due to presence of the jet upstream of the far field region are dissipated.

The steady state mass transport is mathematically an equilibrium problem. In other words, with reference to Fig. 4 (note that coordinate axes are redefined), the equilibrium distribution of concentration c in a domain D, for a given initial distribution at the end of the near field region, is to be determined by solving the differential equation [Bird et al., 1960; Hinze, 1959]

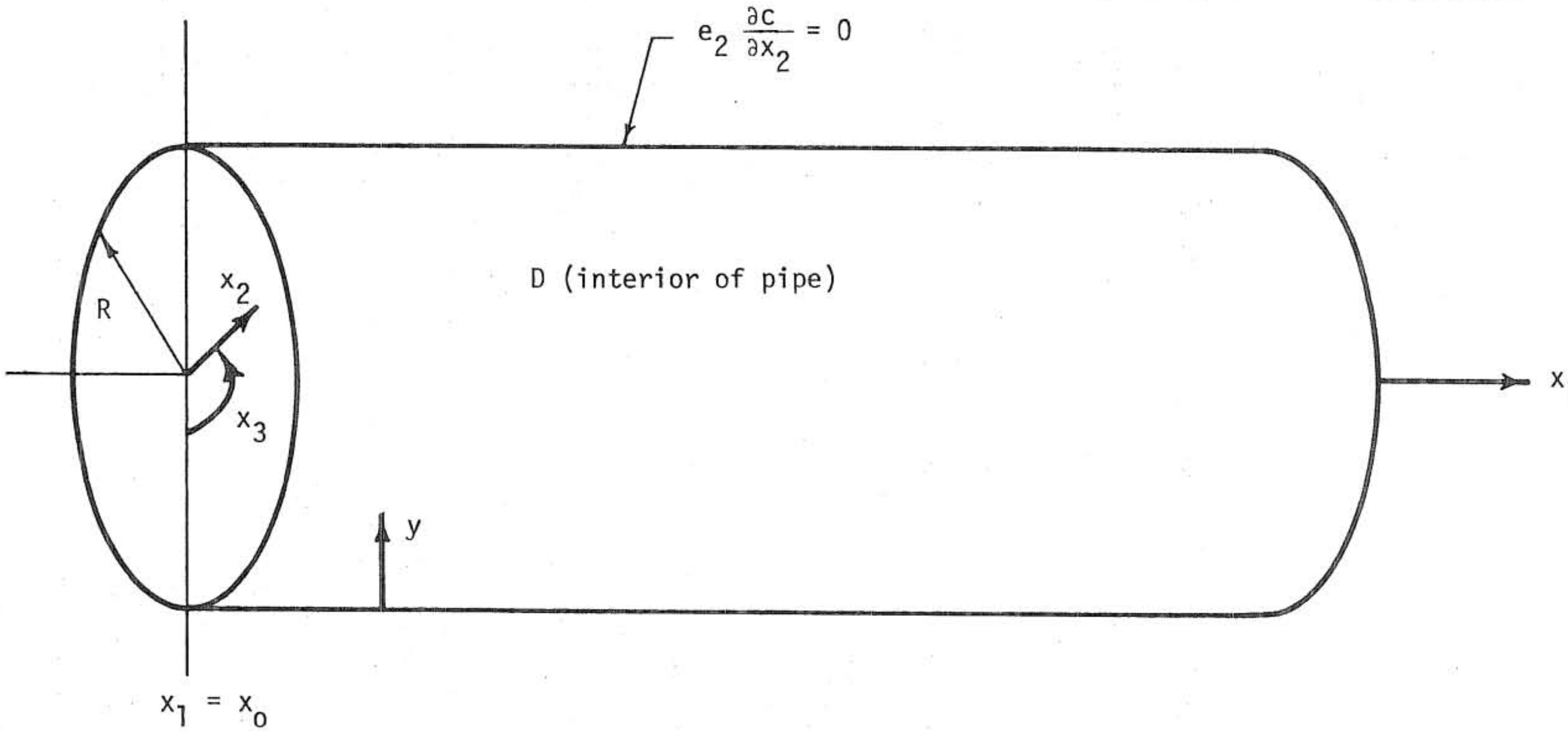

FIGURE 4: Definition sketch for the far field region

$$\frac{\partial}{\partial x_1}(uc) = \frac{1}{x_2}\frac{\partial}{\partial x_2}(x_2 e_2 \frac{\partial c}{\partial x_2}) + \frac{1}{x_2^2}\frac{\partial}{\partial x_3}(e_3 \frac{\partial c}{\partial x_3}) \tag{3-75}$$

within D, subject to certain conditions on the boundary. In Eq. 3-75, u is the axial velocity, and e_2 and e_3 are, respectively, the radial and circumferential turbulent mass diffusivities as discussed in Sections 2.3.1 and 2.3.2. In this study, the distribution of u is approximated by a power law (Section 4.2.2)

$$u = a\bar{\bar{u}} (1 - \frac{x_2}{R})^{1/n} \tag{3-76}$$

Since the initial condition (i.e., concentration distribution of tracer) at the $x_1 = 0$ plane is not necessarily axisymmetric, both the radial and the circumferential diffusion terms must be retained on the right-hand side of Eq. 3-75. However, for the range of Reynolds number ($> 4 \times 10^3$) of interest here, the contribution of axial diffusion has been neglected in Eq. 3-75 on the basis of past work [Section 2.3 and Roley, 1960; Seagrave, 1960; Evans, 1966].

The lateral boundary of D is the pipe wall where there is no mass transport in the x_2-direction. Because the mass transport is a gradient type process, this boundary condition can be expressed as

$$e_2 \frac{\partial c}{\partial x_2}\Big|_{x_2=R} = 0 \tag{3-77}$$

Using the above equation as the boundary condition, the problem of solving Eq. 3-75 reduces to an initial value problem such that the solution depends only on the concentration distribution at the beginning of the far field region and the flow characteristics u, e_2, e_3.

A general treatment of elliptic equations is available in Ames [1969], Varga [1970], among others [Crank, 1964; Carslaw and Jaeger, 1965; Kantorovich and Krylov, 1964]. Under certain conditions, analytical solutions for Eq. 3-75 are possible [Crank, 1964; Carslaw and Jaeger, 1965; Kantorovich and Krylov, 1964]. The next subsection presents one such solution which is useful for this study.

3.2.5.1 An Analytical Solution for a Wall Source

For a continuous point source at the pipe wall, Eq. 3-75 has an analytic closed form solution if ambient flow characteristics are such that

$$u = \bar{\bar{u}} = \text{constant} \qquad (3\text{-}78)$$

$$e_2 = e_3 = k_r = \text{constant} \qquad (3\text{-}79)$$

Substituting Eqs. 3-78 and 3-79 into Eq. 3-75, and rearranging, one obtains

$$\frac{\partial^2 c}{\partial x_2^2} + \frac{1}{x_2}\frac{\partial c}{\partial x_2} + \frac{1}{x_2^2}\frac{\partial^2 c}{\partial x_3^2} - \frac{\bar{\bar{u}}}{k_r}\frac{\partial c}{\partial x_1} = 0 \qquad (3\text{-}80)$$

This equation will be solved subject to the boundary conditions of a unit continuous point source located at $x_1 = 0$, $x_2 = R$, and $x_3 = 0$ and

$$\left.\frac{\partial c}{\partial x_2}\right|_{x_2 = R} = 0 \qquad (3\text{-}81)$$

Introducing the new variable t, the travel time,

$$t = \frac{x_1}{\bar{\bar{u}}} \tag{3-82}$$

Eq. 3-77 becomes

$$\frac{\partial^2 c}{\partial x_2^2} + \frac{1}{x_2}\frac{\partial c}{\partial x_2} + \frac{1}{x_2^2}\frac{\partial^2 c}{\partial x_3^2} - \frac{1}{k_r}\frac{\partial c}{\partial t} = 0 \tag{3-83}$$

This equation now mathematically represents an unsteady diffusion problem in two dimensions (x_2 and x_3). The boundary condition given in Eq. 3-81 is not affected by the change from axial distance x_1 to travel time t. However, the boundary condition of a continuous point source is transformed into an initial condition of an instantaneous, infinitely long, line source parallel to the pipe axis at $x_2 = R$, $x_3 = 0$ at $t = 0$. This line source at the wall must be infinitely long in order to maintain the two-dimensionality of the problem. Since Eqs. 3-80 and 3-81 are related to each other by Eq. 3-82, the solution of Eq. 3-80 can be obtained from the solution of Eq. 3-83 replacing t by $x_1/\bar{\bar{u}}$.

The infinitely long line source can be viewed as the superposition of point sources. For an instantaneous, unit point source at $x_1 = \xi$, $x_2 = R$, $x_3 = 0$ and $t = 0$, it has been shown [Carslaw and Jaeger, 1965] that the concentration distribution is given by

$$c = \frac{\exp\left[-\frac{(x_1-\xi)^2}{4K_r t}\right]}{2\pi\sqrt{\pi K_r t}}\left[1 + \sum_{n=-\infty}^{\infty} \cos n x_3 \sum_{m=1}^{\infty} \frac{\exp(-K_r \alpha_{n,m}^2 t)\,\alpha_{n,m}^2\, J_n(\alpha_{n,m} x_2)}{(\alpha_{n,m}^2 - n^2)\, J_n(\alpha_{n,m})}\right] \tag{3-84}$$

where

$$K_r = \frac{k_r}{R^2} \tag{3-85}$$

$$X_1 = \frac{x_1}{R} \tag{3-86}$$

$$X_2 = \frac{x_2}{R} \tag{3-87}$$

and $\alpha_{n,m}$ is the m-th positive root of $J_n'(\alpha) = 0$. Thus, the solution of Eq. 3-83, subject to the aforementioned initial and boundary conditions, is obtained by integrating Eq. 3-84 over ξ from $-\infty$ to $+\infty$:

$$c = \frac{1}{\pi}\left[1 + \sum_{n=-\infty}^{\infty} \cos n\, x_3 \sum_{m=1}^{\infty} \frac{\exp\,(-K_r\alpha_{n,m}^2 J_n(\alpha_{n,m}X_2)}{(\alpha_{n,m}^2 - n^2)\; J_n(\alpha_{n,m})}\right] \tag{3-88}$$

Substituting Eqs. 3-82, 3-85, and 3-86 into Eq. 3-88, the solution of Eq. 3-80 subject to appropriate boundary conditions is obtained:

$$c = \frac{1}{\pi}\left[1 + \sum_{n=-\infty}^{\infty} \cos n\, x_3 \sum_{m=1}^{\infty} \frac{\exp\,(-\frac{k_r\alpha_{n,m}^2 x_1}{R^2\;\bar{\bar{u}}})\;\alpha_{n,m}^2\; J_n(\alpha_{n,m}x_2/R)}{(\alpha_{n,m}^2 - n^2)\; J_n(\alpha_{n,m})}\right] \tag{3-89}$$

Since

$$J_{-n}(z) = (-1)^n J_n(z) \tag{3-90}$$

Eq. 3-89 is further simplified to

$$c = \frac{1}{\pi}\left[1 + \sum_{n=0}^{\infty} w_n \cos n\, x_3 \sum_{m=1}^{\infty} \exp\left(-\frac{k_r\, \alpha_{n,m}^2\, x_1}{R^2\, \bar{\bar{u}}}\right) \frac{\alpha_{n,m}^2\, J_n(\alpha_{n,m} x_2/R)}{(\alpha_{n,m}^2 - n^2)\, J_n(\alpha_{n,m})}\right] \quad (3\text{-}91)$$

where

$$w_n = \begin{cases} 1 & \text{if } n = 0 \\ 2 & \text{if } n > 0 \end{cases} \quad (3\text{-}92)$$

Equation 3-91 is an analytical solution of a simplified form of diffusion equation (Eq. 3-80) for a continuous point source at the pipe wall and was used for comparison with the results of numerical computations for selection of the optimum grid size for the finite difference scheme used in numerical integration of Eq. 3-75, as discussed below.

3.2.5.2 Method of Numerical Integration

In the case where u, e_2, and e_3 are arbitrary functions of x_2, an analytical solution could not be found. Therefore, numerical integration was used. In this study, an alternating direction implicit finite difference scheme was used for a number of reasons, the primary one being the unconditional stability of the scheme [Ames, 1969; Siemons, 1970]. Another feature of the method is a reformulation of the finite difference equations so that the algebraic system generated in the numerical procedure can be easily solved. Further, the method is convergent [Ames, 1969; Varga, 1962].

In an alternating direction implicit method, the distribution at $x_{1,k}$ is used to calculate the distribution at the next downstream

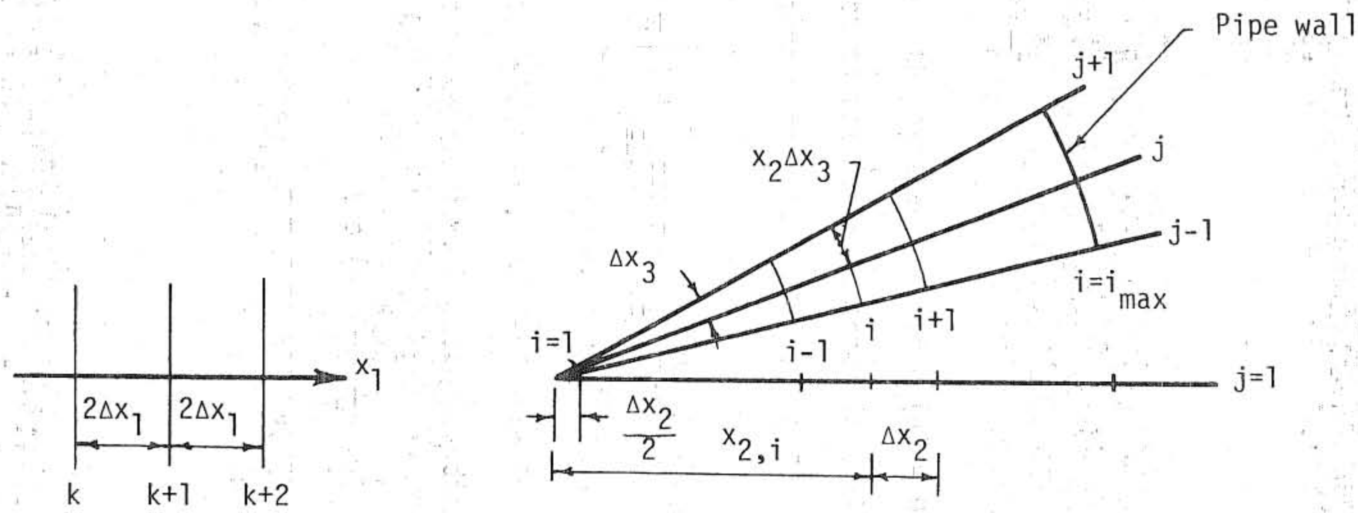

FIGURE 5: Definition of step sizes for far field region

cross section, $x_{1,k} + \Delta x_1$ (Fig. 5), considering radial diffusion only. Then starting from $x_{1,k} + \Delta x_1$, the distribution at $x_{1,k} + 2\Delta x_1$ is obtained, but this time only circumferential diffusion is considered. The method can be iterated, but iteration was not used in this study.

The following central difference relations were used in the derivation of finite difference equations:

$$\frac{\partial(\ )}{\partial x_i} = \frac{1}{2\Delta x}\left[(\ )_{i+1} - (\ )_{i-1}\right] \tag{3-93}$$

$$\frac{\partial}{\partial x}\left[z\frac{\partial}{\partial x}(\ )\right] = \frac{1}{(\Delta x)^2}\left[z_{i+1/2}(\ )_{i+1} + z_{i-1/2}(\ )_{i-1} - (z_{i+1/2} + z_{i-1/2})(\ )_i\right] \tag{3-94}$$

Considering only advection and radial diffusion in the first half of the alternating direction implicit scheme, a finite difference equation which is implicit in the radial direction is obtained:

$$\sum_{\ell=i-1}^{i+1} a_{k+1,\ell,j}\, c_{k+1,\ell,j} = p_{k+1,i,j} \tag{3-95}$$

where

$$a_{k+1,i-1,j} = \frac{\Delta x_1}{u_i}\left[-\frac{(e_2)_{i-1/2}}{(\Delta x_2)^2} + \frac{(e_2)_i}{2x_{2,i}\,\Delta x_2}\right] \tag{3-96}$$

$$a_{k+1,i,j} = 1 + \frac{\Delta x_1}{u_i(\Delta x_2)^2}\left[(e_2)_{i+1/2} + (e_2)_{i-1/2}\right] \tag{3-97}$$

$$a_{k+1,i+1,j} = \frac{\Delta x_1}{u_i}\left[-\frac{(e_2)_{i+1/2}}{(\Delta x_2)^2} - \frac{(e_2)_i}{2x_{2,i}\,\Delta x_2}\right] \qquad (3\text{-}98)$$

$$p_{k+1,i,j} = c_{k,i,j-1}\left[\frac{\Delta x_1 (e_3)_{j-1/2}}{u_i\, x_{2,i}^2 (\Delta x_3)^2}\right]$$

$$+ \; c_{k,i,j}\left[1 - \frac{(\Delta x_1)\,[(e_3)_{j+1/2} + (e_3)_{j-1/2}]}{u_i\, x_{2,i}^2 (\Delta x_3)^2}\right]$$

$$+ \; c_{k,i,j+1}\left[\frac{\Delta x_1 (e_3)_{j+1/2}}{u_i\, x_{2,i}^2 (\Delta x_3)^2}\right] \qquad (3\text{-}99)$$

Equations 3-96, 3-97, and 3-98 cannot be used in evaluating the coefficients $a_{k+1,i_{max}-1,j}$, $a_{k+1,i_{max},j}$, and $a_{k+1,i_{max}+1,j}$ corresponding to a boundary point (i.e., $i = i_{max}$), since i_{max} +1 fell outside the boundaries. Thus, the mirror image technique (Fig. 6) as described elsewhere [Harleman, 1960] is used to satisfy the boundary condition (Eq. 3-77). In this technique, the concentration at the fictitious point $i_{max} + 1$ is set equal to the concentration at $i_{max} - 1$ so that the boundary condition $\partial c/\partial x_2 = 0$ on the boundary (i.e., $i = i_{max}$) is satisfied. Hence,

$$a_{k+1,i_{max}-1,j} = -\frac{(\Delta x_1)(e_2)_{i_{max}-1/2}}{u_{i_{max}-1/4}(\Delta x_2)^2} \qquad (3\text{-}100)$$

$$a_{k+1,i_{max},j} = 1 + \frac{2(\Delta x_1)(e_2)_{i_{max}-1/2}}{u_{i_{max}-1/4}(\Delta x_2)^2} \qquad (3\text{-}101)$$

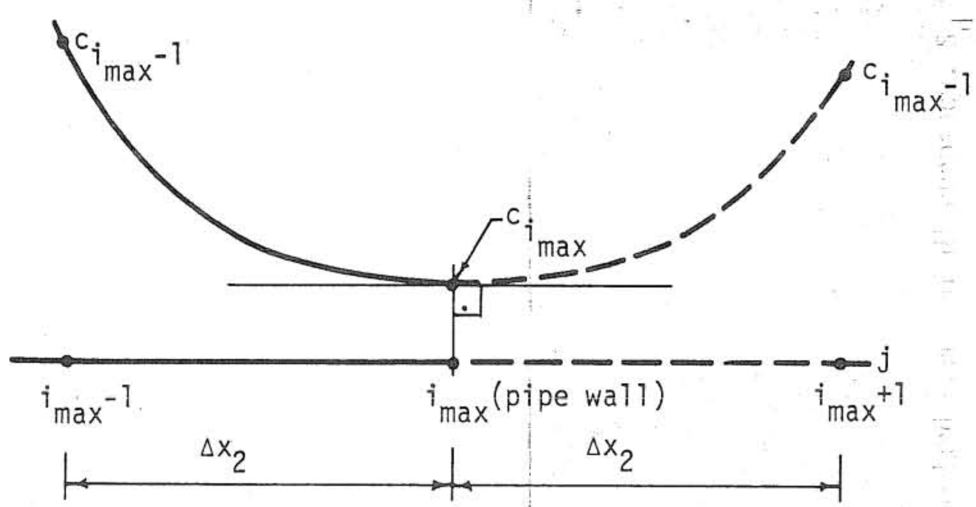

FIGURE 6: Schematic representation of mirror image technique

$$a_{k+1,i_{max}+1,j} = a_{k+1,i_{max}-1,j} \tag{3-102}$$

Equations 3-100, 3-101, and 3-102 now provide necessary and sufficient information for the evaluation of the a-coefficients corresponding to a point on the pipe wall.

For the second half of the alternating direction implicit method, a finite difference equation which is implicit in the circumferential direction is obtained, considering only advection and circumferential diffusion:

$$\sum_{m=j-1}^{j+1} f_{k+2,i,m}\, c_{k+2,i,m} = p_{k+2,i,j} \tag{3-103}$$

where

$$f_{k+2,i,j-1} = - \frac{(\Delta x_1)(e_3)_i}{u_i\, x_{2,i}^2 (\Delta x_3)^2} \tag{3-104}$$

$$f_{k+2,i,j} = 1 + \frac{2(\Delta x_1)(e_3)_i}{u_i\, x_{2,i}^2 (\Delta x_3)^2} \tag{3-105}$$

$$f_{k+2,i,j+1} = f_{k+2,i,j-1} \tag{3-106}$$

$$p_{k+2,i,j} = 2c_{k+1,i,j} - p_{k+1,i,j} \tag{3-107}$$

In Eq. 3-103, when $j = 1$, $j - 1$ is replaced by j_{max} and when $j = j_{max}$, $j + 1$ is replaced by 1 in order to close the circle in the x_3-direction.

Equations 3-95 and 3-103 can be rewritten in matrix notation as

$$A^{k+1}\ C^{k+1} = P^{k+1} \tag{3-108}$$

$$F^{k+2}\ C^{k+2} = P^{k+2} \tag{3-109}$$

Equations 3-108 and 3-109 are the finite difference equations which now represent the differential equation (Eq. 3-75) plus the boundary condition (Eq. 3-77). Knowing the distribution at $x_{1,k}$, the distribution at $x_{1,k+1}$ is computed using Eq. 3-108. The result of this computation becomes the initial distribution for Eq. 3-109. The solution of Eq. 3-109 is the distribution at $x_{1,k+2}$. The resulting distribution at $x_{1,k+2}$ is then used to begin the integration for the next segment of length $2\Delta x$. The integration proceeds in this manner in the x_1 direction.

Any one of the familiar methods of solving a system of linear algebraic equations may be applied to the solution of the finite difference equations (Eqs. 3-108 and 3-109). In this study, the method of successive elimination is used [Kantorovich and Krylov, 1964].

Numerical integration of Eqs. 3-108 and 3-109 was carried out on an IBM 360/75 digital computer [Ger and Holley, 1974]. The step size along the x_1-axis was controlled automatically by assuming that the longitudinal gradients would decrease as the gradients within a cross section decreased. The initial Δx_1 step size at the beginning of the far field region was selected as one pipe radius. As x increased, the Δx_1 step size was doubled when the range of c values within a given cross section became half of the range for which the current Δx_1 was established. The step sizes for x_2 and x_3 axis were selected as described below. Integrations were carried out until a predetermined degree of uniformity within a pipe cross section was obtained.

3.2.5.3 Selection of the Optimum Grid Configuration

The optimum grid configuration is the one for which a reasonable amount of computer time is used to numerically produce concentration distributions which are within an acceptable tolerance of the true solutions. The optimum grid configuration must be selected empirically. Experimentally recorded concentration distributions cannot be used for this procedure since the circumferential diffusivity is not known a priori. Therefore, the optimum grid configuration was selected so that the concentration distributions obtained by the numerical integration of Eq. 3-80 (simplified form of Eq. 3-75) were within an acceptable tolerance of the analytical solution given by Eq. 3-91. Closeness of numerical and analytical solutions were checked by

1. Comparison of the standard deviations, σ, of the concentration distributions within various cross section along the pipe axis,
2. The cumulative loss m_ℓ, in total mass flux in the numerical integration, and
3. The standard error of discrepancy, S_d, between the

numerically evaluated concentration distributions and corresponding analytical solutions.

The following definitions were used:

$$\sigma = \frac{1}{c}\sqrt{\sum_{i,j} a_{i,j}(c_{i,j} - \bar{c})^2/A} \qquad (3\text{-}110)$$

$$m_\ell = 1 - \left(\sum_{i,j} a_{i,j}\, c^{(n)}_{i,j}\right)/A\bar{c}^{(a)} \qquad (3\text{-}111)$$

$$S_d = \frac{1}{c}\sqrt{\sum_{i,j} a_{i,j}\,(c^{(n)}_{i,j} - c^{(a)}_{i,j})^2/A} \qquad (3\text{-}112)$$

$$L = x_1/2R \qquad (3\text{-}113)$$

where $\bar{c}$ is the cross-sectional average concentration, A is the cross-sectional area, i and j are the indices describing the location of the grid point, $c^{(n)}_{i,j}$ and $c^{(a)}_{i,j}$ are the concentrations obtained numerically (superscript n) and analytically (superscript a), and $a_{i,j}$ is area represented by the grid point. This area is defined by the perpendicular bisectors of the line segments between the grid point and the neighboring points.

For pipe Reynolds number of 100,000, four different grid sizes were tried:

Number of Grid Points	
x_2	x_3
10	32
10	16
5	32
5	16

There are no significant differences among the different grid sizes as far as the variation in standard deviation along the pipe axis is concerned (Table 1). However, as shown in Table 2 and Fig. 7, the cumulative loss in total mass flux for the numerical integration is highly dependent on the number of grid points along the radial direction; for the larger number of points, there is less total mass loss. Furthermore, when the variation in the standard error of discrepancy is studied (Table 3 and Fig. 8), the same conclusion relative to the number of radial grid points is reached. The optimum was selected as 10 and 32 grid points along the radial and circumferential directions (i.e., $\Delta x_2 = R/9.5$ and $\Delta x_3 = \pi/16$) and this arrangement was used in all further numerical computations. The length of required computer time is shown in Table 4.

3.3 Further Remarks

The proposed model to describe the general flow field of a round, turbulent jet in a crossing pipe flow differs from the past work on the jets in a crossflow in three primary ways:

Table 1

Variation in σ with L and Number of Grid Points

L	Eq. 3-91 Analytic S.	Numeric S. 5x16	5x32	10x16	10x32
24	1.167	1.173	1.157	1.184	1.168
44	0.711	0.709	0.702	0.718	0.711
64	0.465	0.462	0.458	0.469	0.464
84	0.308	0.307	0.304	0.311	0.307
104	0.205	0.205	0.203	0.208	0.204
124	0.137	0.138	0.136	0.139	0.136

Table 2

Variation in Cumulative Loss of Mass with L and Number of Grid Points

L	5x16	5x32	10x16	10x32
24	0.01230	0.01330	0.00300	0.00303
44	0.01370	0.01480	0.00325	0.00329
64	0.01390	0.01510	0.00331	0.00335
84	0.01400	0.01520	0.00338	0.00335
104	0.01400	0.01520	0.00338	0.00335
124	0.01400	0.01520	0.00338	0.00335
164	0.01400	0.01520	0.00338	0.00335

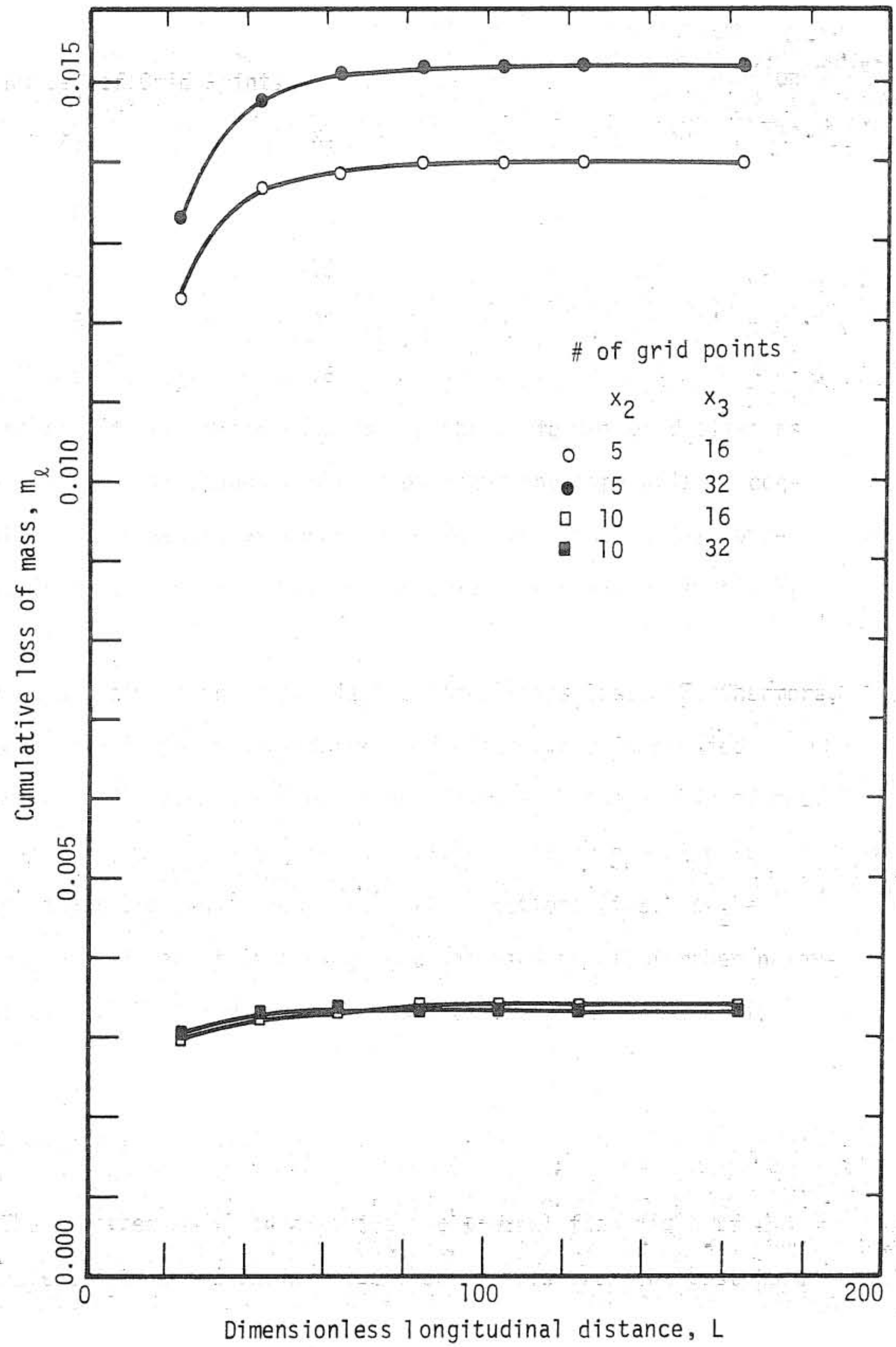

FIGURE 7: Variation of cumulative loss of mass with L and number of grid points

Table 3

Variation in S_d with L

L	5x16	5x32	10x16	10x32
24	0.0620	0.0299	0.0538	0.0129
44	0.0284	0.0240	0.0184	0.0064
64	0.0226	0.0230	0.0090	0.0053
84	0.0214	0.0226	0.0056	0.0052
104	0.0211	0.0224	0.0045	0.0052
124	0.0211	0.0223	0.0042	0.0051

Table 4

Approximate Time of Computation for Mixing Distance of 164 Pipe Diameter

No. of Grid Points	t
5 x 16	40 sec.
5 x 32	200 sec.
10 x 16	80 sec.
10 x 32	400 sec.

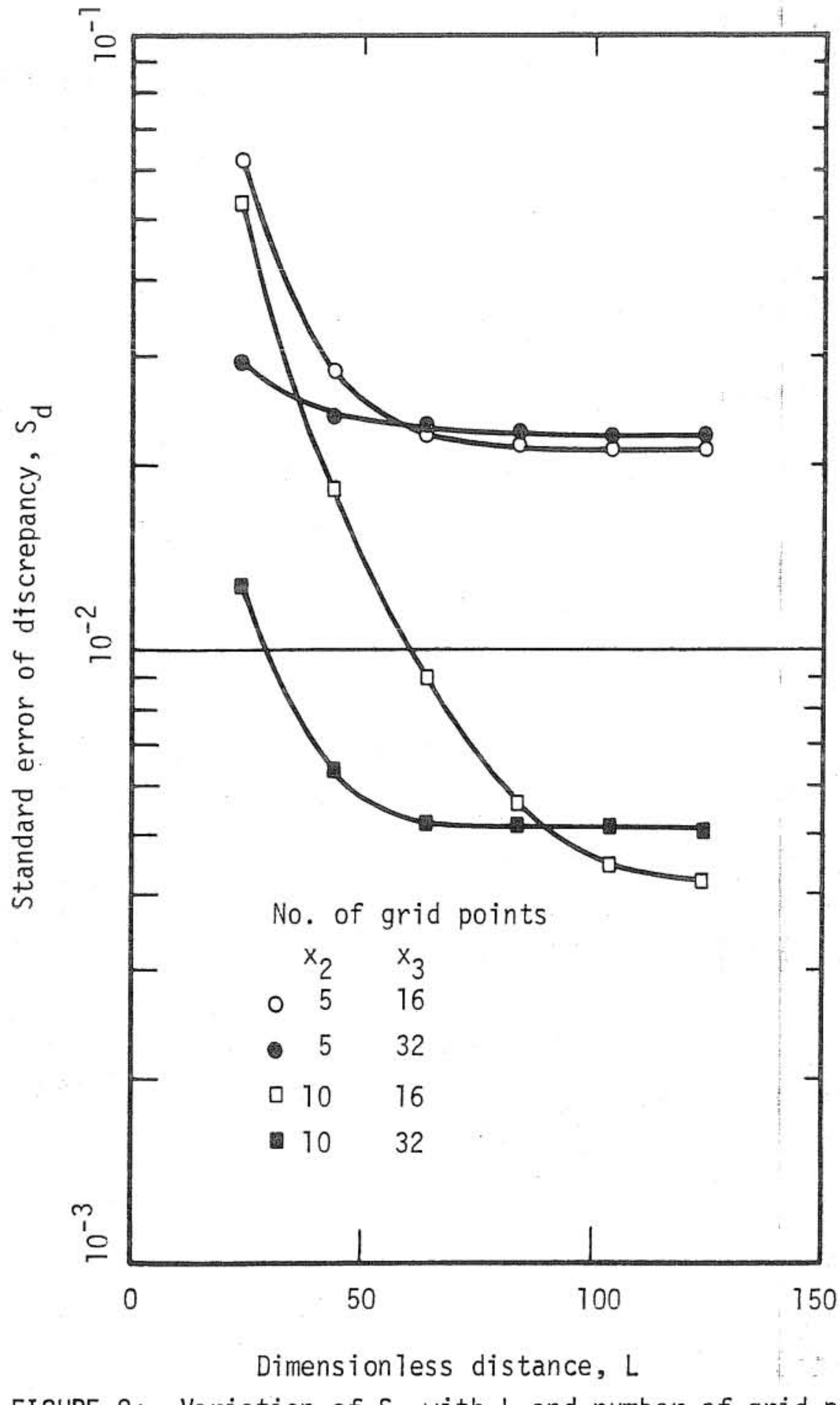

FIGURE 8: Variation of S_d with L and number of grid points

1. The applicable equations (Eqs. 3-52 through 3-58) for the near field region were derived from the basic governing point equations so that the meaning of each term is more clearly defined.
2. The nonuniform velocity distribution of the crossing pipe flow is considered by letting u_a in Eqs. 3-52 through 3-58 and 3-80 vary across the pipe according to a power law.
3. The turbulence of crossflow is taken into account by the consideration of a far field region. Also, the effects of the pipe turbulence in the near field region are inherently reflected by the experimentally evaluated entrainment and drag coefficients presented in Section 5.4.3.

There is no precise point at which the change between the near field and far field regions takes place. There exists a transitional regime between those two regions in which both the jet characteristics and the pipe flow turbulence have some influence on the mixing of the tracer with the ambient flow. Although there is no experimental verification, it is assumed in this study that the jet-induced turbulence loses its significance at the end of the near field region. Thus, no transition region is considered. The end of the near field region defines the beginning of the far field region. In other words, any jet-induced turbulence or disruption of the pipe-flow velocity distribution in the far field region is assumed to be negligible.

4. EXPERIMENTAL EQUIPMENT AND PROCEDURES

4.1 Objectives

The mixing distance is defined as the longitudinal distance between the injection point and the point at which the variation in concentration becomes less than some specified value. Therefore, the experimental determination of the mixing distance is based on an evaluation of the variation in concentration of tracer over each of a series of cross sections at downstream position from the injection point.

In this investigation, experiments were run primarily to evaluate the mixing distance associated with the use of a jet, with or without buoyancy, perpendicular to the pipe wall. Furthermore, the experimental results were used in evaluation of the entrainment coefficient, α, and the drag coefficient, C_D, for the jet and the circumferential diffusivity, e_3, for pipe flow.

4.2 Apparatus

4.2.1 The Hydraulic Circuit

The experimental system is shown schematically in Fig. 9. The pipe was 6 in. IPS galvanized steel. The inside diameter was $6 \pm 1/16$ in.

The laboratory sump water was used to supply the flow in the pipe. Valve A (Fig. 9) was used as a shut-off valve, while valve B (Fig. 9) was used in controlling the flow. The flow was measured by a Dall-Flowmeter (BIF, Model 0122-25) indicated in Fig. 9. Weighing

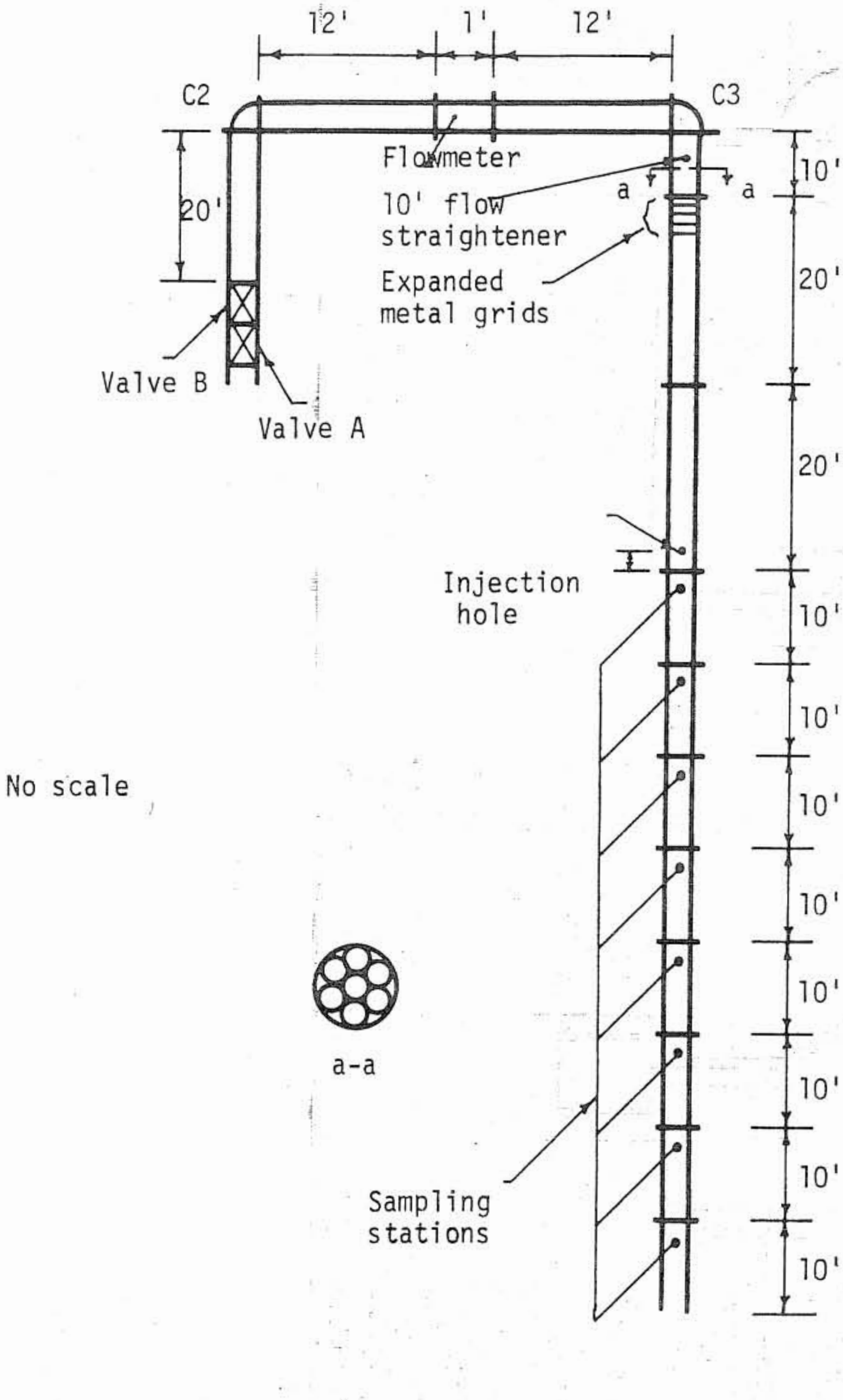

FIGURE 9: Schematic diagram of the hydraulic circuit

tanks were used in calibrating the flowmeter. Each tank had been calibrated in 1000 lb increments from 1000 lb through 20,000 lbs using dead weight loading. The read-out was accurate to ±20 lbs.

A flow straightener was included in the system to suppress any swirl resulting from elbow C3 (Fig. 9). The flow straightener consisted of

1. Four vanes placed in the elbow C3,
2. Seven 10-ft long, 1-1/4 in. IPS galvanized steel pipes (Fig. 9) inserted inside the 6 in. pipe immediately downstream of the elbow, and
3. A stack of five pieces of 5/16 in. flattened expanded metal placed 6 in. apart.

The length of straight pipe between the end of the expanded metal and the injection point was 76 pipe diameters and was sufficient for decay of the additional turbulence due to disturbances of the elbow and flow straightener and for establishment of fully developed turbulent pipe flow before the injection point [Dryden, 1942; Laufer, 1954].

Sampling stations downstream of the injection point were located 20 pipe diameters (10 ft) apart. Accessibility to any point in the cross section at these sampling stations was provided by the support and the traversing system shown in Fig. 10. The probe (Section 4.2.4.2) could traverse the entire pipe diameter and its location relative to the pipe wall could be read to an accuracy of 0.001 ft. The supporting pipe could be rotated a full revolution about the pipe centerline. This

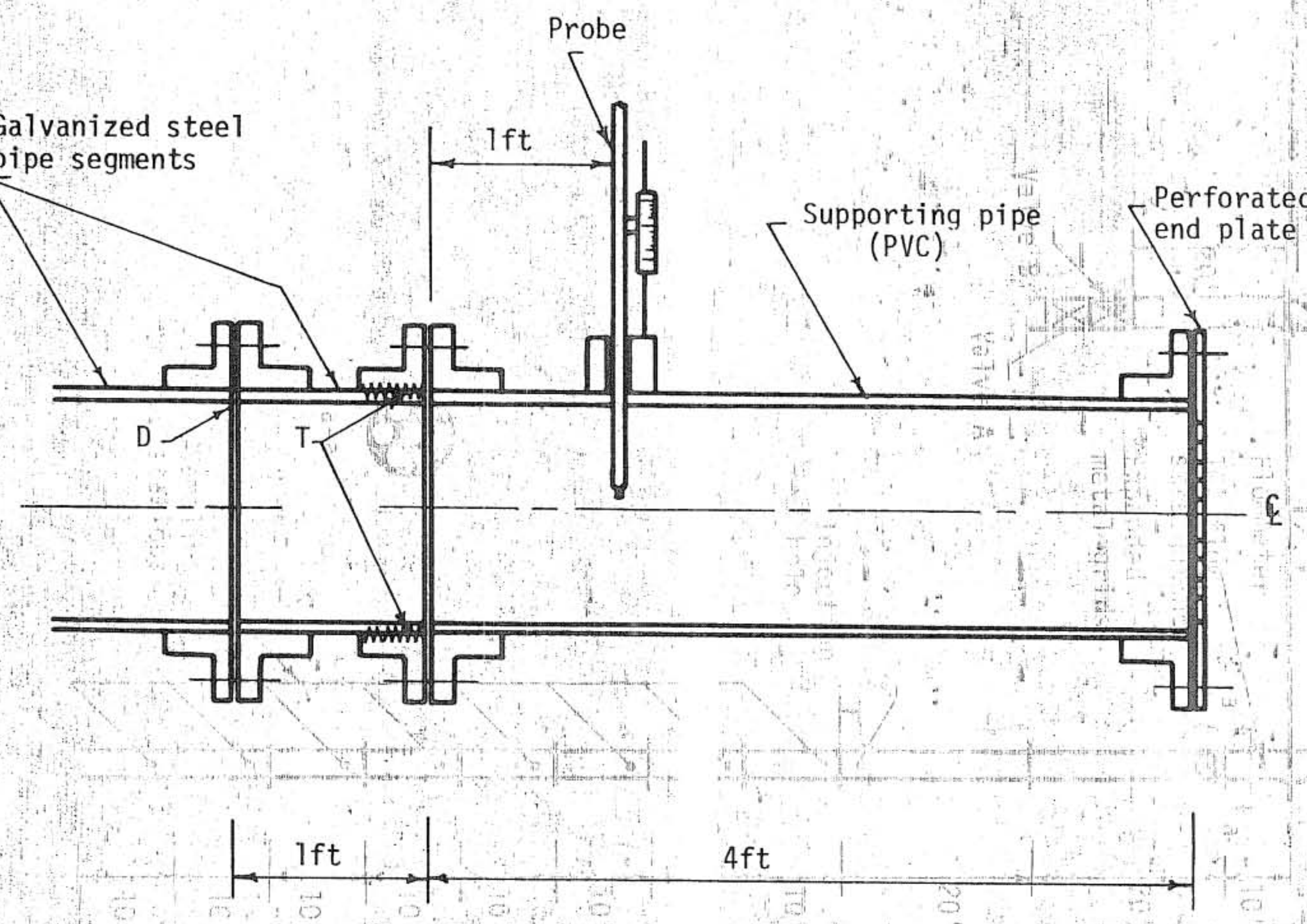

FIGURE 10: Schematic diagram of traversing mechanism and its support

rotation was achieved simply by rotating on the pipe threads indicated by T in Fig. 10. In other words, the probe axis could be set to any angle with the vertical. To move to a new sampling station, the 5 ft long measurement section was disconnected at point D, the required additional length of pipe was added, the measurement section was reattached at the end of the pipe, and the discharge was reset to the desired value.

The sections were connected by standard screw-on flanges. Care was taken to ensure that the inner surface of the pipe at the joints was as smooth as possible by threading the pipe ends so that the gap at the joints was at most 1/8 in. Also, each time that pipe sections were added, care was taken to align the inside surface of the pipes.

The hydraulic roughness of the pipe wall was determined empirically by measuring the head loss over a 90 ft length of pipe and measuring the corresponding discharge. The relative wall roughness was found to be 0.00001 (Fig. 11). Thus, flow was assumed to be in hydraulically smooth regime. The possible aging of the wall was also checked; no change in the wall roughness was observed during an 18 month period (Fig. 11).

During the 24-month period of testing, the temperature of the water varied between 20°C and 24°C. This variation was caused by a combination of factors: the pipeline was exposed to air, the water was recirculated, there was heating associated with the pumps, and there were changes in the temperature of the sump water. One effect of the variation in temperature was to change the viscosity of water and hence the Reynolds number corresponding to a given measured flow rate. With the

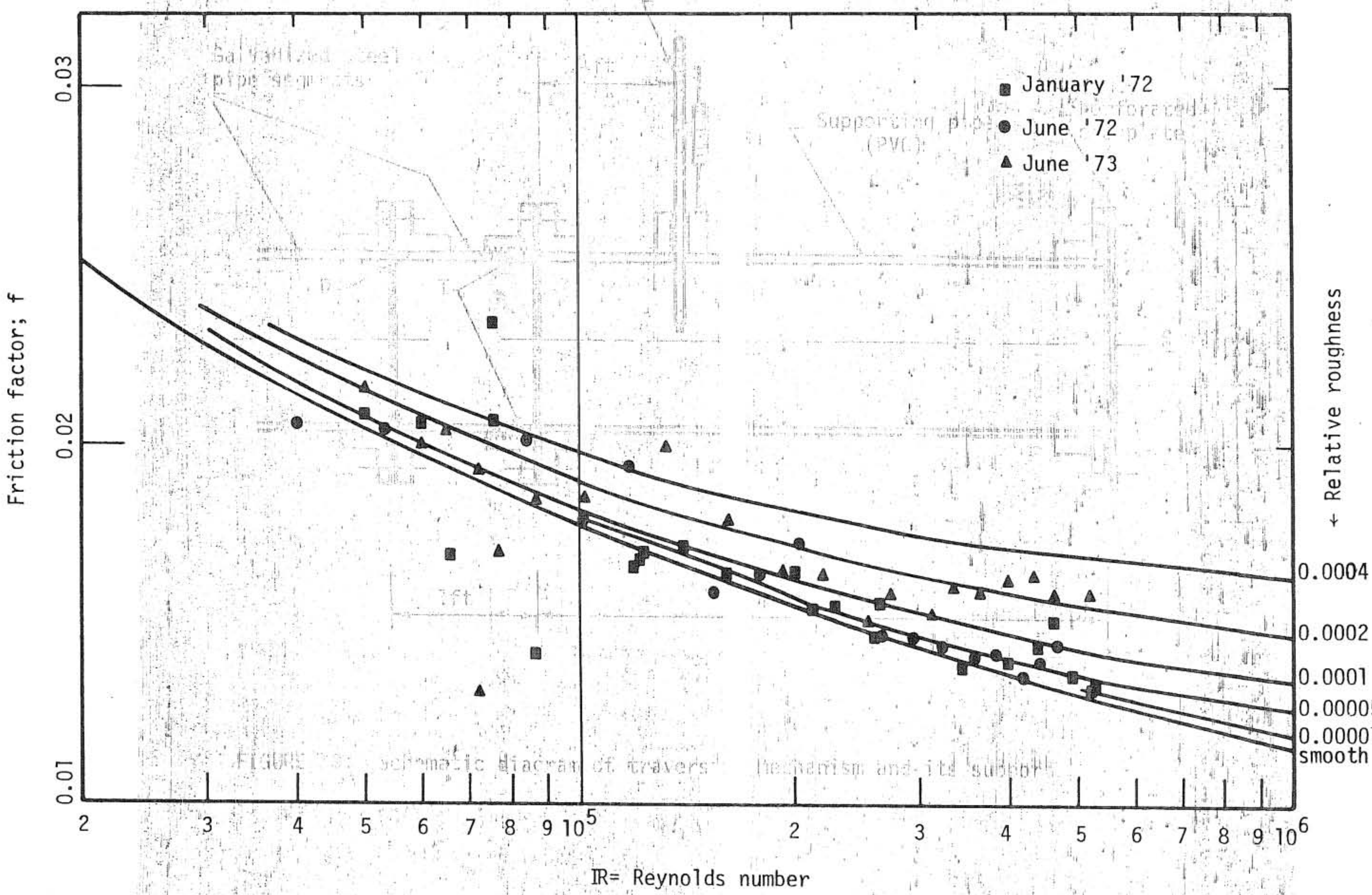

FIGURE 11: Observed friction factors

weak dependence of mixing distance on Reynolds number as observed in this study and elsewhere [Clayton, et al., 1968] and because of the relatively small temperature changes, the effect of temperature changes on the viscosity was considered insignificant and a representative value of viscosity at 22°C was used throughout.

4.2.2 Velocity Measurements

Velocity distributions were measured to check the axismmetry of the pipe flow and to obtain the discharge by integration of the velocity for comparison with the flow meter. A 0.6 cm O.D. Prandtl-Pitot tube with a dynamic-head opening of 0.107 cm was used. The difference between the static and dynamic heads was measured by a tilting manometer. Heads were recorded to within 0.001 ft (vertical equivalent). The distribution of the measurement points over a cross section are as shown in the top part of Fig. 12. The velocity profiles at three Reynolds numbers were measured at the injection section and the sampling station 20 ft downstream of it. The measurements are summarized in Fig. 12. These distributions were fitted by a power law velocity distribution [Schlichting, 1968] as shown in Fig. 12, and used as an input to the mathematical model.

The discharge calculated by the integration of velocity distribution at a given section had an average deviation of less than 0.5 percent from the metered discharge. This discrepancy was considered as being due to experimental error. The metered discharge was therefore

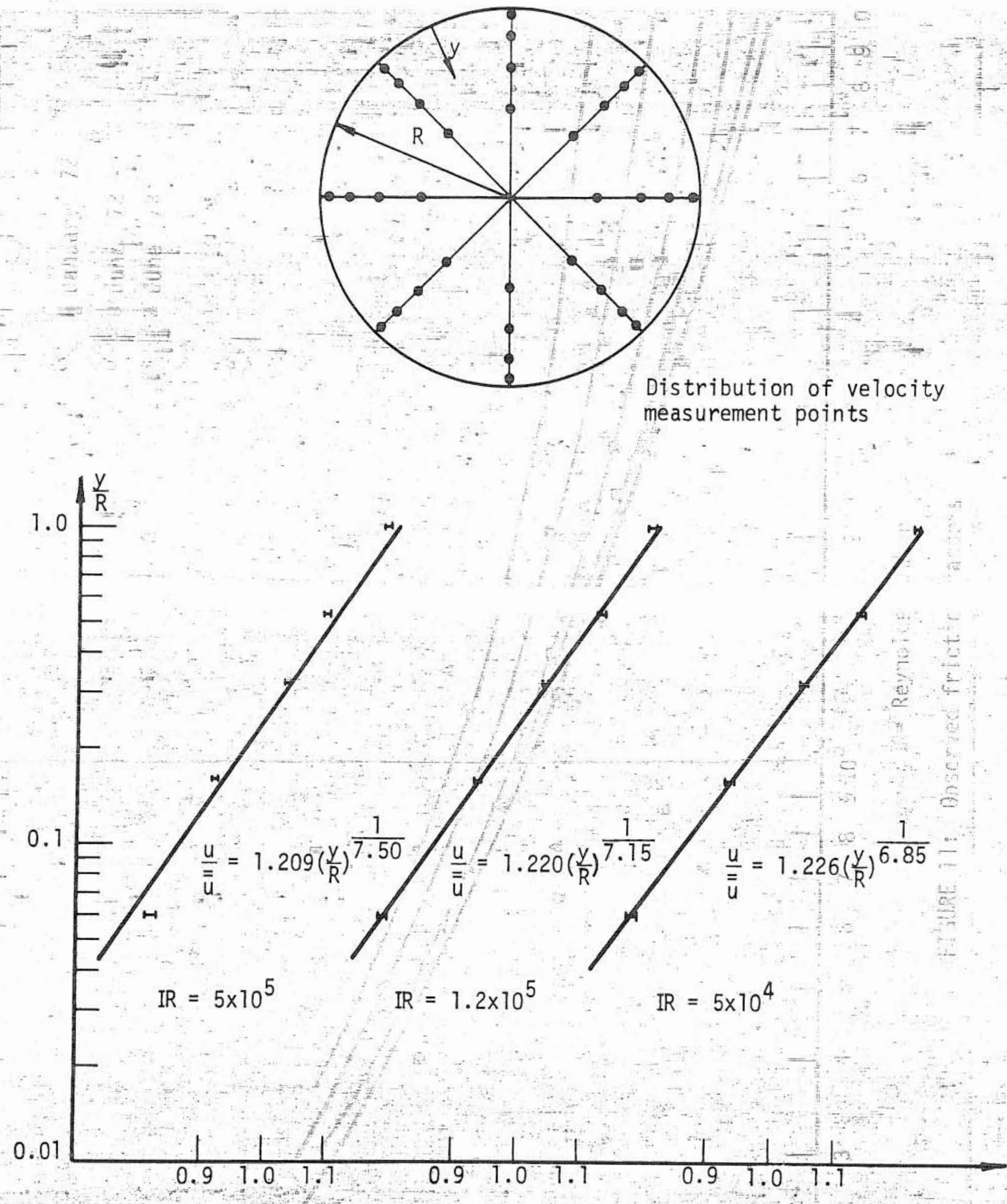

FIGURE 12: Typical measured velocity distributions

considered to be accurate and was used for calculation of the mean velocity in the pipe.

4.2.3 Tracer Injection

4.2.3.1 Selection of Tracer

In previous experimental determinations of mixing distance due to different injection systems, several tracers have been used. Radioactive tracers, fluorescent tracers and salt are the most commonly used tracers. The radioactive tracers (which mostly have relatively short half-life) require a storage of radioactivity. The use of fluorescent tracers, on the other hand, require the use of detection equipment which was not available. Therefore, in this study, sodium chloride (NaCl) was used as a tracer material; it was inexpensive and easily accessible, and its ionizing nature made it easily detectable. In what follows, sodium chloride will be called simply "salt."

4.2.3.2 Tracer Preparation

The salt was dissolved in the laboratory sump water in preparing the injection fluid. If salt were the only solute used, the density of the solution would always be greater than that of the laboratory water. However, for nonbuoyant jets the density of the injection solution was to be equal to that of the laboratory water. Thus, methanol was added to make the density of the injection solution equal to the density of the laboratory sump water. For buoyant jets, on the other hand, sugar was used to obtain a heavier injection solution whenever the increase in the density due to salt alone was not enough. The density of injection solution was measured to within three significant decimal digits by a Westphal specific gravity balance (Fischer Scientific, Catalog #2-150).

Since tracer conductivity was the distinguishing property to be measured during the experiments, the conductivities of the constituents of the tracer solution were measured with a standard conductivity probe. It was found that methanol and sugar were essentially nonionizing. This meant that the increase in conductivity during an experiment was due only to the salt.

4.2.3.3 Tracer Injection System

Figure 13 is a schematic diagram of the tracer injection system. The tracer solution (jet fluid) was stored in a reservoir (18 x 18 x 18 in^3). There were two injection circuits. Circuit C1 was used with valve VA completely open (and pump P off and valve VM closed). In circuit C1, the tracer flow rate was controlled by the metering pump PM (Chemcon, Series 1140-PVC-135) with the capacity of 50 GPH. The pump PM was a diaphragm pump which provided alternate suction and discharge strokes at a rate of 90 per minute. Therefore, the closed surge tanks were introduced into the circuit to damp out the fluctuations in the flow associated with the pump characteristics. The pressure gauge attached to the second closed surge tank was used to check the steadiness of the

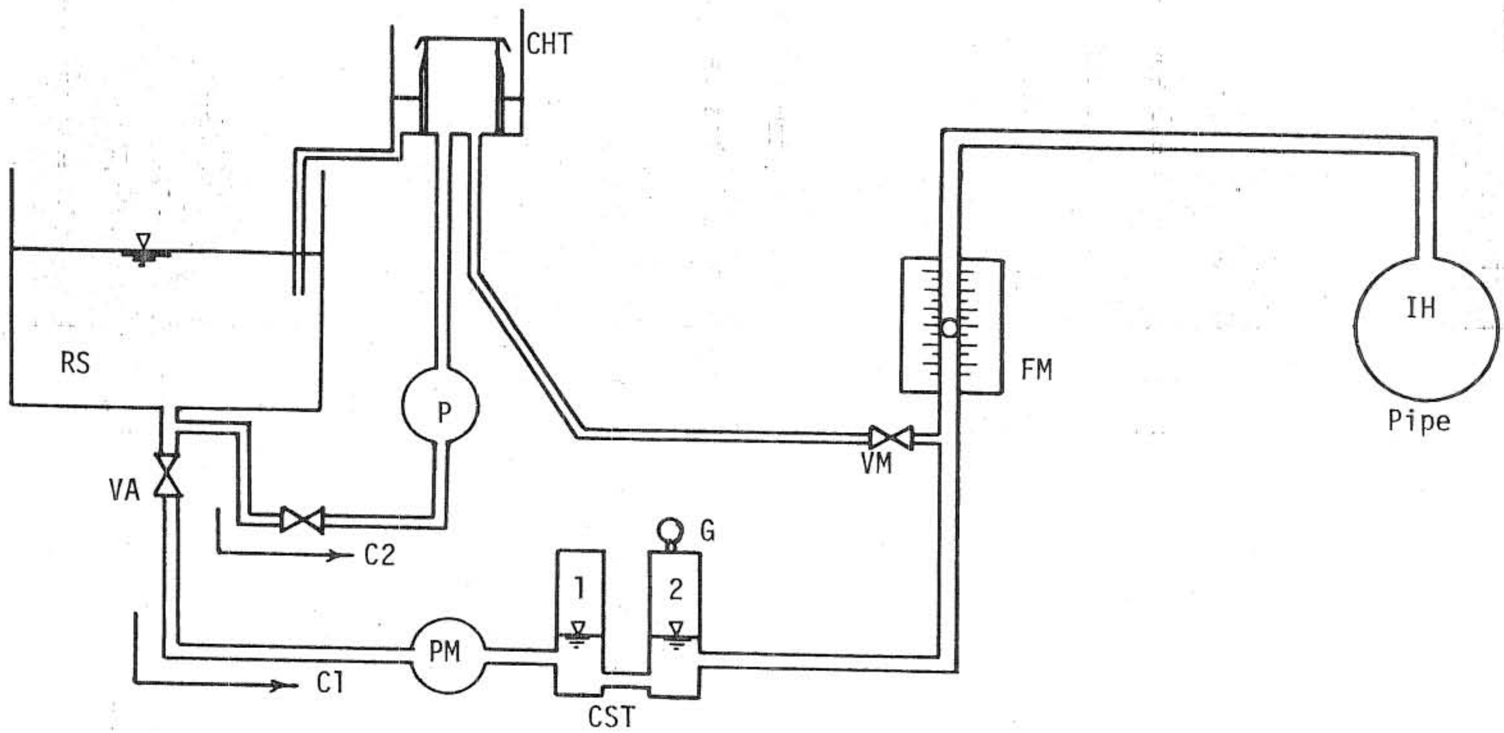

VA: Shut-off valve
G: Pressure gauge
VM: Metering valve
P: Pump
PM: Metering pump
CST: Closed surge tanks
RS: Reservoir
CHT: Constant head tank
C1: Circuit 1
C2: Circuit 2
FM: Flowmeter
IH: Injection hole

FIGURE 13: Schematic diagram of injection circuit

flow. It was assumed that the flow was steady when the pressure fluctuations became less than 1 percent of the average pressure. (The resulting jet was visually observed and appeared to be steady.) For flow rates greater than 300 ml/min, the transient period was short enough (less than 10 min.) to use this circuit. However, flow rates less than 300 ml/min, the transient period was too long to use circuit C1. Then, the circuit C2 was used. (An arbitrary time limit was imposed to prevent putting large quantities of salt into the pipe flow and the sump while waiting for a steady condition to be reached.) Circuit C2 was used with the valve VA closed. The tracer flow rate from the constant head tank was controlled by the use of a metering valve VM. (This circuit was not used for all flows because of the higher head requirements for flows greater than 300 ml/min.)

The flowmeter, FM, was a triflat, variable area flowmeter (FP-3/8-25-G-5, Fischer and Porter Company). It was calibrated by measuring the discharge collected in a calibrated beaker. It was found that within the range of the change in temperature of the injection fluid (1°C at most) observed from one experiment to another and within the sensitivity (0.5 percent accuracy) of the flowmeter, a single calibration curve was adequate for a series of experimental runs. A new curve was developed

1. When the density of the injection solution was changed,
2. When switching between the two injection circuits previously described.

The details of the injector used for jet injections are as shown in Fig. 14. The length H_i of the injector was chosen to be long enough ($H_i/d > 40$) to have fully-established flow when the jet entered the pipe. The flow inside the injection tube was always turbulent. A pressure tap located opposite to the injection hole was used to visually check the alignment of the jet with the jet discharging into an empty pipe.

In Fig. 15, the injector used for wall source is shown. The tracer solution was released exactly from the same location as the jet injection. The alignment of wall source probe was checked visually.

4.2.4 Concentration Detection Equipment

4.2.4.1 The Overall System

Conductance of a fluid changes as the concentration of ionizing agent (salt) changes. Thus, concentration distributions of an ionizing agent can be obtained from the measured conductivity distributions. The concentration detection equipment (Fig. 16) for the laboratory measurements consisted essentially of a conductivity probe which formed a part of a Wheatstone bridge circuit.

4.2.4.2 The Conductivity Probe

The conductivity probe (Fig. 17) constructed for this study consisted of two platinum electrodes of 1/8 in. x 1/8 in. x 1/192 in. placed 1/8 in. apart at the base of a glass tube (Corning Pyrex Brand

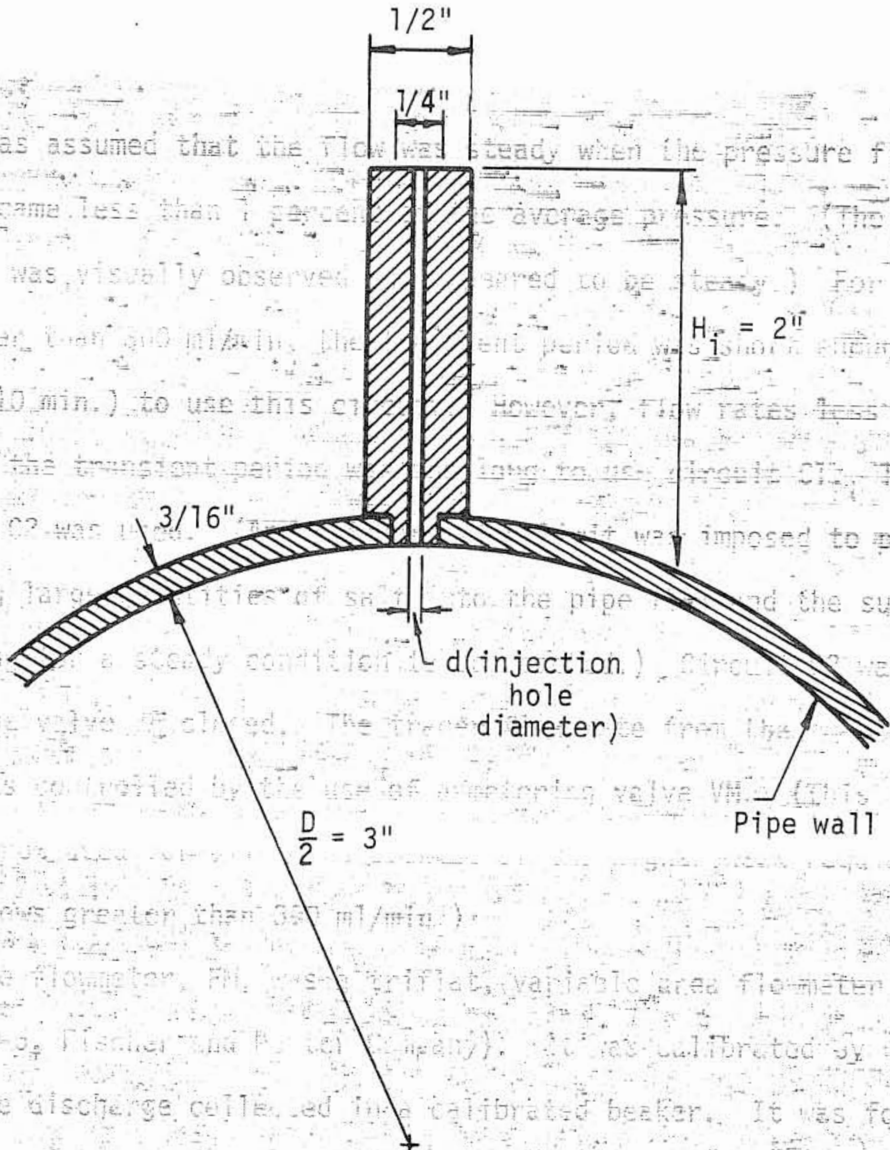

FIGURE 14: Schematic diagram of jet injector

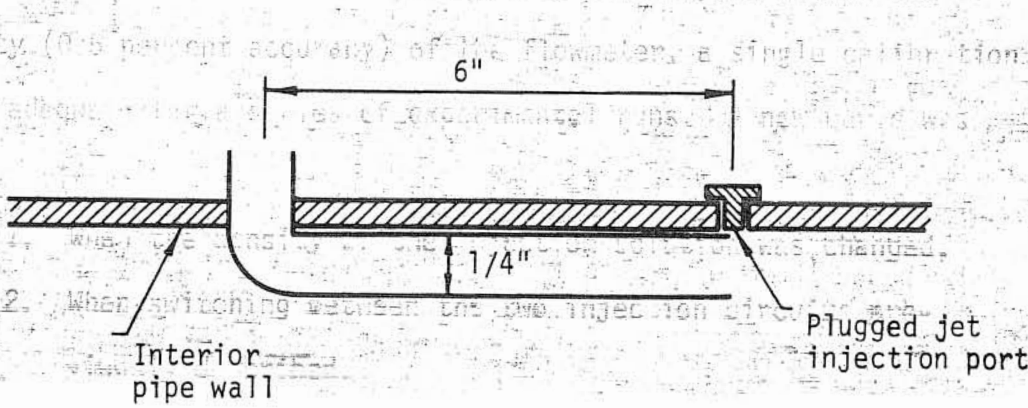

FIGURE 15: Schematic diagram of simple wall source

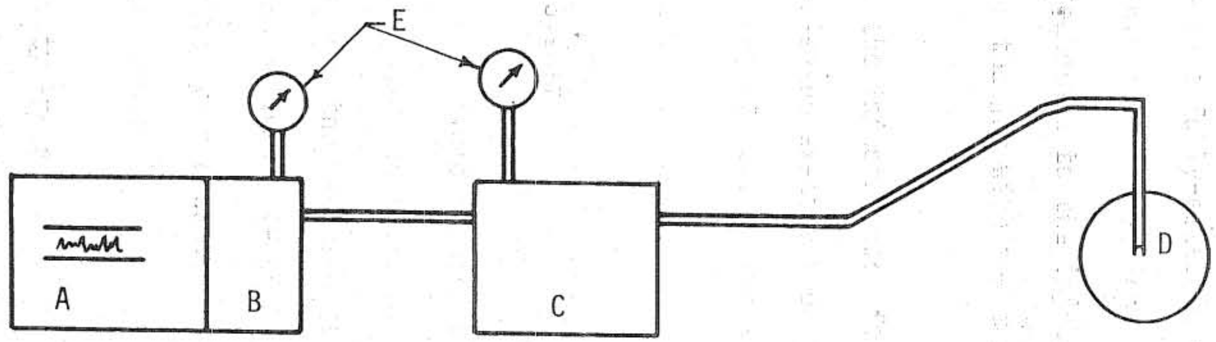

A: Recorder
B: Preamplifier
C: Bridge circuit (See figure 19)
D: Probe
E: Voltmeters

FIGURE 16: Schematic diagram of concentration detection circuit

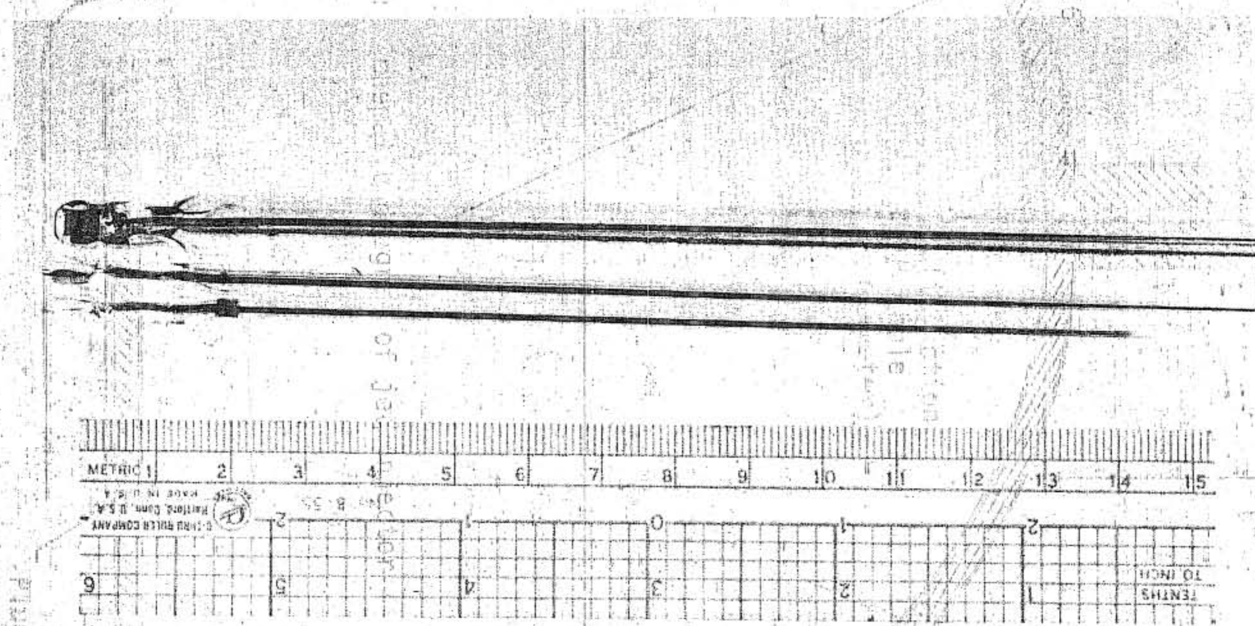

FIGURE 17: The conductivity probe

7740) of 8 mm-outside diameter (Fig. 18). A platinum wire, 0.65 mm in diameter, was flattened at the one end to 1/192 in. thickness to obtain the electrodes. The unflattened ends of the platinum wires were butt-welded by plasma arc to copper wires of the same outside diameter to form the leads from the electrodes. These leads, then, were isolated from one another by glass tubing (Corning Pyrex Brand 7740) of 3 mm outside diameter, and 3 mm glass tubing was evacuated. The probes had a total length of approximately 18 in.

Before first use, and later whenever readings become erratic each probe was cleaned and platinized according to a standard chemical method as described by Glover [1970]. (See Appendix 1.) The probes were stored in distilled water when not in use.

4.2.4.3 Bridge Circuit

The probe was connected to the bridge circuit by a two conductor shielded cable. As shown in Fig. 19, the preamplifier supplied the excitation voltage for the bridge (4.5 volts, 2400 Hz) and received the input signal of the probe through the bridge circuit. The probe was connected across the third leg of the bridge. The variable condenser connected to the leads A and B and the 2 KΩ variable potentiometer in the third leg of the bridge circuit offered flexibility in the initial balancing of the bridge circuit. A voltmeter was connected to the bridge circuit as shown in Fig. 4 to check the initial balancing of the bridge. Furthermore the 10 KΩ variable potentiometer and 5 KΩ resistor connected across the bridge as shown in Fig. 19 provided the

1: Electrodes (Platinum)
2: Outer tubing (Glass)
3: Insulator tubing (Glass)
4: Platinum leads
5: Butt-weld
6: Copper leads
7: Filling (Glass)

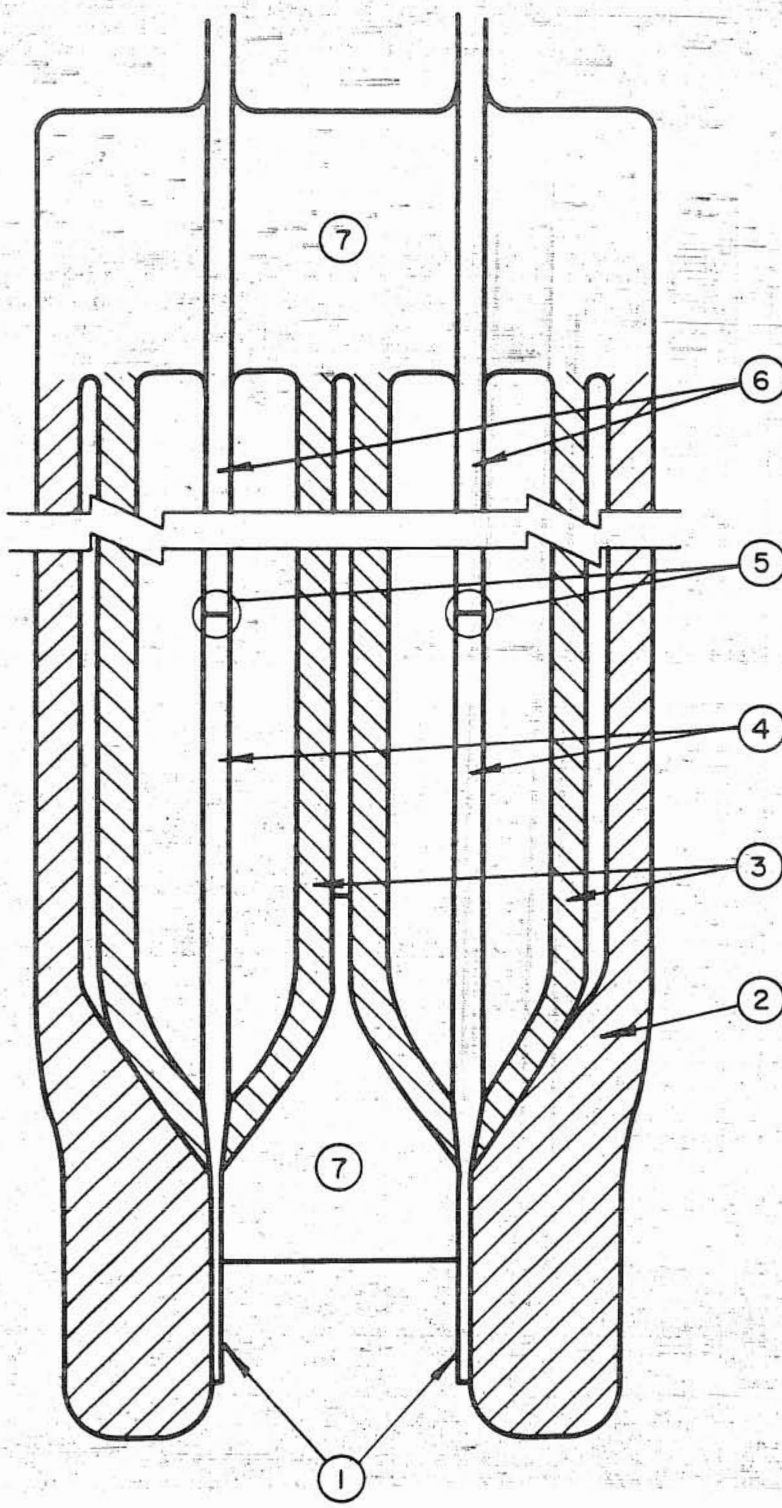

(Not to scale)

FIGURE 18: Details of the probe

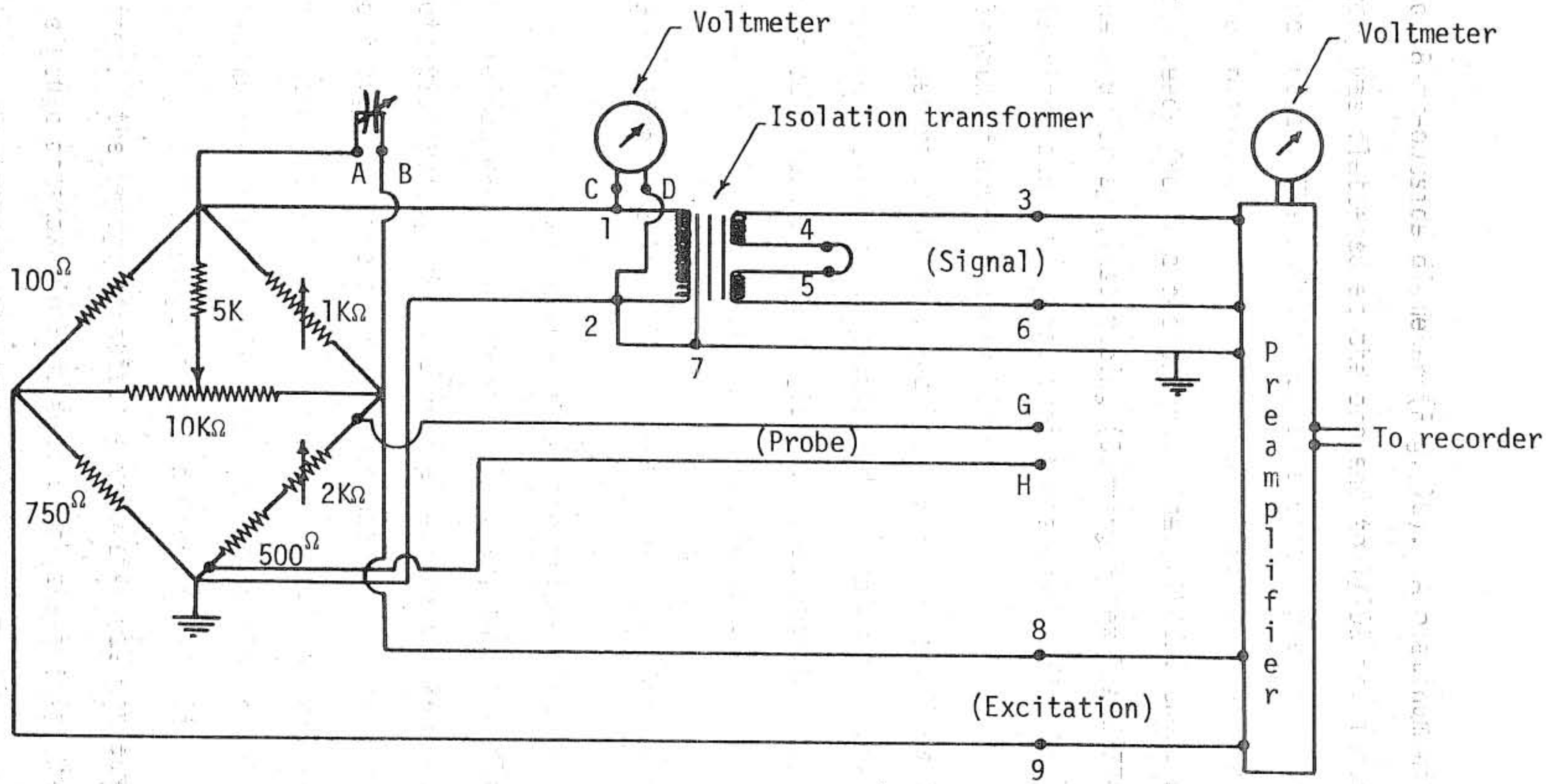

FIGURE 19: Circuit diagram of the bridge

possibility to vary the sensitivity of the probe when desired. The bridge was connected to the preamplifier via the signal and excitation leads (a four conducted shielded cable).

When a probe was immersed in flow with ionized salt in a grounded pipeline, the potential difference between the pipeline ground and instrument ground induced a ground loop. To eliminate this problem, an isolation transformer was installed in the signal circuit of the bridge as shown in Fig. 19. The bridge and the isolation transformer were grounded at the guard shield of the signal and excitation leads.

4.2.4.4 Recording Equipment

A two-channel Sanborn Recorder (Model 296) was used. The signal output from the preamplifier was continuously recorded on a strip chart. An averaging switch was also available so that the signal output could be averaged over a one-second period if desired.

Using the R (resistance) and C (capacitance) balance knobs of the preamplifier final balancing of the overall bridge preamplifier circuit was accomplished. A voltmeter was connected to the preamplifier output as shown in Fig. 19 to check the final balancing.

4.2.4.5 Calibration of Probes

Calibration of probes is required to obtain the relationship between the recorder output and the corresponding tracer concentration.

A constant temperature bath was used for calibration of the probes. Since the purpose of the probe was to measure the change in concentration relative to the background concentration, the constant temperature bath was filled with sump water. The probe circuit was balanced with the probe in the sump water. Then successively weighed quantities of salt were added to a known volume of water in the bath. Figure 20 shows a typical set of calibration curves obtained for one series of runs. All measured calibrations were linear within the accuracy of reading of the recorder for concentration levels up to 70 mg/ℓ of sodium chloride above the background concentration (or above the bridge balance point). For a given probe, the same calibration curve was obtained when starting at different balance points. The minimum concentration that could be accurately measured by the probes and associated circuitry was 0.5 mg/ℓ. The resistance of the probe immersed in water was measured to be 20 KΩ at 20°C and 200 mg/ℓ background concentration.

Calibration of probes were checked after completion of each series of runs. The probes were recalibrated after each platinization.

4.3 Experiments

4.3.1 Dimensional Considerations

The mixing distance x_m depends on the characteristics of both the jet and the pipe flow. For constant density, fully-established uniform pipe flow, the flow characteristics can be represented by the diameter D of the pipe, the average flow velocity $\bar{\bar{u}}$, the viscosity μ,

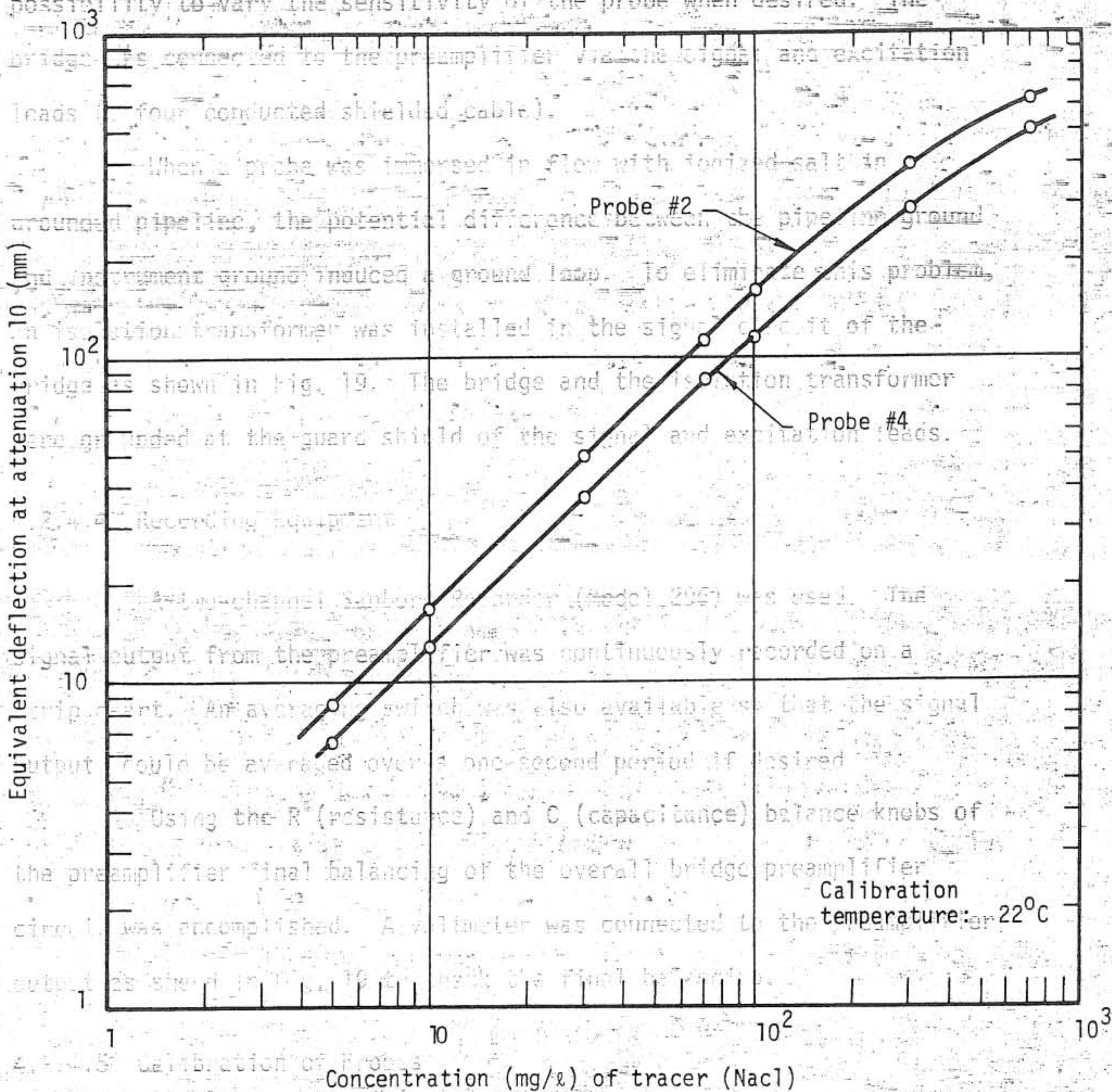

FIGURE 20: Typical calibration curves

and the mass density ρ_a. Since, in this investigation, only pipes with a single relative roughness are considered, the surface roughness of the pipe is not listed among the significant pipe flow parameters. The jet flow, on the other hand, can be characterized by the injection hole diameter d, the injection velocity u_o, and the difference in specific weight $\Delta\gamma$ between the jet fluid and the ambient fluid. The geometry and the orientation of the injection hole are not cited as significant parameters since only one type of injection hole (a circular one perpendicular to the pipe wall) was used throughout this investigation. In addition to the jet and pipe flow characteristics, the mixing distance depends on the degree of completeness of mixing of the tracer which is considered as adequate. The standard deviation σ of the concentration measurements at a given cross section is used as a measure of degree of completeness of mixing. (A more complete discussion of completeness of mixing and σ is given in Section 4.3.2.) Thus, the relationship among the variables can be indicated as

$$x_m = f_1\ (D,\ \rho_a,\ \mu,\ \bar{\bar{u}},\ d,\ u_o,\ \Delta\gamma,\ \sigma) \tag{4-1}$$

By application of Buckingham's π theorem and some further manipulations, Eq. 4-1 can be reduced to a simpler form:

$$L = f_2\ (D_r,\ k,\ \mathbb{F}_d,\ \mathbb{R},\ \sigma) \tag{4-2}$$

where L is the dimensionless mixing distance,

$$L = \frac{x_m}{D} \tag{4-3}$$

D_r is the ratio of pipe diameter to the injection hole diameter,

$$D_r = \frac{D}{d} \tag{4-4}$$

k is the velocity ratio,

$$k = \frac{u_o}{\bar{\bar{u}}} \tag{4-5}$$

$\mathbb{F}_d$ is the densimetric Froude number,

$$\mathbb{F}_d = \frac{u_o}{\sqrt{\frac{\Delta\gamma}{\rho_a} d}} = \frac{u_o}{\sqrt{\frac{\Delta\rho_o}{\rho_a} gd}} \tag{4-6}$$

$\mathbb{R}$ is the Reynolds number,

$$\mathbb{R} = \frac{\bar{\bar{u}}\ \rho_a\ D}{\mu} \tag{4-7}$$

g is the gravitational acceleration, and $\Delta\rho_o$ is the initial density disparity between jet and pipe flow.

Experiments were conducted in flows covering a range of conditions with different D_r, k and $\mathbb{F}_d$ for $\mathbb{R}$ = 60,000. The dependence of L on Reynolds number will be discussed in Chapter 5. The range of conditions covered in this investigation are as shown in Table 5.

4.3.2 Measure of Degree of Completeness of the Mixing (Adequacy of Mixing)

As defined earlier (Chapter 1), the mixing distance is the distance between the injection point and some downstream location where

Table 5

Summary of Experimental and Numerical Runs

Series	Type of Injection	D_r	$\mathbb{F}_d$	k	$\Delta\rho/\rho_a$	u_o (fps)	$q/Q \times 10^5$	$\mathbb{R}_j$	Remarks[6]
1[1]	SS[3]	-	-	-	0.	1.3	174.	-	0
2[2]	SS	-	-	-	0.	2.0	174.	-	0
3	N[4]	96	∞	2	0.	2.4	21.6	1250	1
4	N	96	∞	4	0.	4.8	43.2	2500	0
5	N	96	∞	8	0.	9.6	84.4	5000	0
6	N	96	∞	10	0.	12.	108.	6250	0
7	N	96	∞	12	0.	14.4	129.6	7500	0
8	N	96	∞	16	0.	19.2	168.8	10000	0
9	B[5]	96	26	4	0.2	4.8	43.2	2500	1
10	B	96	52	8	0.2	9.6	84.4	5000	0
11	B	96	104	16	0.2	19.2	168.8	10000	0
12	N	192	∞	8	0.	9.6	21.8	2500	0
13	N	192	∞	16	0.	19.2	43.7	5000	0
14	N	192	∞	24	0.	28.8	65.5	7500	0
15	N	192	∞	32	0.	38.4	87.4	10000	2
16	N	96	∞	14	0.	16.4	152.2	8750	2
17	N	48	∞	4	0.	4.8	171.5	5000	2
18	N	48	∞	6	0.	7.2	257.2	7500	2
19	N	48	∞	8	0.	9.6	342.9	10000	2

[1] $\mathbb{R} = 7.7 \times 10^4$

[2] $\mathbb{R} = 10.0 \times 10^4$

[3] SS Simple source at the wall

[4] N Simple momentum jet (nonbuoyant)

[5] B Buoyant jet

[6] 0 Both numerical and experimental runs are performed
1 Only experimental runs are performed
2 Only numerical runs are performed

adequate mixing has taken place. The standard deviation σ of the concentration distributions normalized with respect to the cross sectional average concentration at each measurement station were used to evaluate the degree of completeness of the mixing. At a given section represented by the index k, the standard deviation σ_k was calculated numerically by

$$\sigma_k = [\sum_i \sum_j w_{i,j} (c_{k,i,j} - 1.0)^2]^{1/2} \tag{4-8}$$

with

$$w_{i,j} = \frac{a_{i,j}\, u_{i,j}}{Q} \tag{4-9}$$

where i and j are the indices describing the position of the measurement point, $c_{k,i,j}$ is the normalized concentration, $w_{i,j}$ is the weighting coefficient which reflects the nonuniformity of velocity distribution and uneven distribution of the observation points across a cross section, $u_{i,j}$ is the velocity at the point (i,j), $a_{i,j}$ is the area defined by the perpendicular bisectors of the line segments between the point (i,j) and the neighboring points, and Q is the flow rate in the pipe.

A value of zero for the standard deviation σ_k would indicate complete mixing. Theoretically, this ultimate value of zero is approached asymptotically, meaning that an infinitely long pipe would be required for complete mixing to take place. (Experimentally, σ_k approaches some constant value which is governed by experimental errors.) For practical purposes, adequate mixing is defined to have occurred when the standard deviation σ_k is smaller than some specified value, for example 0.01.

4.3.3 Procedure for a Typical Run

First the desired test conditions (k, D_r, $\mathbb{F}_d$) were determined. From these parameters plus $\mathbb{R}$ = 60,000, the required $\Delta\rho_0$, injection rate, and pipe discharge could be calculated. The tracer solution was prepared to give a concentration at the last measurement station which would be large enough to be measured accurately. The sump was mixed to eliminate fluctuations in background conductivity and temperature. A calibrated probe was placed in the traversing support and inserted into the pipe flow such that the flow continuously flushed the volume between the electrodes (i.e., the electrodes were parallel to the pipe axis). The concentration detection circuit, i.e., the bridge circuit, was balanced at the background concentration of the sump. Then the tracer is injected continuously at the predetermined constant rate. After allowing ten minutes for establishment of a steady state, tracer concentrations within the cross section were recorded. The distribution of measurement points within a cross section was governed by an estimate of what part of the cross section would be occupied by the tracer. (All of the data is available separately [Ger and Holley, 1974].) After the measurements were completed at the first cross section, the flow was stopped using valve A shown in Fig. 9, the measurement section was removed, the required additional pipe length was added being careful to align the inner pipe surfaces, the measurement section was placed at the end of the pipe, valve A was reopened, and the probe circuit was rebalanced at the (new) background concentration. The change in the

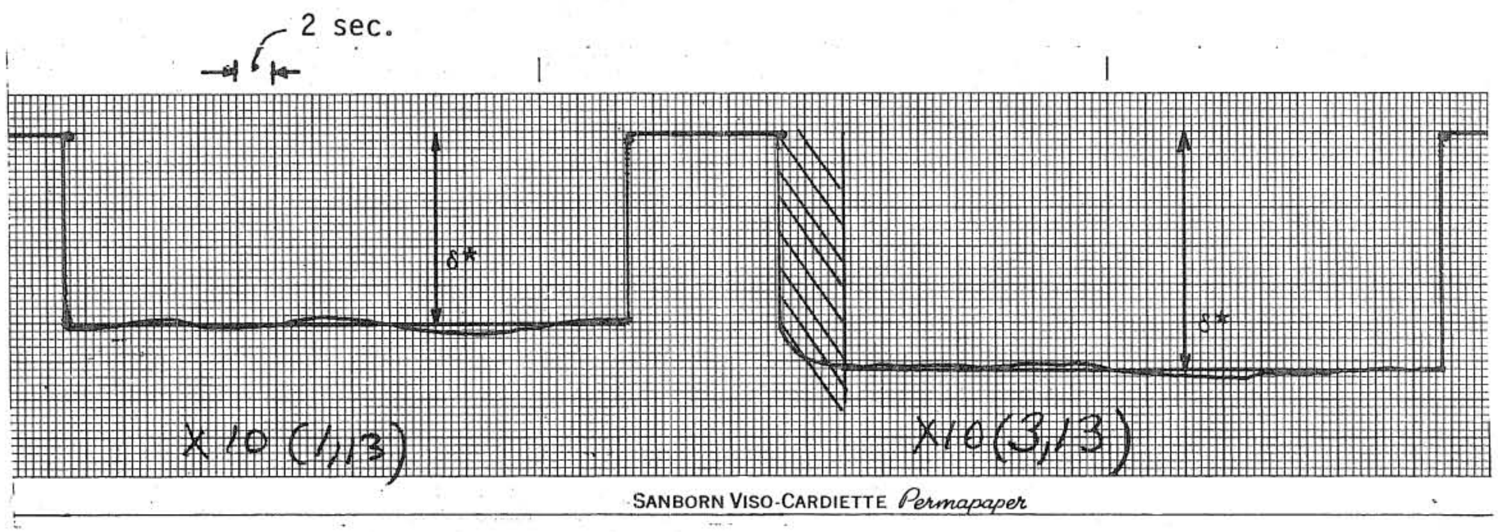

FIGURE 21: A typical data record with 1 sec averaging; run #05-44

length of the pipe line did not significantly affect the overall headloss in the hydraulic circuit and therefore did not alter the discharge.

A typical data record is shown in Fig. 21. The averaging switch of the preamplifier permitted the fluctuations in the signal to be automatically averaged over a one-second period. This smoothed record of concentration was used to obtain the time-mean concentration c as discussed below. First, the area beneath the record was determined by counting squares. Then, the apparent time-mean deflection of stylus, δ^*, was obtained by dividing the area beneath the record by the time span over which recording was made. Since the laboratory water was recirculated, the salt content of the laboratory water increased slowly during a run so that it was necessary to make a correction in the background reading. Therefore δ^* was reduced to the time-mean deflection δ corresponding to the tracer concentration by the formula

$$\delta\ (t_r) = \delta^*\ (t_r) - \Delta\,\frac{t_r - t_b}{t_e - t_b} \tag{4-10}$$

where t_r is the time of recording, t_b is the time at which the bridge was balanced, t_e is the time of recording the background concentration at the end of a set of measurements, and Δ is the deflection of stylus due to net change in the background concentration during the run. This correction was applied separately for each run. This correction assumes a linear variation of the background reading with time. This is equivalent to a linear variation of background concentration. The largest change in the background concentration for any test was 1 mg/ℓ or 2 percent of δ^*. For any point, the time-mean concentration c was then computed by

$$c = K \left(\frac{a_t}{10}\right) \delta \qquad (4\text{-}11)$$

where a_t is the recorder attenuation used during the measurement and K is the calibration factor to convert from mm-deflection at attenuation 10 to mg/ℓ concentration of salt.

The temperature of the flow did not vary more than 0.5°C during any run. This temperature did not significantly affect the conductivity measurements since a change 0.5°C gives the same conductivity change as 0.5 mg/ℓ of tracer and 0.5 mg/ℓ is the limit of accuracy of the probe circuit (Section 4.2.4.5).

4.3.4 Coding of the Experiments

Since experimental numbers will be used later to refer to test conditions, the code for identification of the runs is given here. The run was designated by two numbers. The first number refers to a particular set of injection and pipe flow characteristics as summarized in Table 5, and the second number refers to the distance, in pipe diameters, between the injection point and the section at which concentration distributions are recorded. For example, Run 13-044 refers to the measurements made at 44 pipe diameters downstream of the injection point for $D_r = 192$, $k = 16$, $\mathbb{F}_d = \infty$, and $\mathbb{R} = 60{,}000$. (See Table 5.)

5. PRESENTATION AND DISCUSSION OF RESULTS

5.1 Objectives

The primary objective of the experimental work was to evaluate the mixing distance due to a jet located at the wall of the pipe issuing perpendicularly in a crossing, fully-established turbulent pipe flow. In this chapter, experimental findings and the results of the mathematical model are presented and discussed. The evaluation of empirical coefficients used in the theoretical analysis is also provided. The experimental and numerical results are compared with those previously obtained for different injection systems by other investigators.

5.2 Centerline Injection

5.2.1 A Relation for Mixing Distances due to a Simple Centerline Source

As mentioned earlier, the diffusion equation (Eq. 3-75 has an analytical solution for a simple, nonbuoyant centerline source emitting continuously into a fully-established pipe flow if uniform velocity and radial diffusivity assumptions are made. In Chapter 2 (Eq. 2-11), the analytical solution which is applicable for axial distances longer than 30 pipe diameters was shown to be

$$c = 1 + \exp\left[-\frac{e_2\,\alpha_1^2\,x_1}{R^2\,\bar{\bar{u}}}\right]\frac{J_o(\alpha_1\,x_2/R)}{J_o^2(\alpha_1)} \qquad (5\text{-}1)$$

where symbols are as previously defined for Eq. 2-11.

The definition of standard deviation, σ, when the velocity is uniform, is

$$\sigma = \left[\frac{1}{A}\int_A \left(\frac{c}{\bar{c}} - 1.0\right)^2 dA\right]^{1/2} \tag{5-2}$$

where A is the cross-sectional area and $\bar{c}$ is the cross-sectional average concentration. Using Eq. 5-1 to evaluate σ, one obtains

$$\sigma = \frac{\sqrt{2}}{J_o^2(\alpha_1)} \exp\left(-2\alpha_1^2 \frac{e_2}{R\,\bar{\bar{u}}} L\right)\left(\int_0^1 \zeta\, J_o^2(\alpha_1\zeta)\, d\zeta\right)^{1/2} \tag{5-3}$$

where

$$L = \frac{x_1}{2R} \tag{5-4a}$$

$$\zeta = \frac{x_2}{R} \tag{5-4b}$$

Equation 5-3 gives the longitudinal variation of σ with the axial distance for a given set of conditions. Numerical evaluation of the integral in Eq. 5-3 gives

$$\int_0^1 \zeta\, J_o^2(\alpha_1\zeta)\, d\zeta = 0.0735 \tag{5-5}$$

Furthermore, in Section 2.3.1, it has been shown that the turbulent mass diffusivity e_2 can be expressed in terms of mean flow characteristics, for turbulent Schmidt number of unity, as

$$\bar{\bar{e}}_2 = 0.0256\,\sqrt{f}\,\bar{\bar{u}}\,R \tag{5-6}$$

where f is the Darcy-Weisbach friction coefficient. Using Nikuradze's data [Schlichting, 1968], the following power law type expression can be established for the friction factor f by curve fitting for Reynolds numbers varying from 10^4 to 10^6 and for smooth pipes:

$$f = \frac{0.204}{\mathbb{R}^{0.208}} \tag{5-7}$$

Substitution of Eqs. 5-5, 5-6, and 5-7 into Eq. 5-3 yields

$$\sigma = 2.37 \times 10^{(-0.148\ L\ \mathbb{R}^{0.104})} \tag{5-8}$$

or rearranging

$$L = 6.80 \log \left(\frac{2.37}{\sigma}\right) \mathbb{R}^{0.104} \tag{5-9}$$

In Eq. 5-9, the pipe is assumed to have smooth wall. Evans [1966] has observed that the mixing distance in a rough pipe is less than that in a smooth pipe at the same flow rate by the ratio of $\sqrt{f_{smooth}/f_{rough}}$, as previously shown by Taylor [1954]. This is in agreement with the argument of the exponential function in Eq. 5-3 which shows that L should vary inversely with e_2 for a given σ, or that L should vary inversely with $\sqrt{f}$ since e_2 is proportional to $\sqrt{f}$ (Eq. 5-6). Thus, Eq. 5-9 can be rewritten including the effect of pipe roughness or variable f for $10^4 \leq \mathbb{R} \leq 10^6$ as

$$L = 6.80 \log \left(\frac{2.37}{\sigma}\right) \mathbb{R}^{0.104} \sqrt{f_{smooth}/f} \tag{5-10}$$

where f is the actual friction coefficient.

Equation 5-10 can be used in predicting the mixing distances if

1. The mixing distance is larger than 30 pipe diameters,
2. The tracer is introduced as a continuous simple center-line source,
3. The Reynolds number is in the range 10^4 to 10^6, and
4. If the concentration distribution remains axisymmetric downstream of the injection point.

For larger Reynolds numbers, another similar expression could be obtained by replacing Eq. 5-7 by an appropriate expression for the variation of f.

5.2.2 Comparison of Theory and Experimental Results

In Fig. 22, experimentally observed mixing distances for a continuous point source of injection at the pipe center are compared with the mixing distances given by Eq. 5-10. There are large deviations in mixing distances observed by different investigators for given σ's for the same friction factor. These deviations are most likely because of the difficulty in obtaining perfectly axisymmetric conditions. For example, when the concentration distributions reported by Filmer and Yevdjevich [1967] are examined, it is seen that the bulk of the injected tracer moved upward within less than 24 pipe diameters downstream of the injection point. This might have been caused by a possible buoyancy effect resulting from different injection and ambient fluid

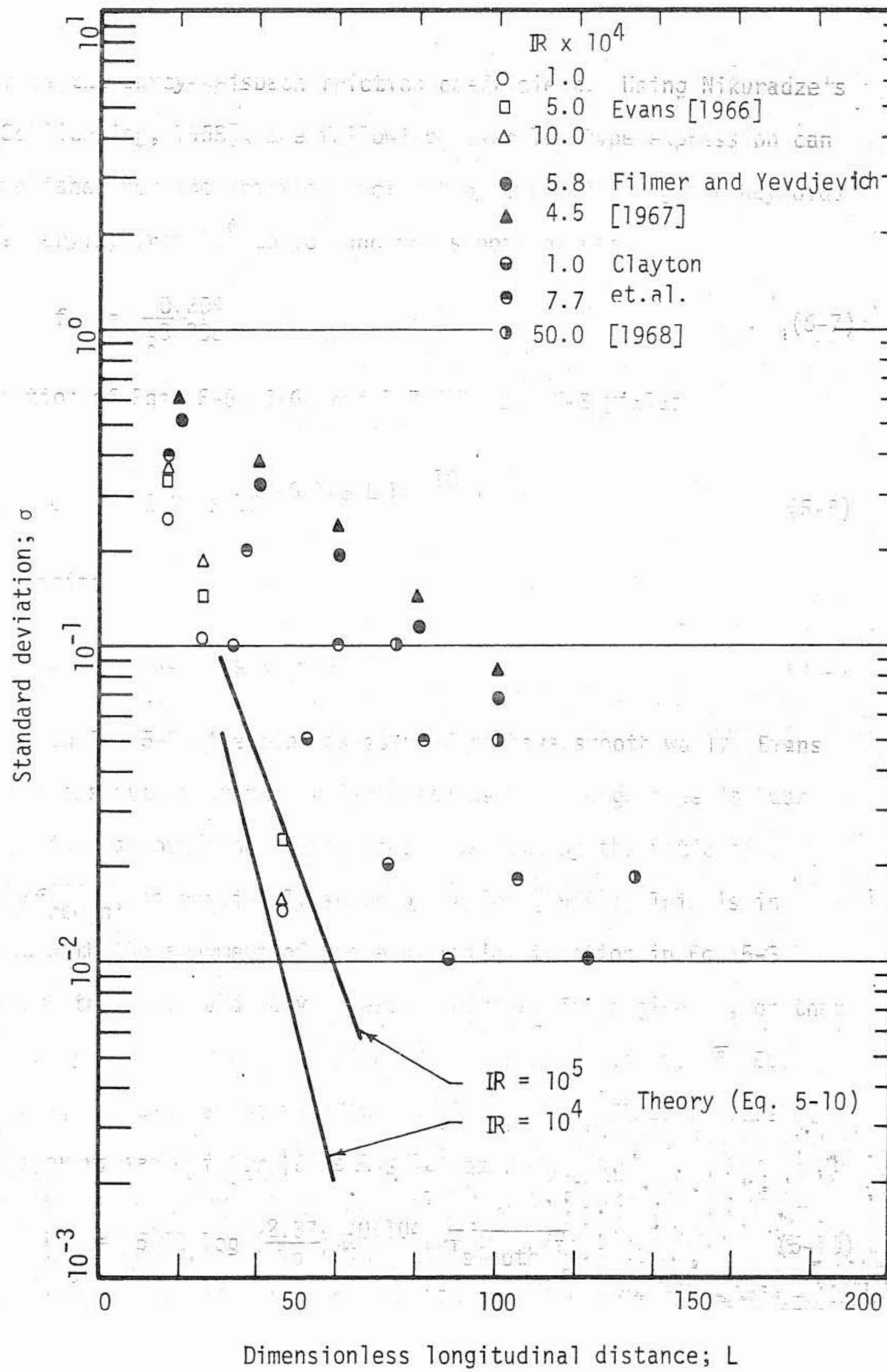

FIGURE 22: Variation of mixing with dimensionless longitudinal distance for a simple centerline source

temperatures and/or due to the wake of the arm supporting the injection tube [Filmer and Yevdjevich, 1967]. In the data of Clayton et al. [1968], their graphs of the measured concentration distributions indicate that the deviations from the theory can be attributed to the fact that the wake behind the arm supporting the injection tube might have caused the bulk of the tracer to move into the wake. Thus, in either case, the concentration distributions are far from being axisymmetric and the experimental mixing distances should therefore be expected to be greater than those calculated from Eq. 5-10. The mixing distances experimentally observed by Evans [1966] are very close to those of Eq. 5-10. The slight deviations, however, are probably due to spatial variation of velocity and diffusivity which have not been taken into account in obtaining Eq. 5-10.

5.3 Simple Source at the Pipe Wall

5.3.1 An Empirical Relation for Mixing Distances Due to a Simple Edge Source

As mentioned earlier, for a continuous simple source injector located at the wall of the pipe, Eq. 3-75 can be solved if it is assumed that the velocity distribution is uniform and that the radial and circumferential diffusivities are equal and uniformly distributed (i.e., $e_2 = e_3 = k_r$). Then an analytical solution is found to be (Eq. 3-91)

$$c = 1 + \sum_{n=0}^{\infty} w_n \cos n\, x_3 \sum_{m=1}^{\infty} \exp\left(-2\alpha_{n,m}^2 \frac{k_r L}{R\,\bar{\bar{u}}}\right) \frac{\alpha_{n,m}^2\, J_n(\alpha_{n,m}\, x_2/R)}{(\alpha_{n,m}^2 - n^2)\, J_n(\alpha_{n,m})} \qquad (5\text{-}11)$$

with

$$w_n = \begin{cases} 1 & \text{if } n = 0 \\ 2 & \text{if } n > 0 \end{cases} \qquad (5\text{-}12)$$

The definitions of symbols are as given for Eq. 3-91. The standard deviation σ (Eq. 5-2) becomes

$$\sigma = \left[\frac{1}{A} \int_A \left[\sum_{n=0}^{\infty} w_n \cos n\, x_3 \sum_{m=1}^{\infty} \exp\left(-2\alpha_{n,m}^2 \frac{k_r L}{R\, \bar{\bar{u}}}\right) \frac{\alpha_{n,m}^2 J_n(\alpha_{n,m} x_2/R)}{(\alpha_{n,m}^2 - n^2) J_n(\alpha_{n,m})} \right]^2 dA \right]^{1/2} \qquad (5\text{-}13)$$

In the analytical evaluation of the integral in Eq. 5-13 a difficulty arises, since, unlike the centerline injection case, more than one term of the series mustbe taken into account even for large L and the entire expression within the inner brackets must be squared before integrating. Therefore, rather than carrying out the integration in Eq. 5-13, it was assumed that the general form of the relationship among L, σ and $\mathbb{R}$ for a simple edge source injection remains the same as the centerline injection, i.e.,

$$L = A \log\left(\frac{I}{\sigma}\right) \mathbb{R}^n \sqrt{f_{smooth}/f} \qquad (5\text{-}14)$$

where A, I and n are constants yet to be evaluated, as discussed in the following paragraphs.

The factor $\mathbb{R}^n \sqrt{f_{smooth}/f}$ in Eq. 5-14 represents the variation of the friction factor and the turbulent diffusion coefficient with

Reynolds number and wall roughness. Therefore it was assumed that n should be independent of the location of the source. In other words, in Eq. 5-14, n was assumed to have a value of 0.104 as in Eq. 5-10.

In Fig. 23, experimentally observed mixing distances due to a simple source injector located at the wall of the pipe are shown. In this figure, σ was calculated for the data using Eq. 4-10. The general variation of the data points substantiates the logarithmic dependence of L on σ as indicated in Eq. 5-14. (Equation 5-14 is an equation of a straight line in the "log σ" vs. "L" plane.) Using the data in Fig. 23, the other unknown constants (A and I of Eq. 5-14) were evaluated as follows: I is the intercept of the straight line at L = 0. Using the available data as shown in Fig. 23, I was found to be 2.40. Substituting the value of I into Eq. 5-14 with n = 0.104, A was evaluated to be 20.5 by least square fit. ($A\mathbb{R}^n\sqrt{f_{smooth}/f}$ is the slope of a line in the log σ vs. L plane.) Furthermore, taking the empirical nature of the relation into account, the power n in Eq. 5-14 was rounded off to 0.10. The result is

$$L \;=\; 20.5 \log \left(\frac{2.40}{\sigma}\right) \mathbb{R}^{0.10} \sqrt{f_{smooth}/f} \qquad (5\text{-}15)$$

Because of the empirical nature of Eq. 5-15, the agreement between the theory and experiments (Fig. 23) is good. However, any use of Eq. 5-15 outside the Reynolds number range of 5,000 to 500,000 would involve extrapolation which has not been verified.

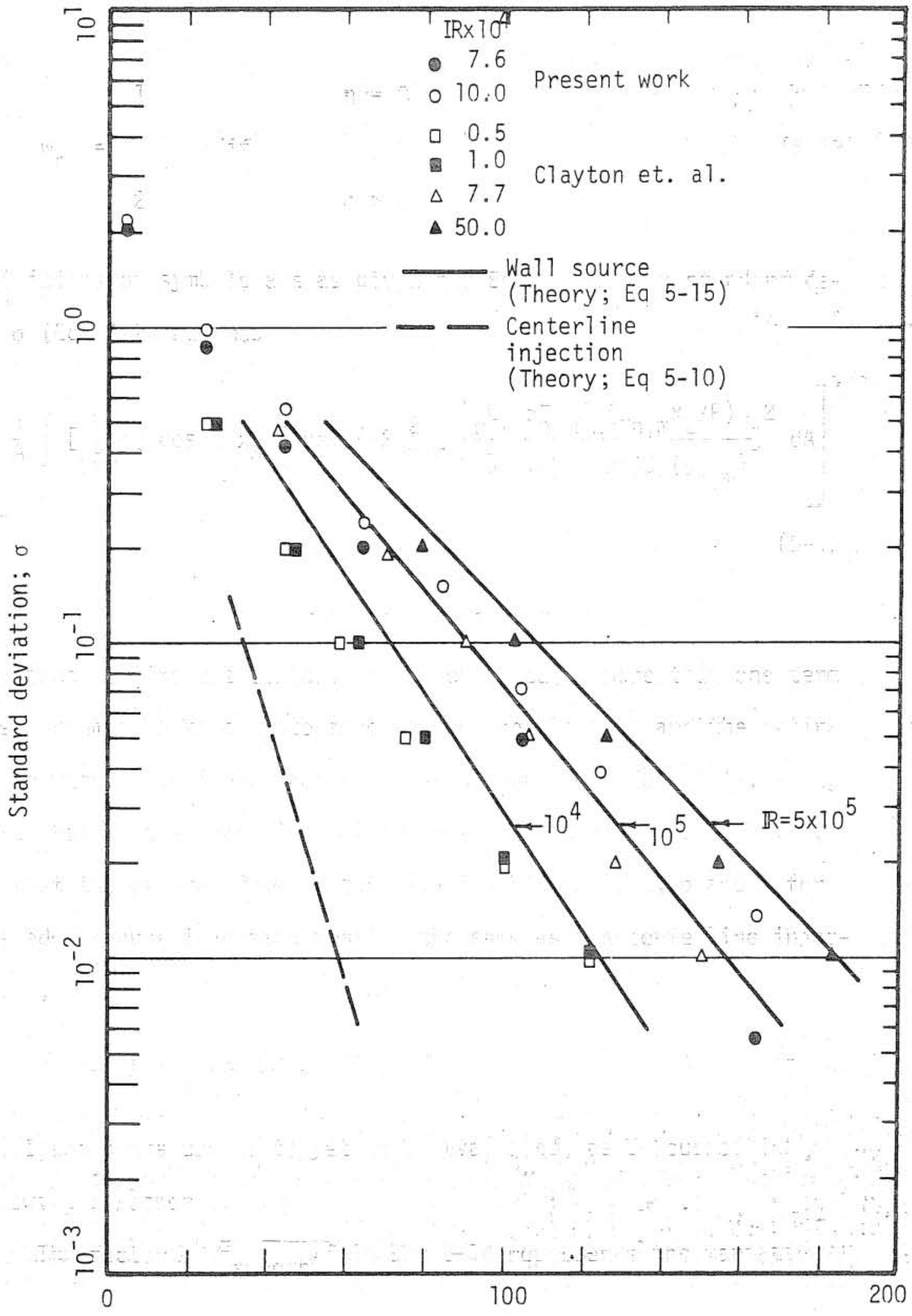

FIGURE 23: Variation of mixing with dimensionless longitudinal distance for a simple wall source

5.3.2 Evaluation of η

As stated earlier, if the diffusivities e_2 and e_3 are not equal and uniformly distributed, obtaining an analytical solution of the diffusion equation (Eq. 3-75) becomes complicated or perhaps impossible, depending on the functional form of e_2 and e_3. Therefore, it is more convenient to solve the diffusion equation (Eq. 3-75) by numerical methods. However, a priori knowledge of both the circumferential mass diffusivity (e_3) and the radial mass diffusivity (e_2) is essential for the numerical integration of the diffusion equation. It has been assumed (Eq. 2-25) that there is a linear relationship between e_2 and e_3 such that $e_3/e_2 = \eta$.

The ratio η was determined by matching the numerical solution (10 grid points along x_2, 32 grid points along x_3; Section 3.2.4.3) and experimental results for normalized concentration distributions using data from both the present work and from Filmer and Yevdjevich [1967]. The normalization was with respect to the average concentration obtained from the numerical solution for each measurement station. The numerical computations were carried out using the experimentally observed concentration distribution at the first sampling station as the upstream boundary condition. For the present experiments, the first sampling station was at four pipe diameters downstream the injection point; for Filmer and Yevdjevich [1967], it was at 27.4 diameters. For different η values, concentration distributions were calculated at several downstream locations corresponding to other sampling stations. It was assumed that the best η value was the one for which the standard error of discrepancy, S_d, between the numerical and experimental normalized concentration distributions was minimum. The standard discrepancy is defined as

$$S_d = [\sum_i \sum_j w_{i,j}(c_{i,j}^{(e)} - c_{i,j}^{(p)})^2]^{1/2} \tag{5-16}$$

where $w_{i,j}$ is the weighing coefficient as defined previously (Eq. 4-9), $c_{i,j}^{(e)}$ and $c_{i,j}^{(p)}$ are the normalized measured and predicted concentrations, respectively.

The variation in the standard discrepancy with longitudinal position and with various assumed values of η is shown in Figs. 24, 25 and 26. As is seen, the best η value is not constant, but rather tends to increase with distance (L). This tendency is possibly due to the type of functional relationship (Eq. 2-22) used in representing the spatial variation of diffusivities. This conclusion is supported by the observation that the parameter η should depend only on the flow characteristics, and thus should not vary with longitudinal position if the actual spatial variations were used. Nevertheless, an average η value can be obtained by taking the arithmetic means of the minimum η values (Table 6). This gives η = 1.35. Furthermore, when the variation in the standard deviation of the numerically obtained concentration distributions are compared with the experimentally observed variations (Figs. 27 and 28), it is seen that η values in the range of 1.2 to 1.5 provide good agreement between calculations and data. Therefore, the η value was selected as 1.35 for use in the mathematical model for the far field region.

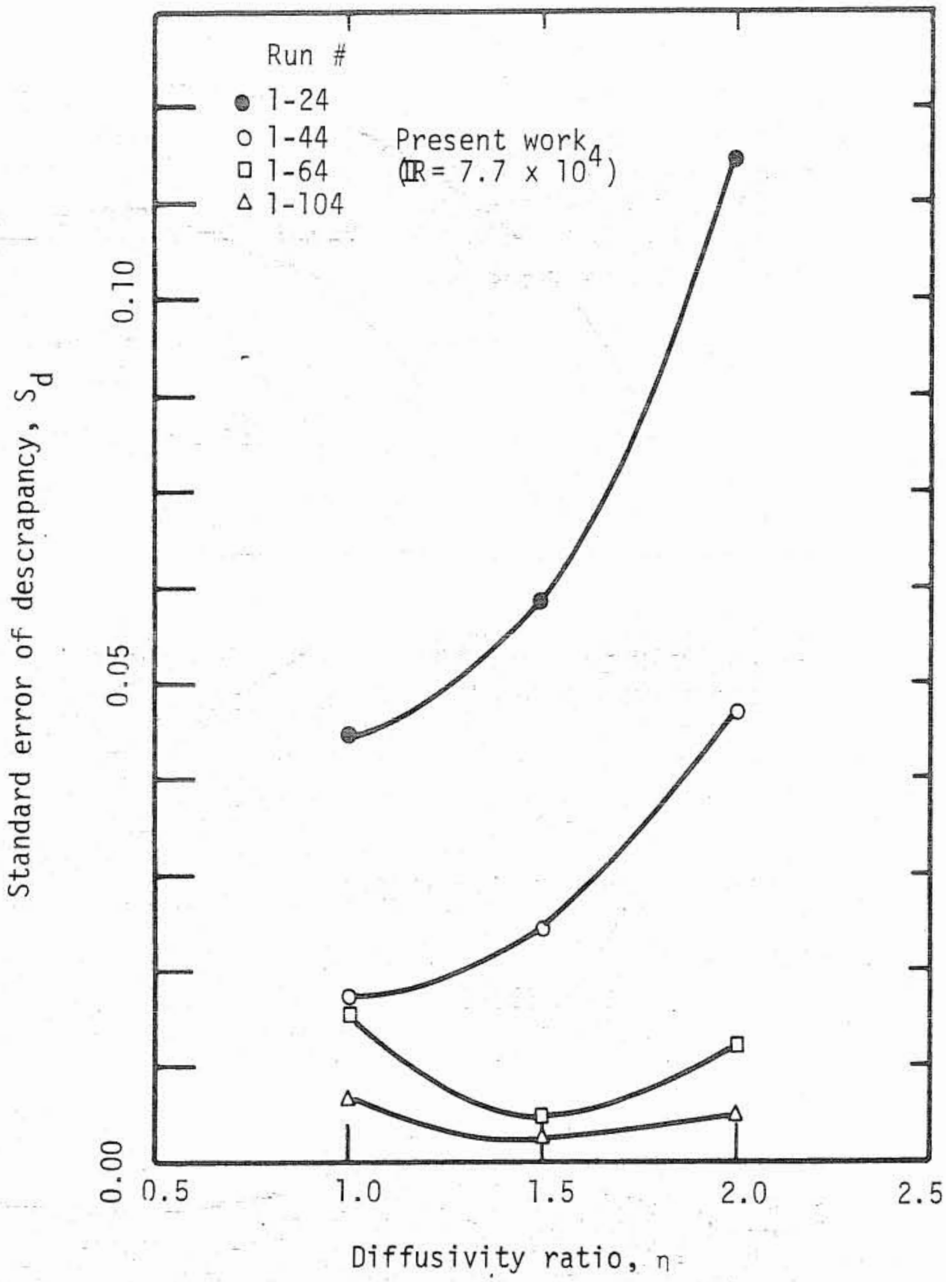

FIGURE 24: Variation of S_d with η

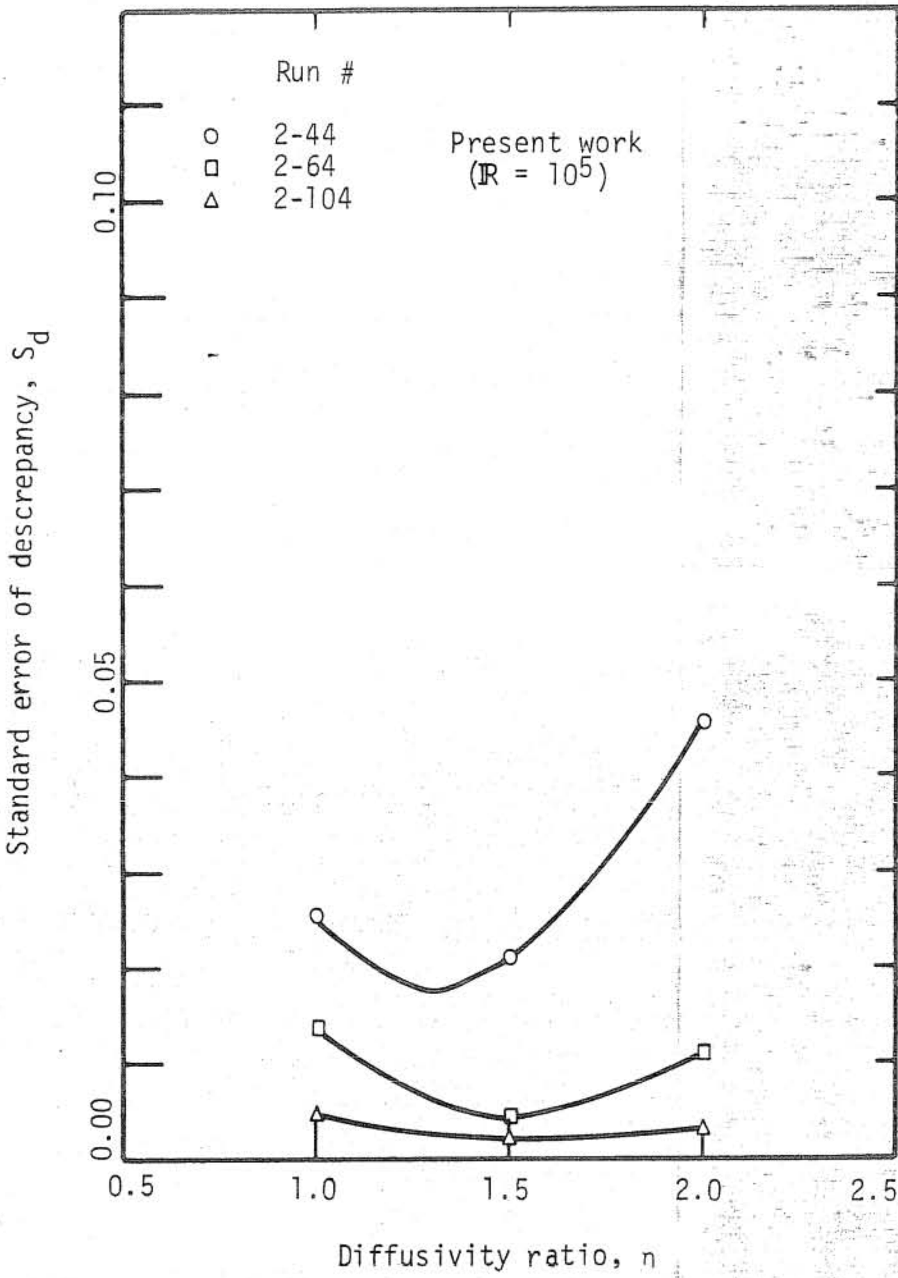

FIGURE 25: Variation of S_d with n

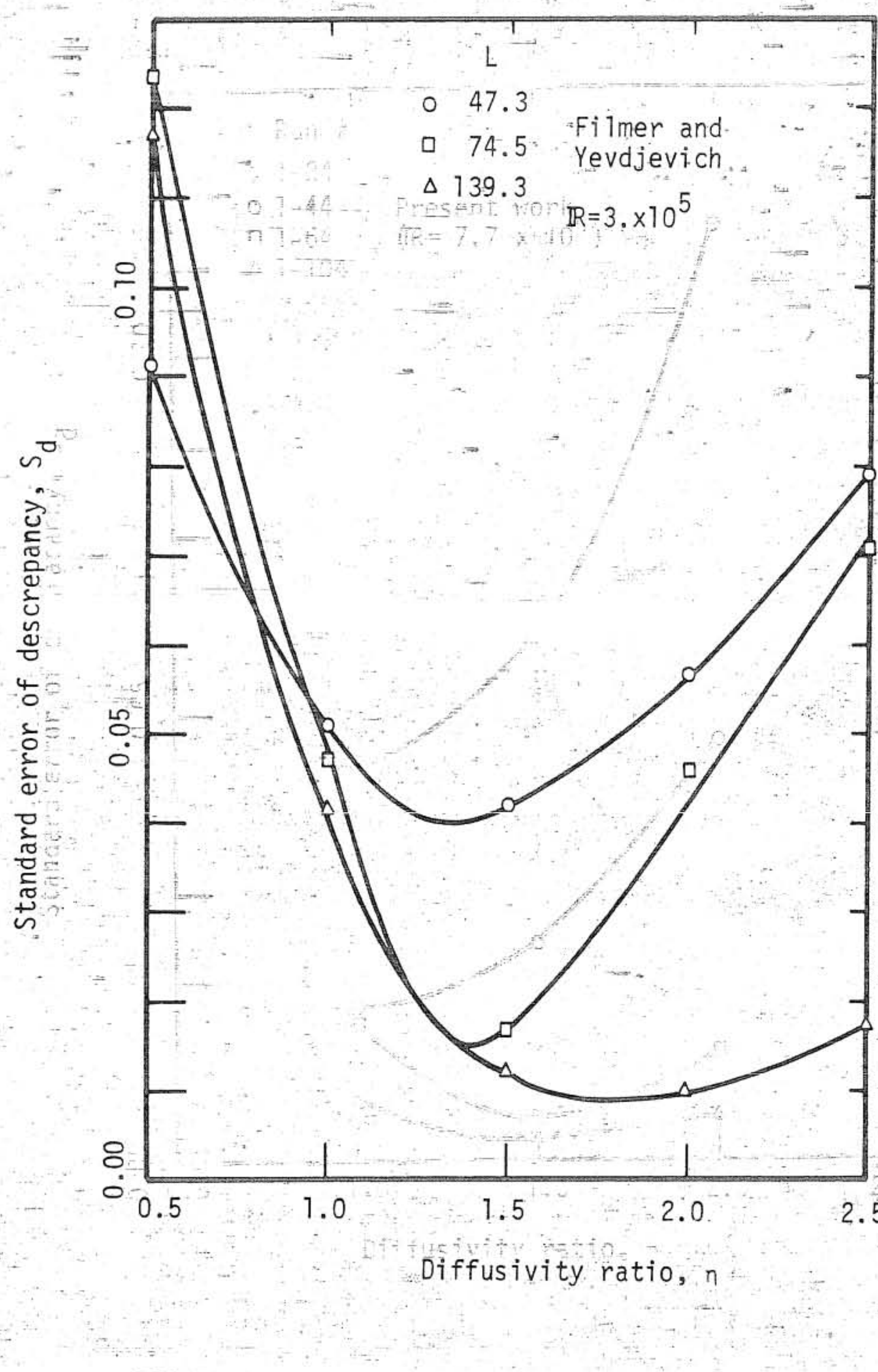

FIGURE 26: Variation of S_d with η

Table 6

Variation of η with L

Reynolds Number	L	η
7.7×10^4	24	0.8
"	44	1.0
"	64	1.5
"	104	1.5
10^5	44	1.3
"	64	1.5
"	104	1.5
3.0×10^5	47.3	1.3
"	74.5	1.4
"	139.3	1.7

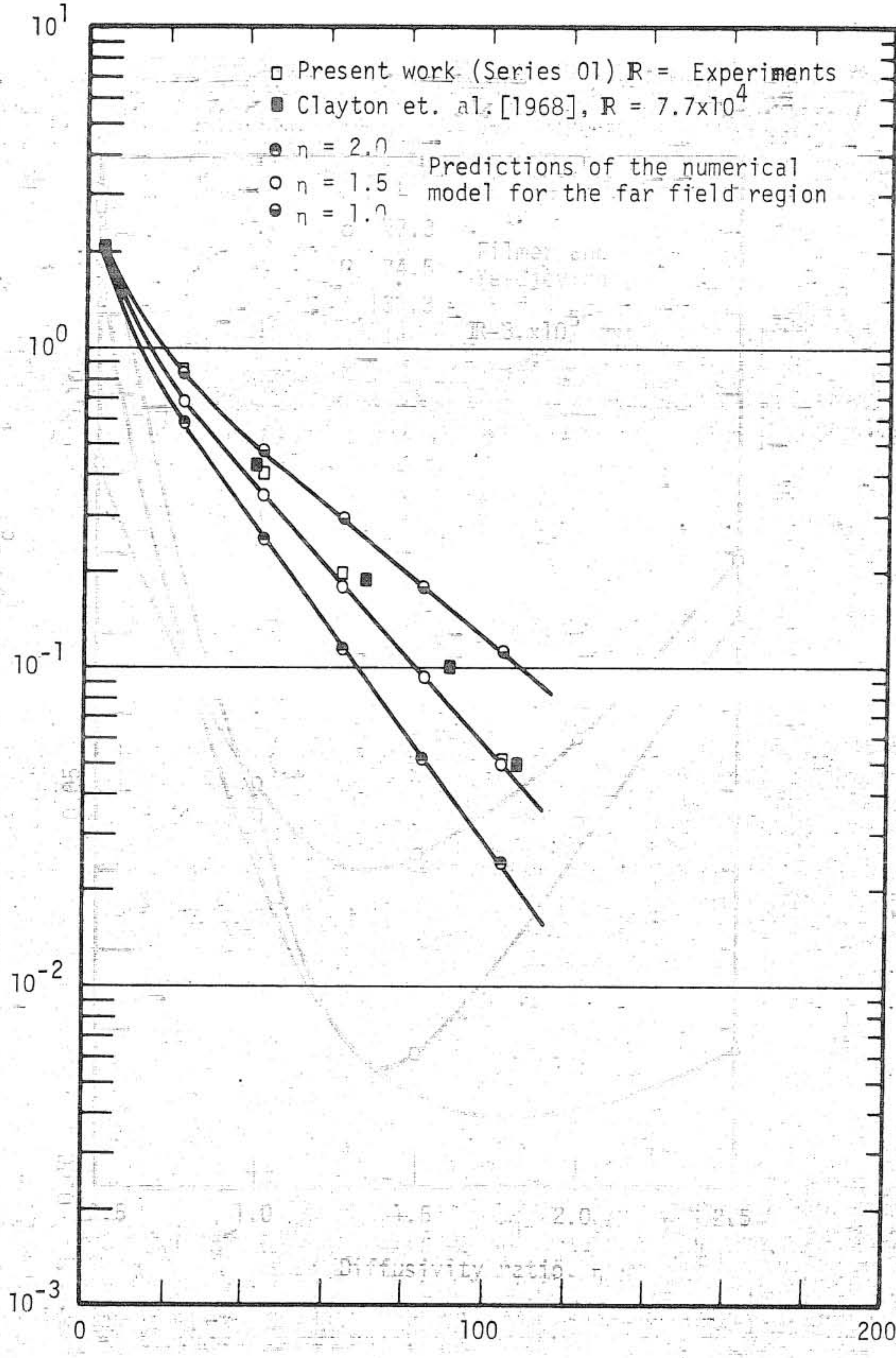

FIGURE 27: Dependence of predicted mixing on η

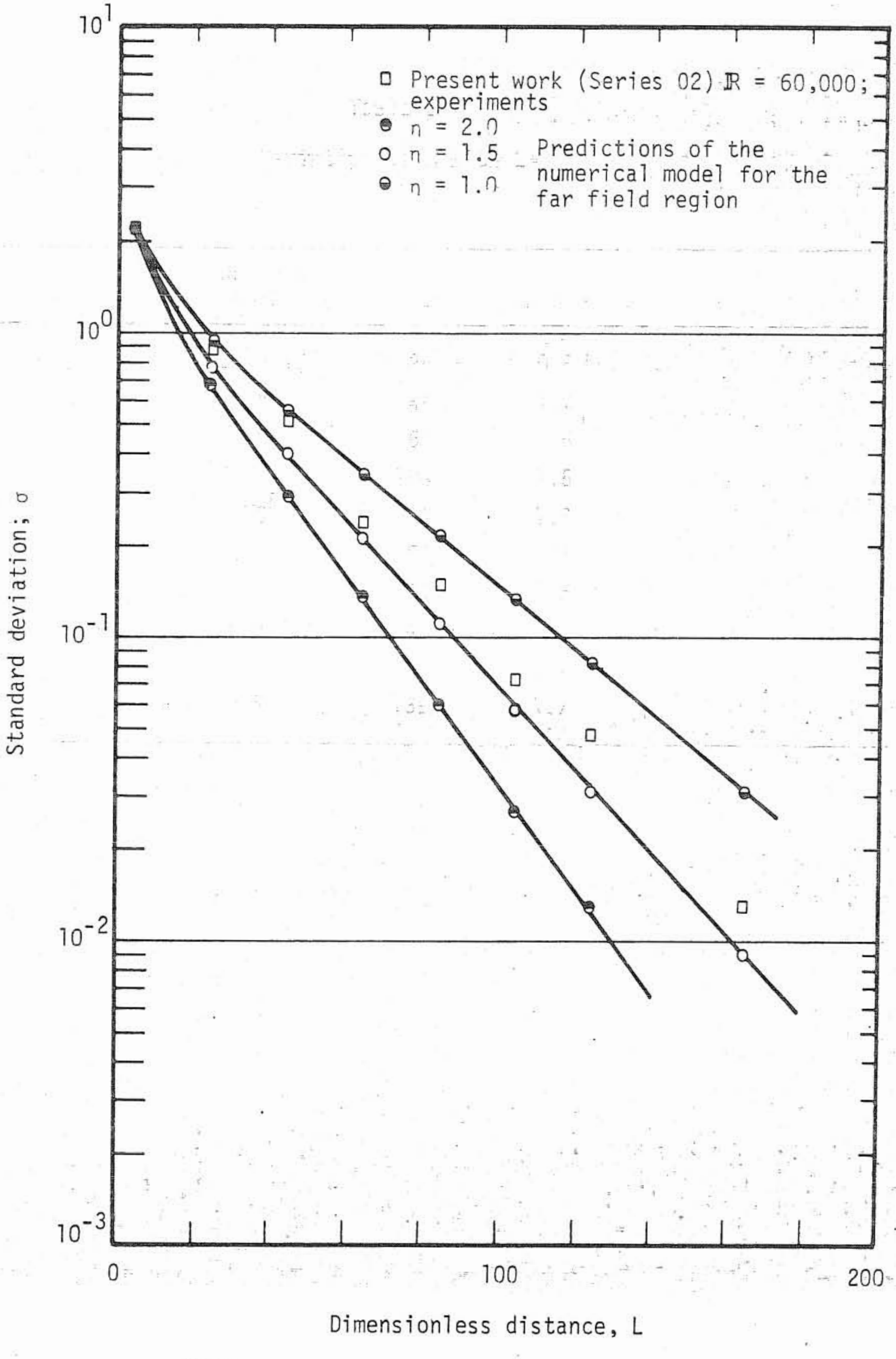

FIGURE 28: Dependence of predicted mixing on η

5.4 Jet Injection

5.4.1 Presentation of Experimental Results

Concentration distributions from several representative runs are presented in Figs. 29 to 45. All data is available in tabular form in a supplementary publication [Ger and Holley, 1974]. The results are in the form of normalized concentration contours. The normalization was with respect to the average concentration for each measurement station. The location of points where tracer concentrations were measured is shown to scale in each figure. Injections were made at the top of the pipe. The injection conditions for each run are given in Table 5 in Section 4.3.1.

5.4.1.1 Effect of σ

In Figs. 29 through 33, the development of mixing is demonstrated for one series of experimental runs (series 06; Table 5).

As defined earlier, the standard deviation, σ (Eq. 4-10), of a concentration distribution is a measure of the mixing; smaller values of σ indicate more complete mixing in a given cross section. Thus, for a given injection condition, longer mixing distances are required in order to achieve smaller σ values. This is demonstrated in Figs. 22 and 23 for a simple source. The same behavior can be seen in Figs. 49, 50, and 51 for jet injections, as discussed later. Theoretically, the ultimate σ value of zero corresponding to a complete mixing requires an

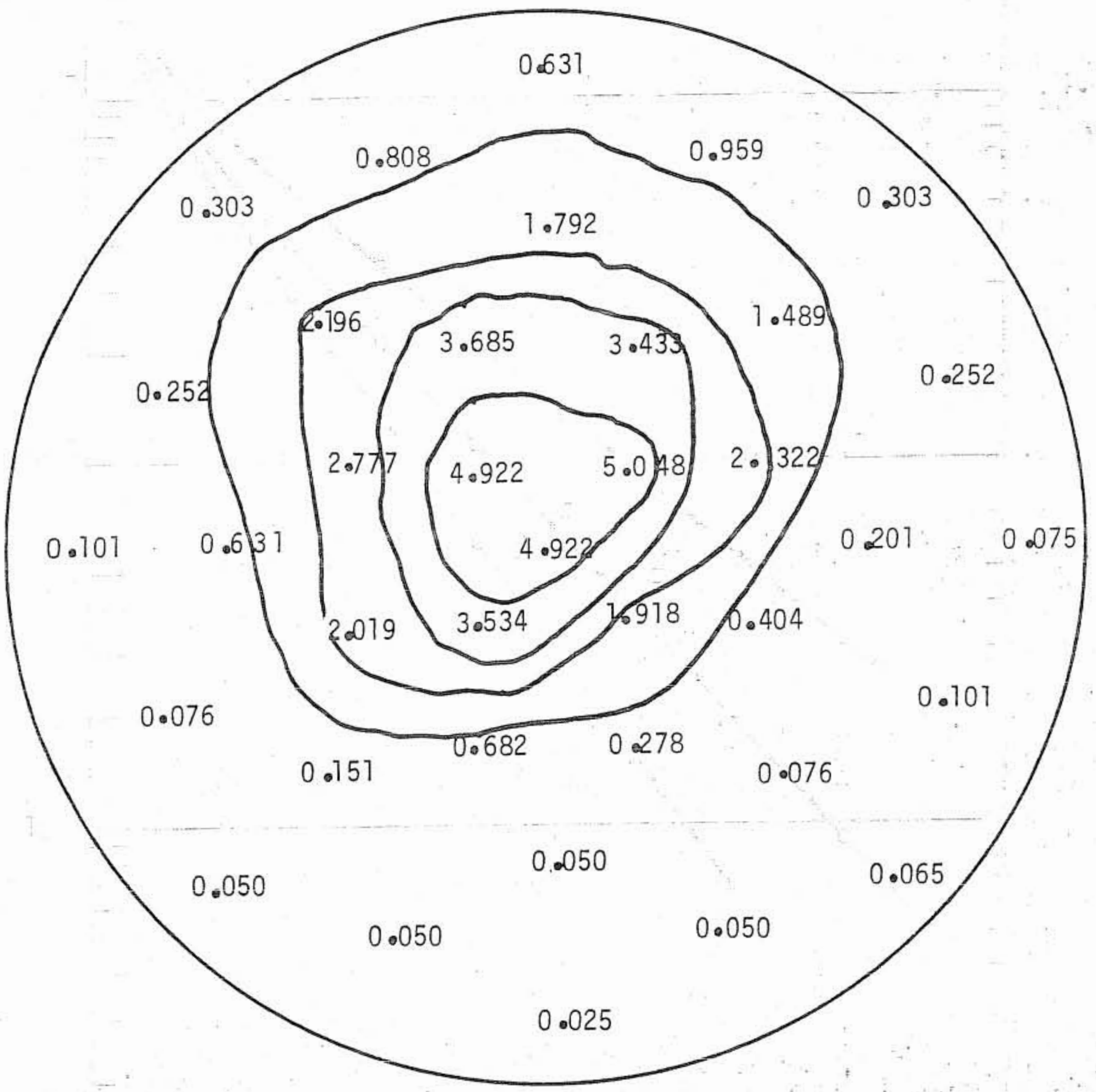

FIGURE 29: Measured concentration distribution for run # 06-004

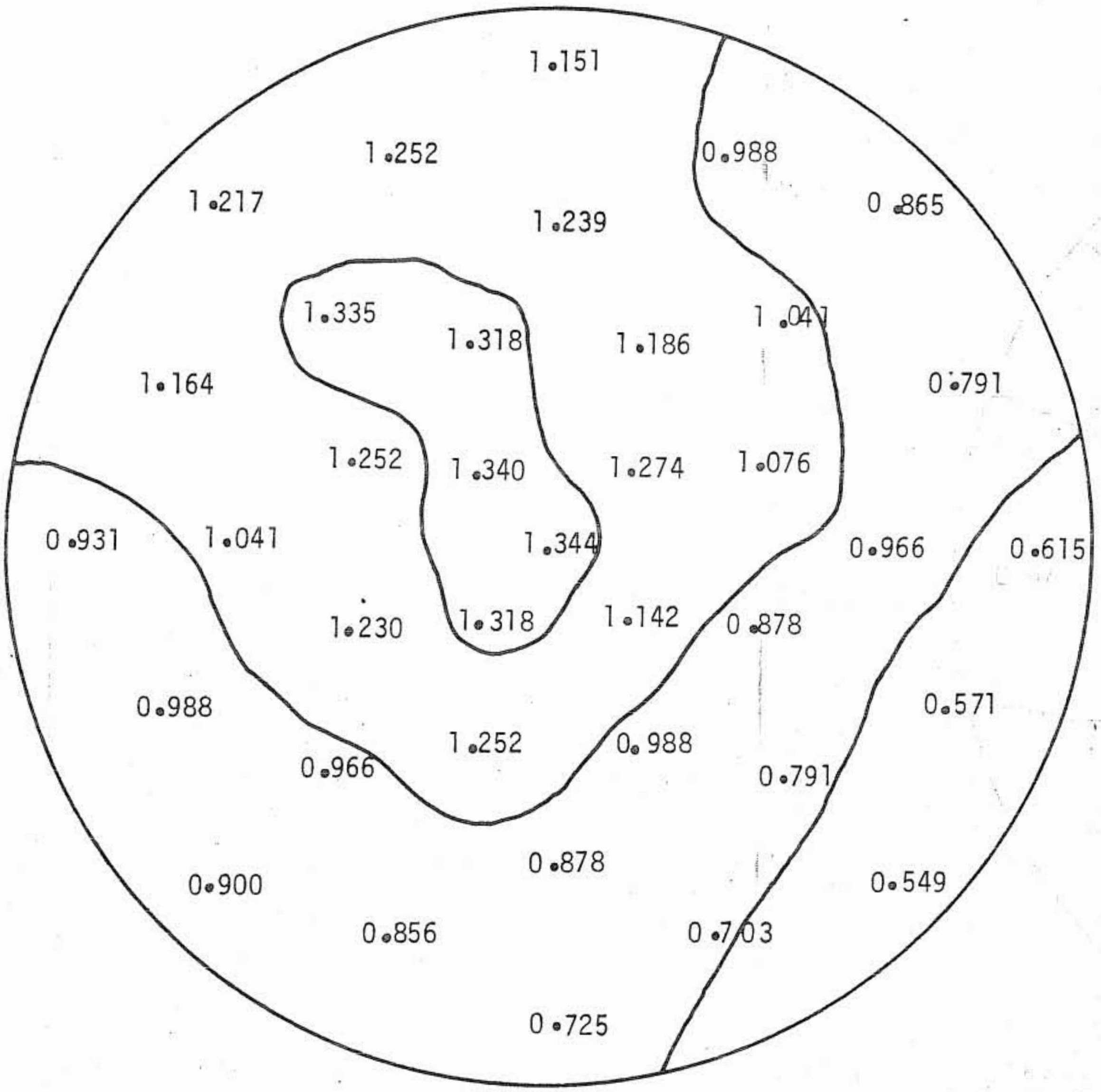

FIGURE 30: Measured concentration distribution for run # 06-024

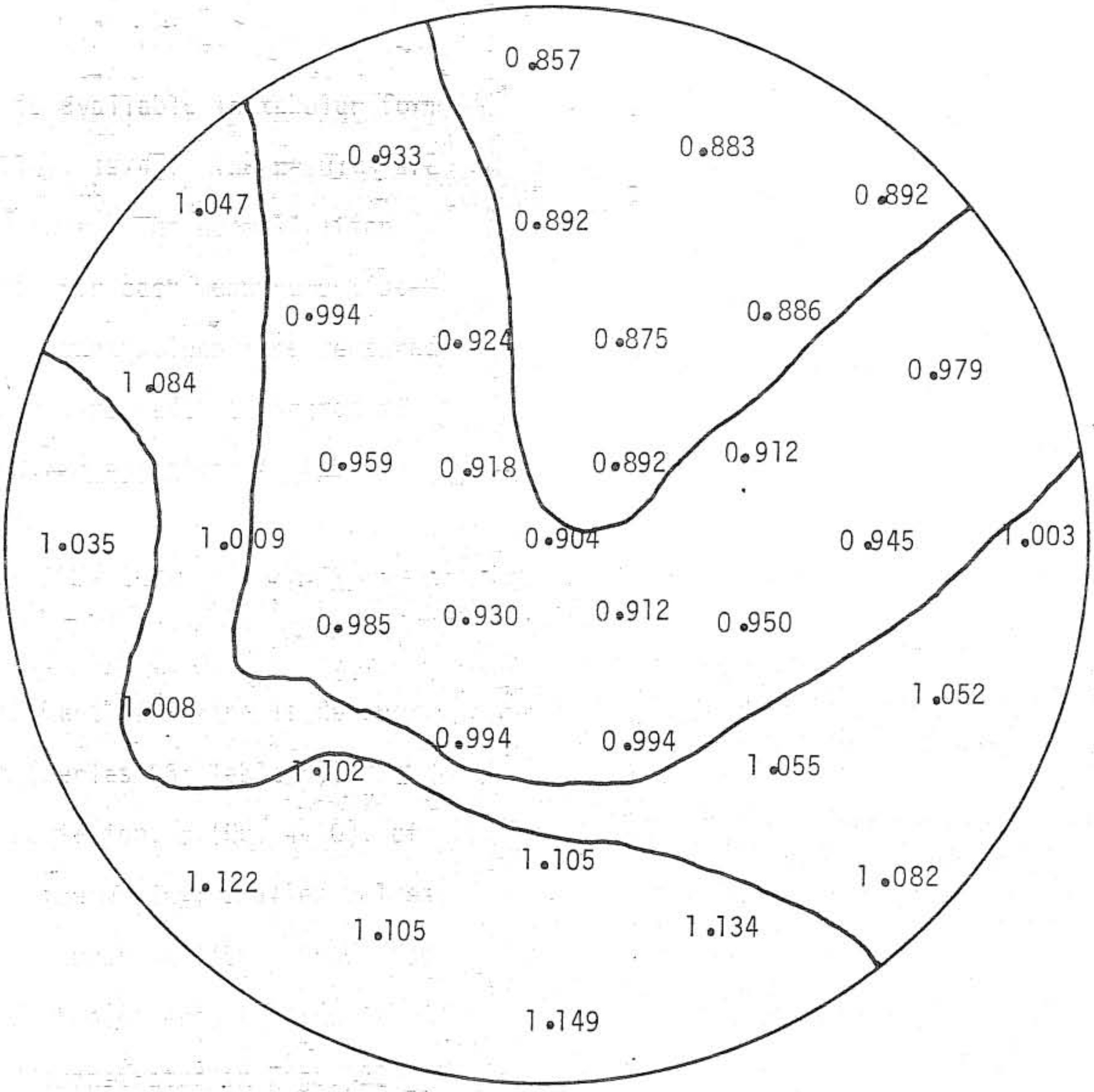

FIGURE 31: Measured concentration distribution for run # 06-044

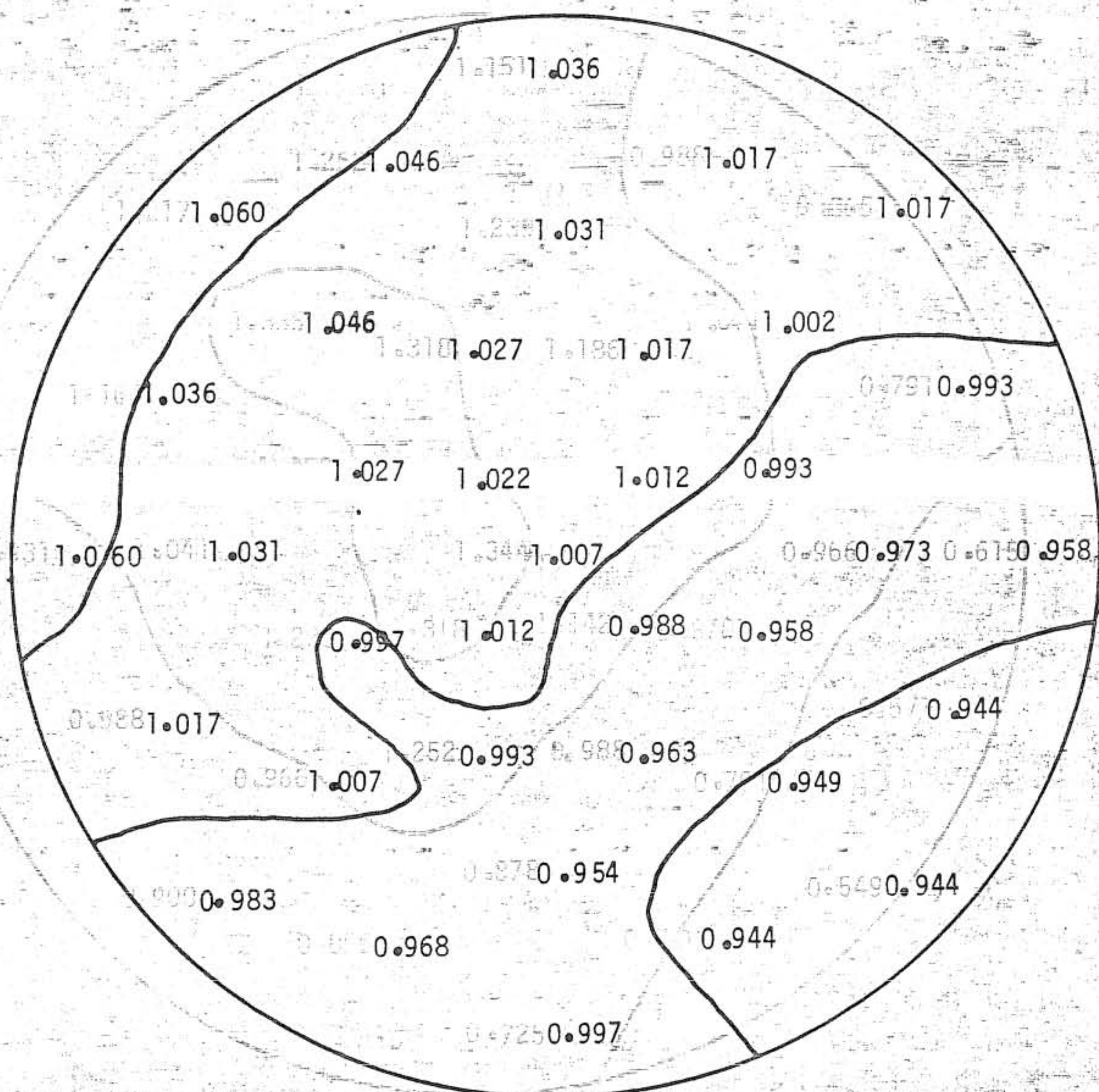

FIGURE 32: Measured concentration distribution for run # 06-084

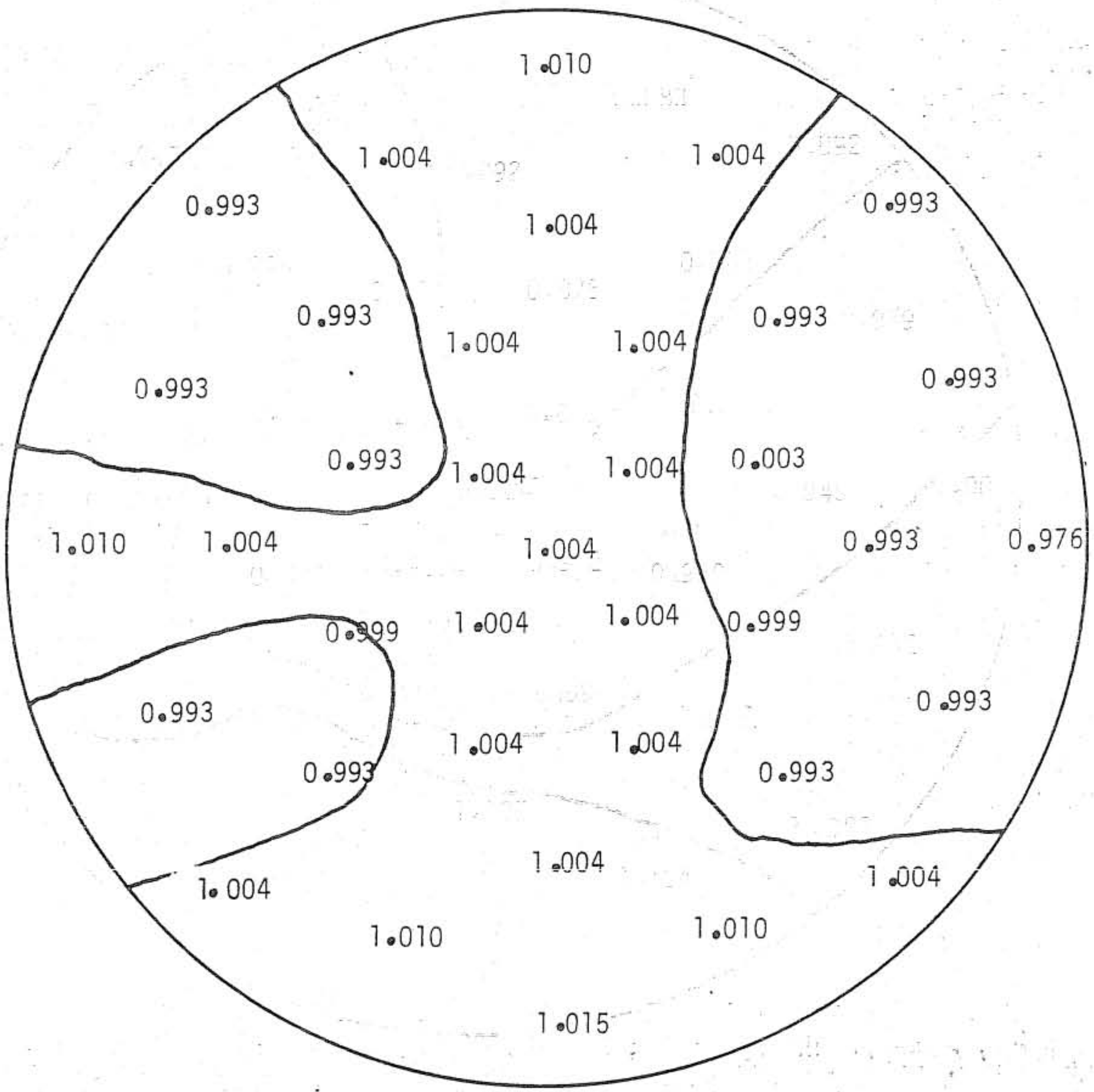

FIGURE 33: Measured concentration distribution for run # 06-124

infinitely long pipe. However, in practice, the smallest value of σ which can be attained is controlled by the magnitude of the experimental error.

5.4.1.2 Effect of k

For a given ratio D_r of the pipe diameter to the injection hole diameter, an increase in the jet-to-pipe velocity ratio k implies an increase in the momentum flux associated with the jet relative to the momentum flux associated with the pipe flow. Thus, as k increases, the jet penetrates further into the crossflow. The concentration contours at a distance of four pipe diameters downstream of the injection hole demonstrate the effect of k on the penetration of the jet into the crossflow. In Figs. 34, 35, 36, and 37 this is shown for four k values for $D_r = 96$. In Fig. 34 (k = 4), the jet penetration is so small that the jet is barely transported away from the top of the pipe. However, as k increased to 8 (Fig. 35), to 12 (Fig. 36), and further to 16 (Fig. 37), the jet was transported further and further away from the top of the pipe.

The position of the jet at the end of the near field region influences the concentration distributions in the far field region. This is demonstrated in Figs. 38 to 41. For a small k value of 4, the jet penetration is small and the maximum concentration stays close to the top of the pipe along the pipe length (Figs. 38 for L = 24 and 39 for L = 84). However, for a larger k value, the jet overpenetrates (i.e., jet penetration is greater than the optimum) and the maximum concentration

FIGURE 34: Measured concentration distribution for run # 04-004

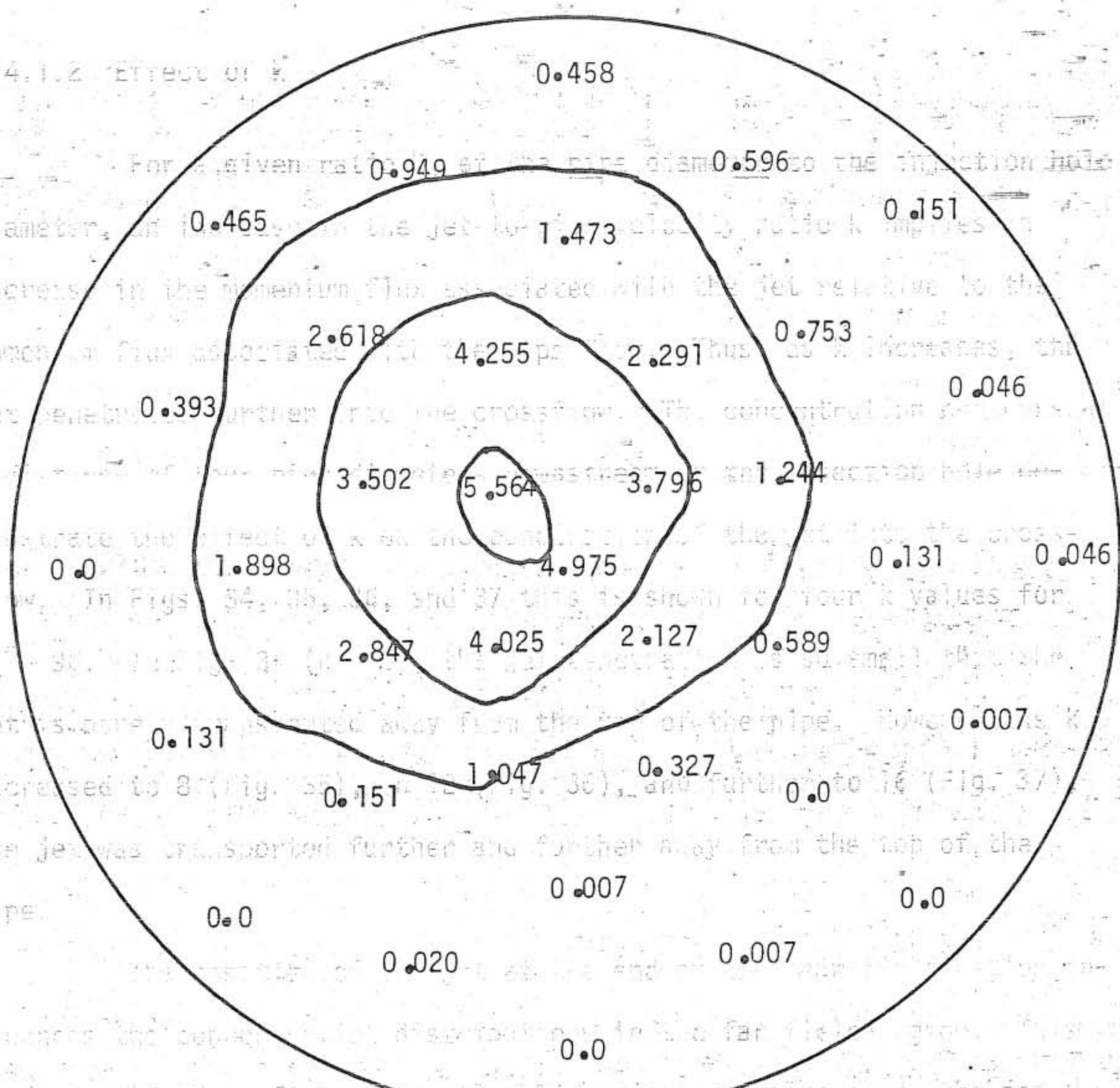

FIGURE 35: Measured concentration distribution for run# 05-004

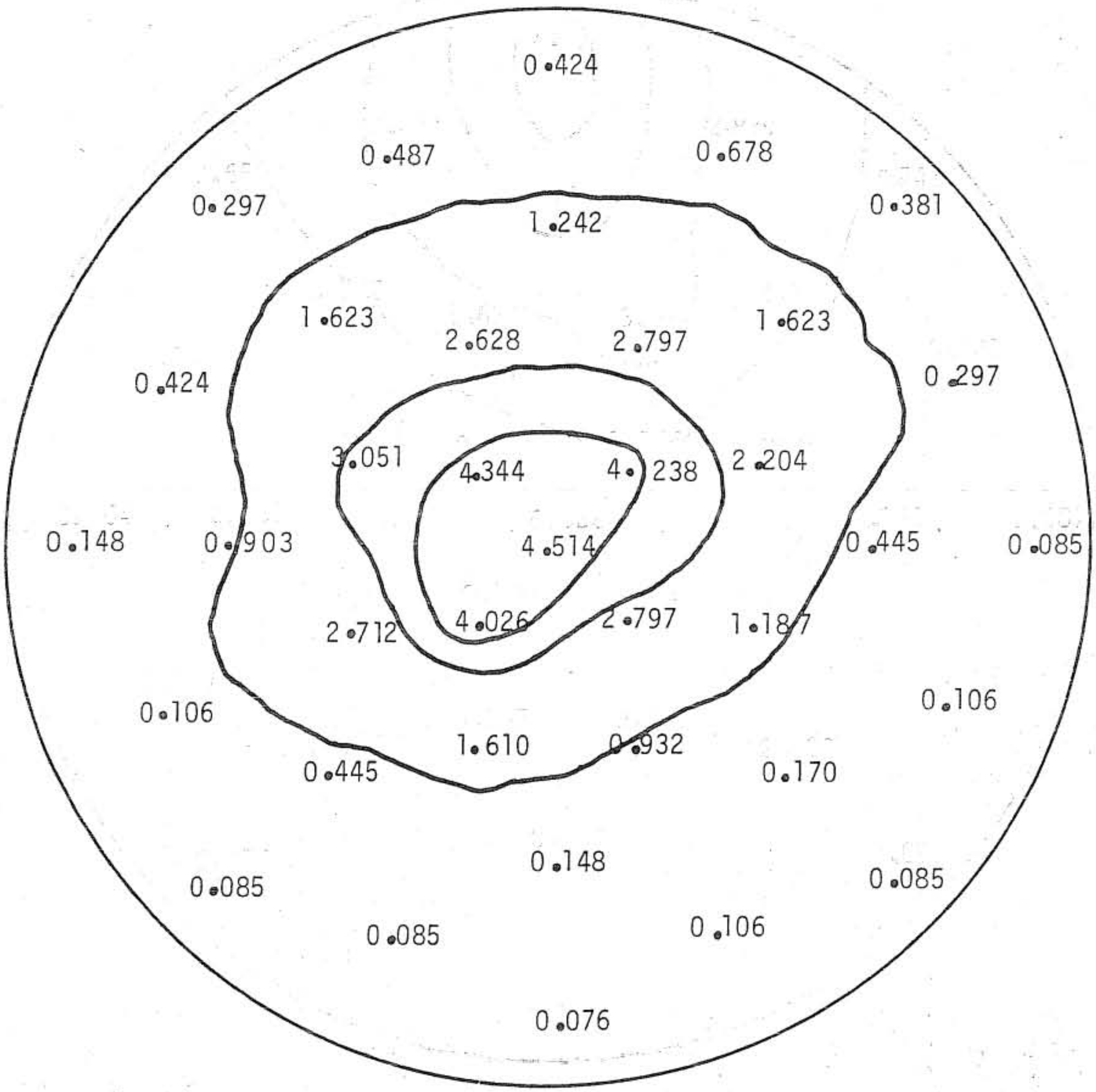

FIGURE 36: Measured concentration distribution for run # 07-004

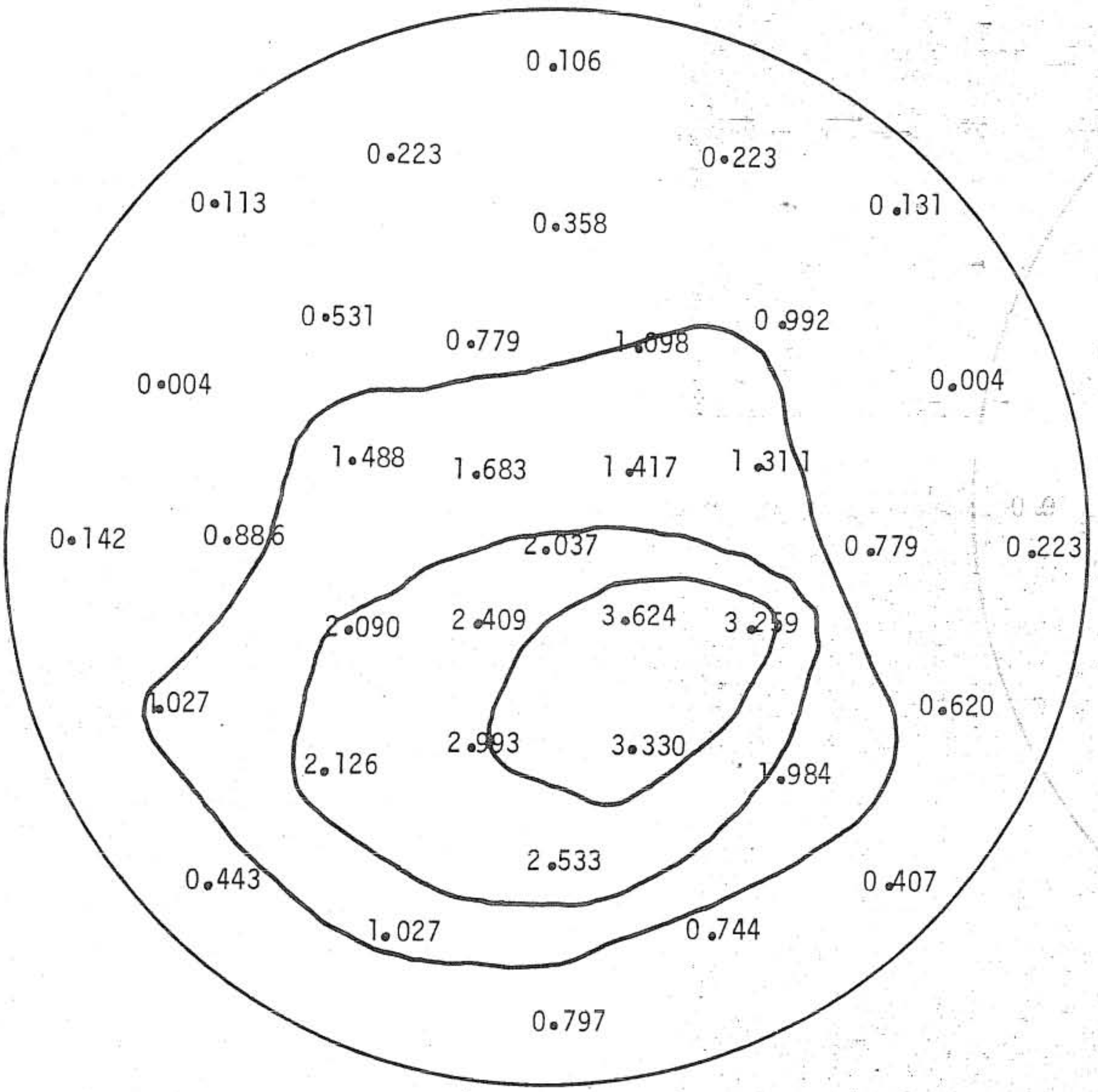

FIGURE 37: Measured concentration distribution for run # 08-004

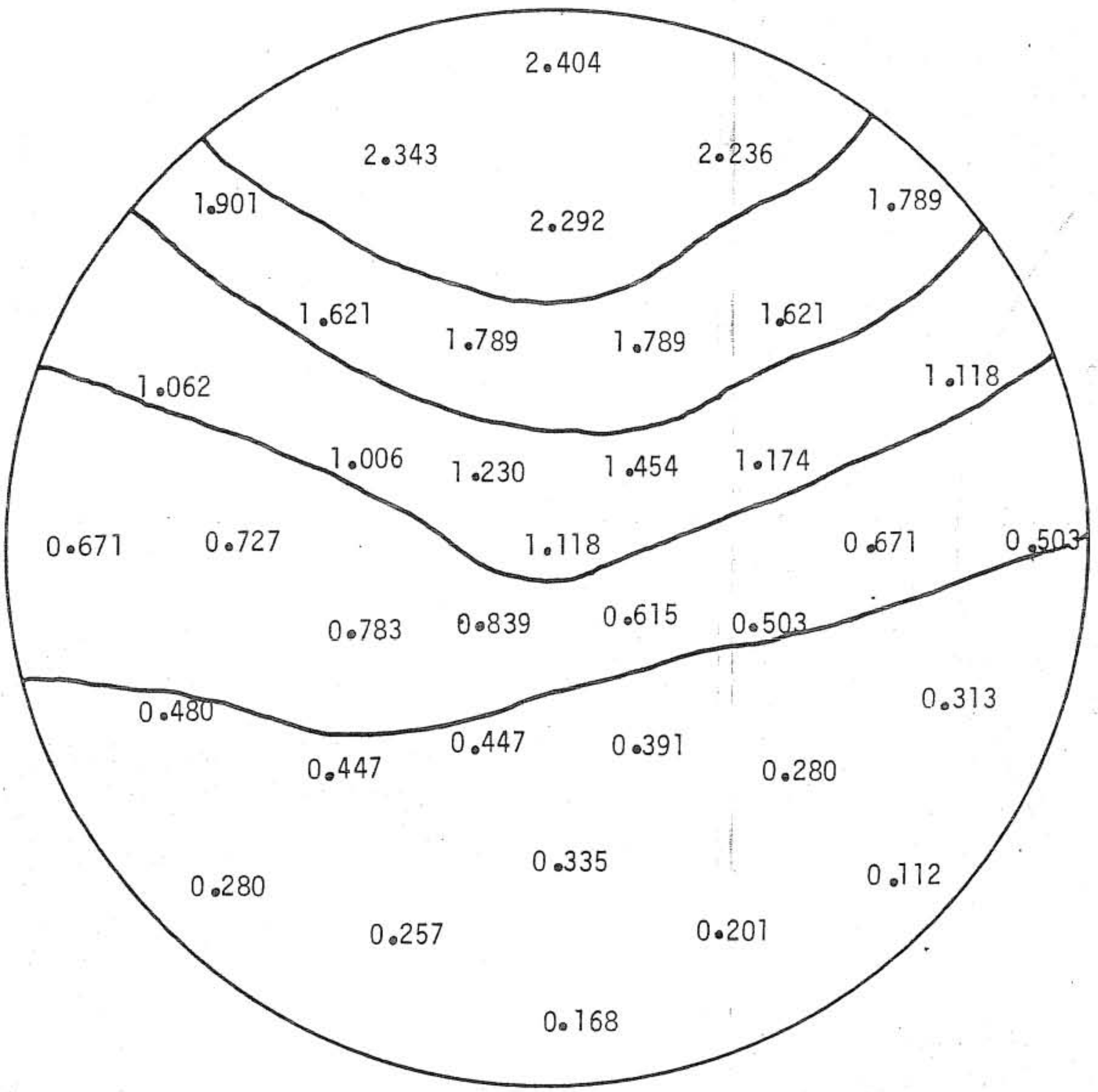

FIGURE 38: Measured concentration distribution for run # 04-024

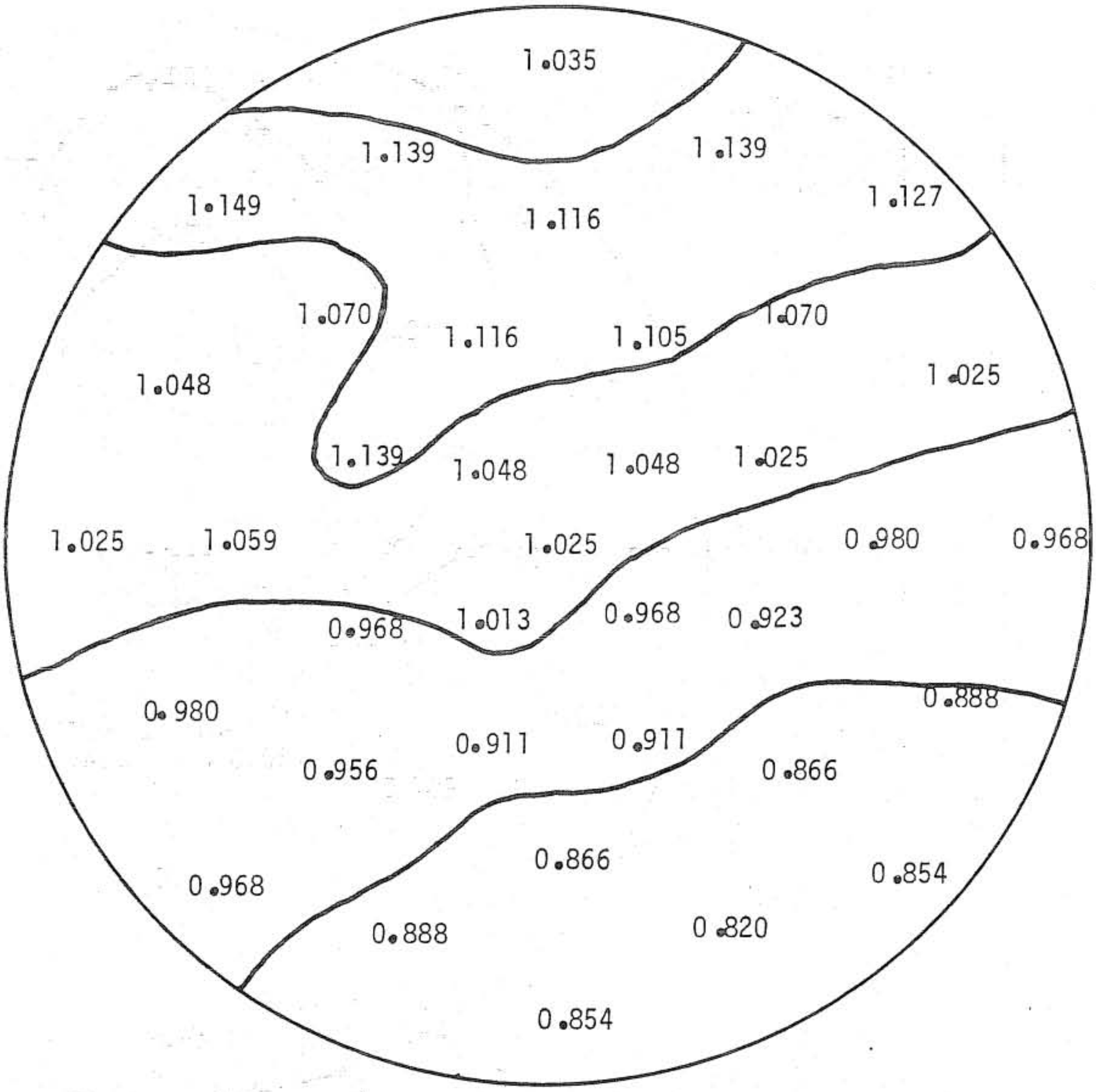

FIGURE 39: Measured concentration distribution for run # 04-084

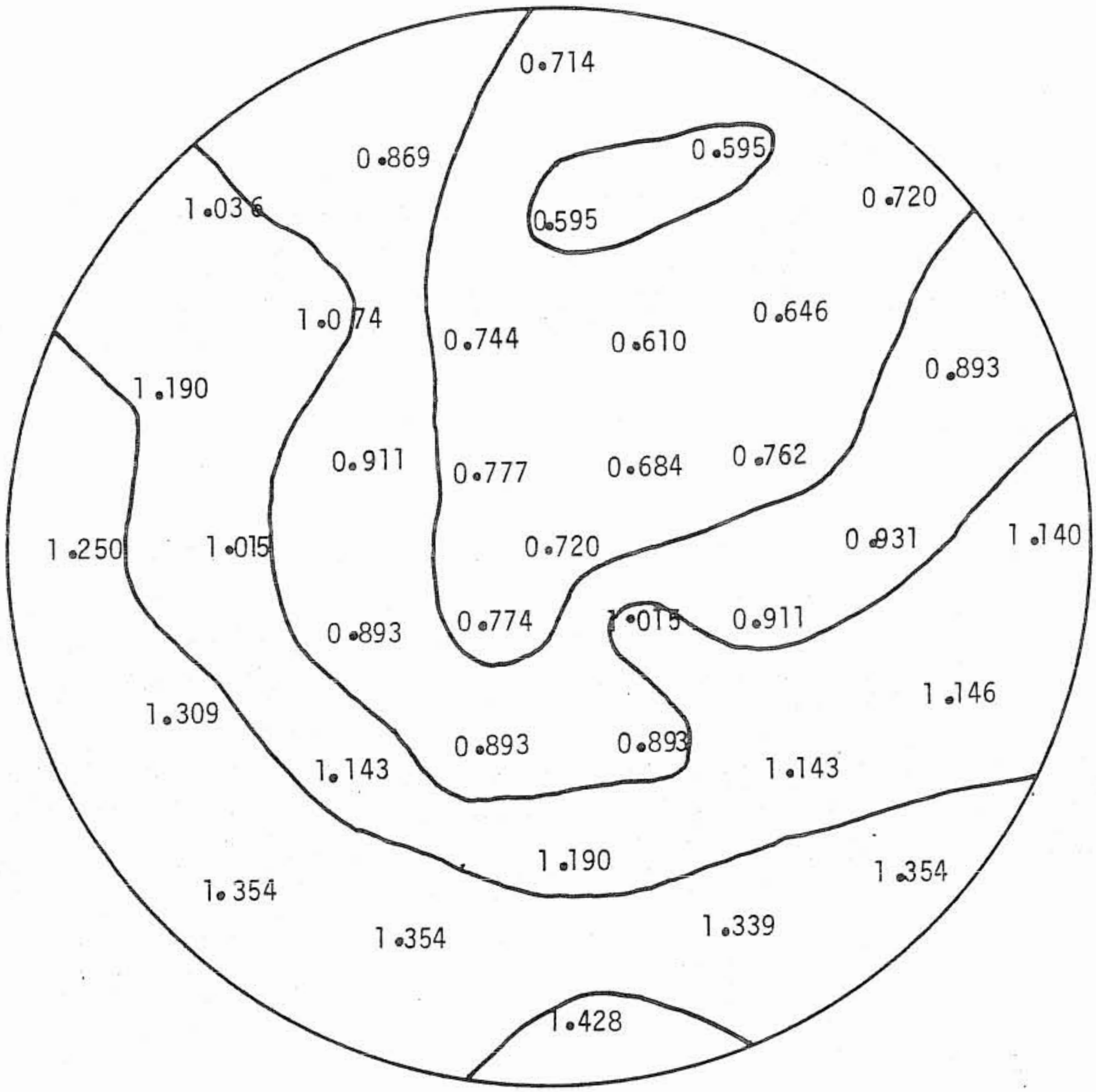

FIGURE 40: Measured concentration distribution for run # 08-024

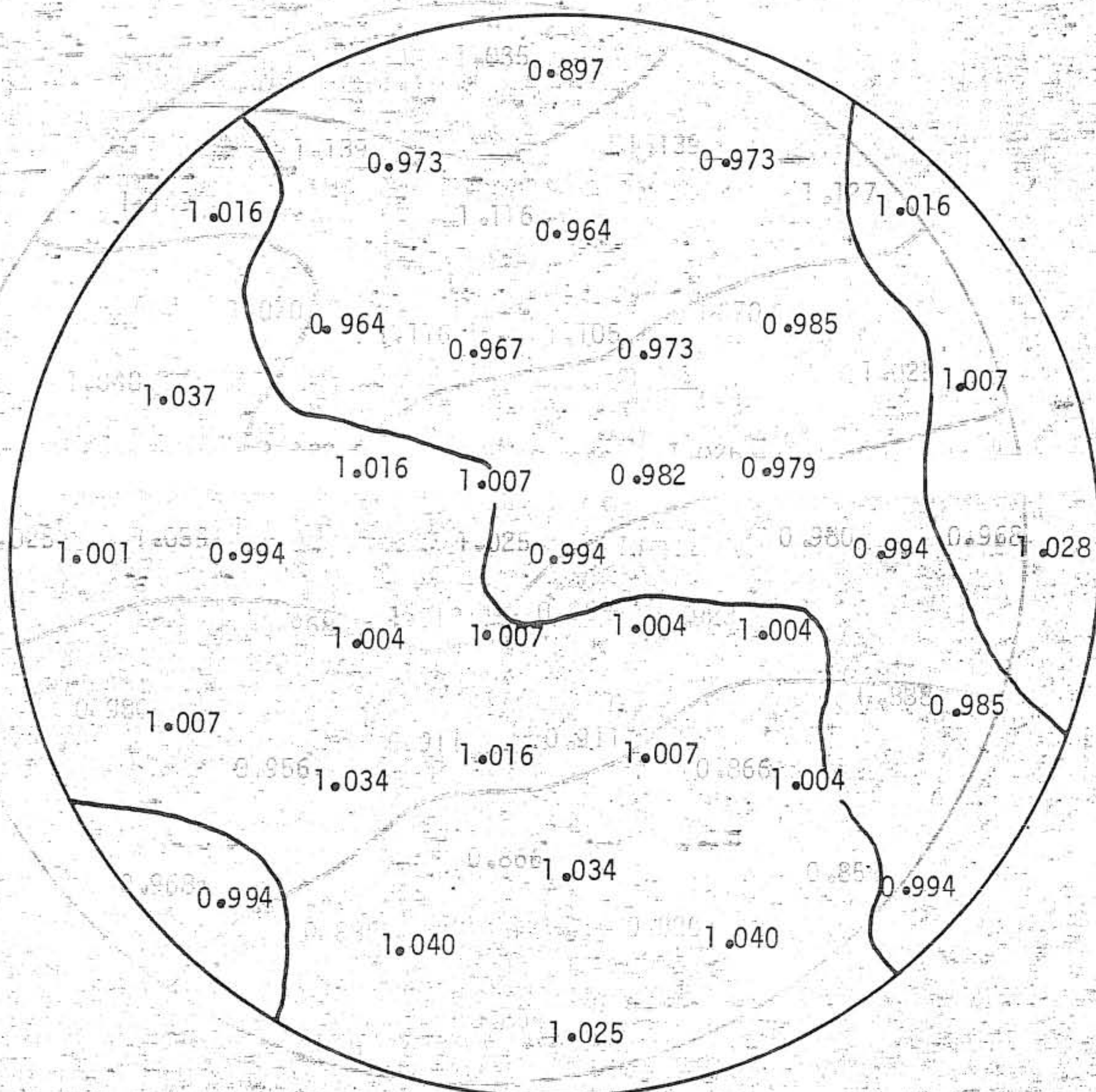

FIGURE 41: Measured concentration distribution
for run # 08-084

Table 7

Variation of σ with k at a Given L Values for D_r = 96

L \ K	4	8	10	12	16
24	1.81	1.45	1.45	1.21	0.94
44	0.75	0.28	0.23	0.18	0.25
64			0.035	0.022	0.061
84	0.10	0.044	0.016	0.012	0.029
124	0.036	0.019	0.009	0.007	0.011
164		0.009	0.006	0.005	0.007

Table 8

Variation of L with k and σ for D_r = 96

		L		
Series	k	σ = 0.01	σ = 0.02	σ = 0.05
04	4	170	144	108
05	8	148	119	80
06	10	108	83	56
07	12	100	70	48
08	16	127	104	70

is located at the bottom of the pipe along the pipe length (Figs. 40 for $L = 24$ and 41 for $L = 84$). For any asymmetrical case where the maximum concentration is not on the pipe centerline the maximum concentration will tend to move toward the pipe boundary as the tracer moves along the pipe. Therefore, it is beneficial to have the jet penetration as near to the centerline as possible in order to minimize this tendency of the boundary to attract the maximum concentration. The influence of the jet penetration (or k for a given D_r) on the concentration distributions is more clearly seen when the standard deviation, σ (Eq. 4-10), of concentration distributions are compared at several given locations along the pipe length for different k values (Table 7). For the larger L values, the standard deviation σ decreases with increasing k until an optimum k value is reached. Further increase in k gives an increase in σ. Since smaller values of σ represent better mixing, the optimum k value for which the σ becomes the smallest corresponds to the shortest mixing distance. In other words, there exists an optimum k value which gives the shortest mixing distance corresponding to a given D_r. This is demonstrated in Table 8, which shows that for $D_r = 96$ the optimum k value is approximately 12.

5.4.1.3 Effect of D_r

For a given k ratio and for a given pipe, a decrease in D_r (i.e., an increase in injection hole diameter) implies an increase in the momentum flux associated with the jet relative to the momentum flux

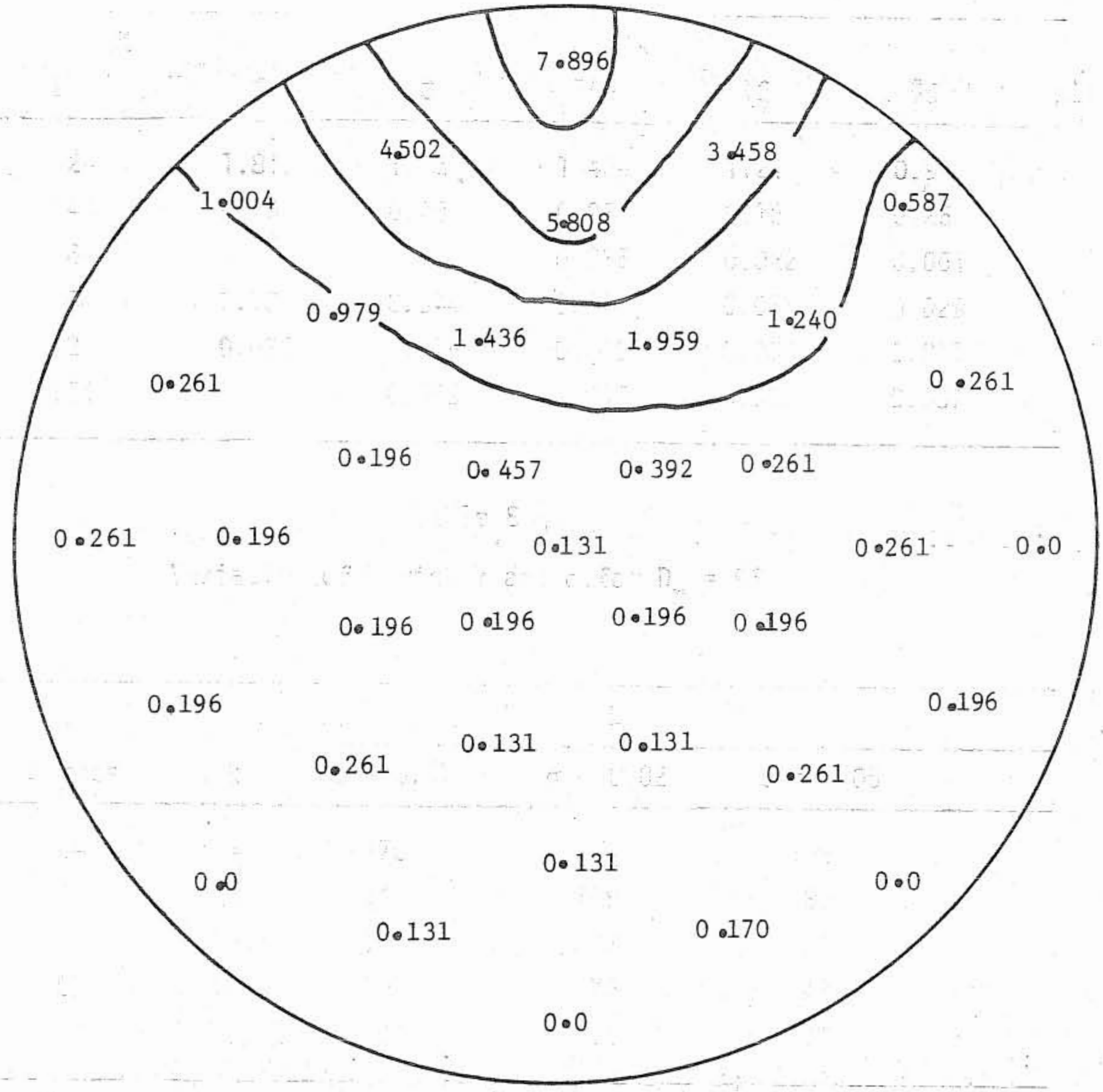

FIGURE 42: Measured concentration distribution for run # 12-004

of the pipe flow. Therefore, the variation in jet penetration and thus in mixing distance when D_r is decreased for a constant k is the same as when k is increased for a constant D_r. The concentration contours at distance of four pipe diameters downstream of the injection port demonstrate the effect of D_r on the jet penetration. This is shown for k = 8 in Fig. 35 (D_r = 96) and Fig. 42 (D_r = 192). In Fig. 42 (D_r = 192), the jet penetration was small; the jet was barely transported away from the top of the pipe. However, when D_r = 96 (Fig. 35) the jet was transported further away from the top of the pipe.

5.4.1.4 Effect of $\mathbb{F}_d$

For a given D_r and k, an increase in density disparity, $\Delta\rho$, naturally implies an increase in the density disparity flux associated with the jet. Thus, as a result of the combined effects of momentum and density disparity fluxes the penetration of the jet will increase as $\Delta\rho$ increases (provided, of course, that the jet is oriented so that the density disparity flux adds to the momentum flux). The relative increase in the penetration of the jet due to additional effect of density disparity flux is dependent on the relative magnitudes of the momentum and density disparity fluxes of the jet. The densimetric Froude number ($\mathbb{F}_d$, Eq. 4-6) is representative of the ratio of the momentum and density disparity fluxes. As $\mathbb{F}_d$ increases, the relative significance of the density disparity on the penetration of the jet decreases. The concentration contours shown in Figs. 43, 44, and 45

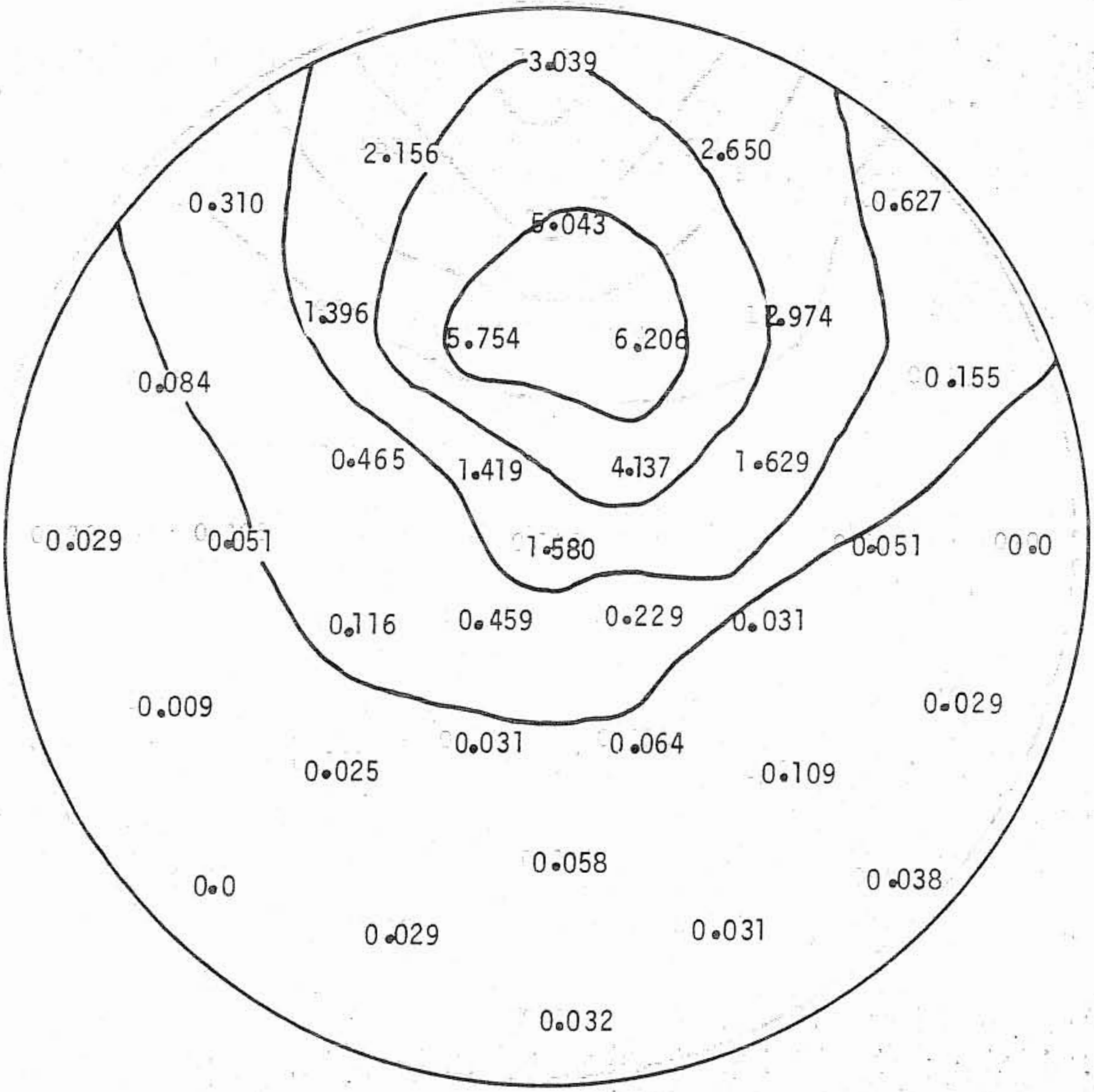

FIGURE 43: Measured concentration distribution for run # 09-004

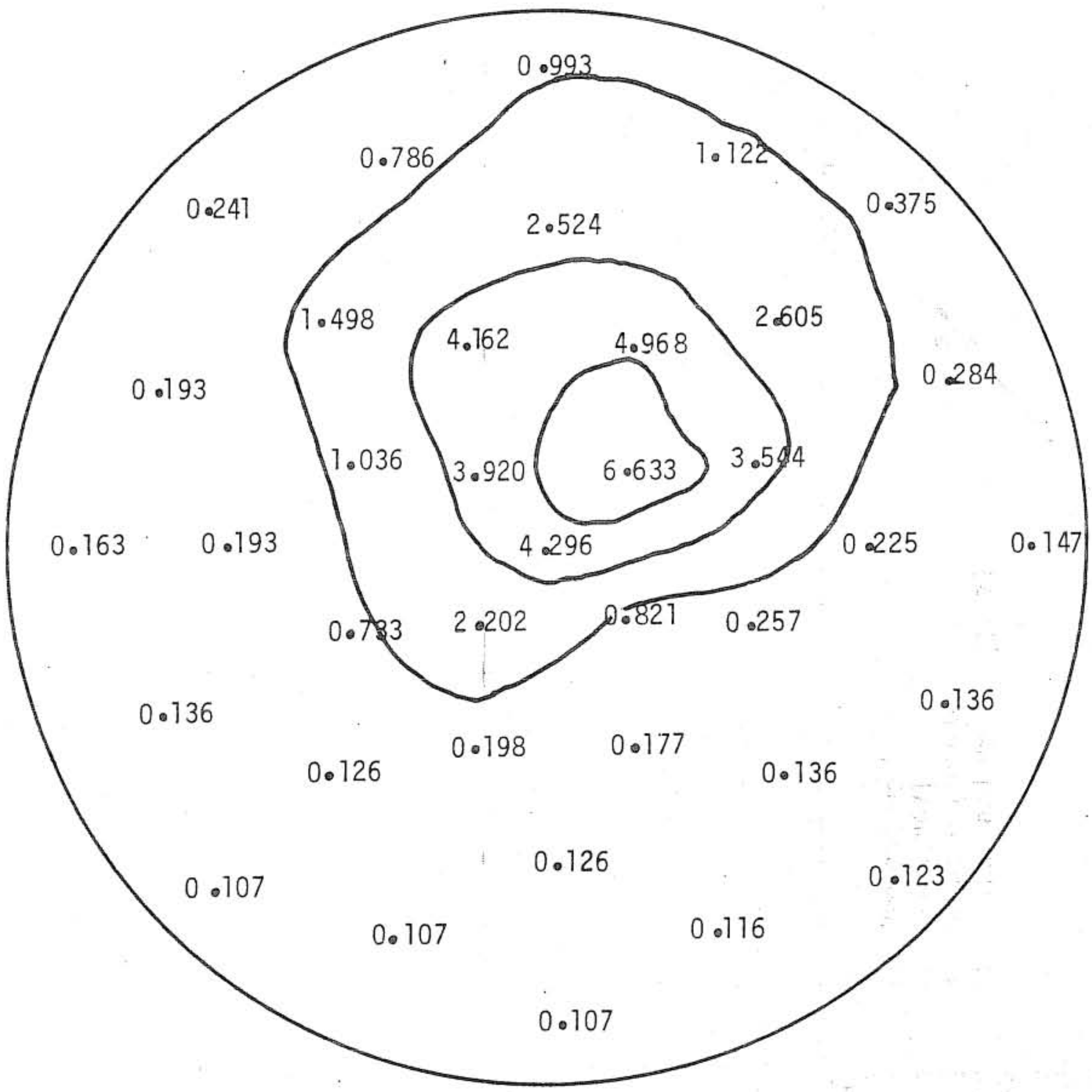

FIGURE 44: Measured concentration distribution for run # 10-004

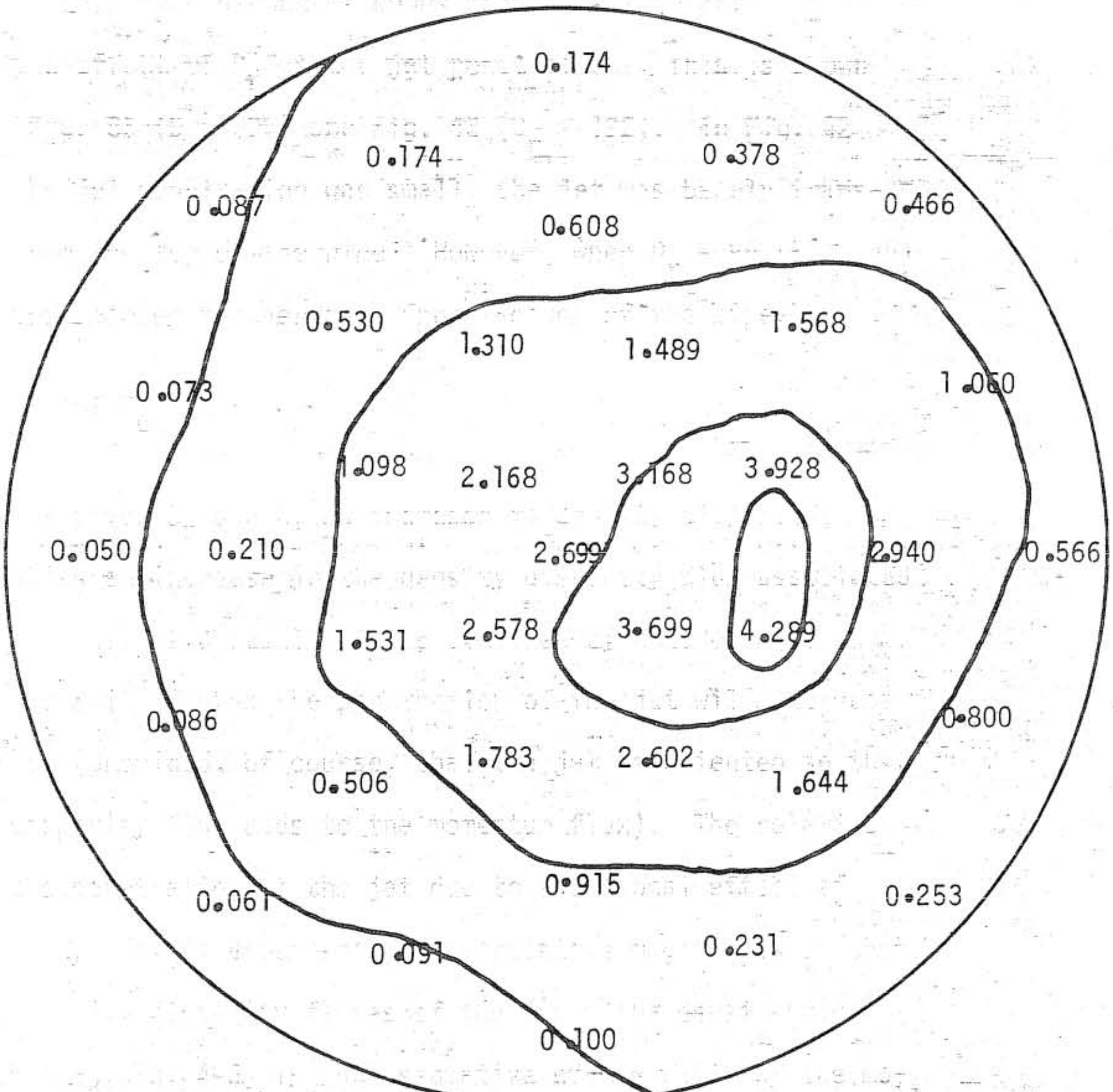

FIGURE 45: Measured concentration distribution for run # 11-004

demonstrate this kind of dependence of penetration on $\mathbb{F}_d$. For a buoyant jet having a $\mathbb{F}_d$ of 26 (Fig. 43) the maximum concentration is transported further away from the top of the pipe than for a nonbuoyant jet with the same k (Fig. 34). For larger densimetric Froude numbers ($\mathbb{F}_d$ = 52 (Fig. 44) and $\mathbb{F}_d$ = 104 (Fig. 45)) no appreciable increase in penetration was observed as compared to nonbuoyant jets with the same k (Figs. 35 and 37). Table 9 gives a quantitative comparison of the jet penetration for various situations. From this table, it was concluded that the penetration of the jet is independent of the buoyancy effects when $\mathbb{F}_d$ is larger than about 50. As can be seen from the conditions investigated (Table 5), there were not enough values of $\mathbb{F}_d$ investigated to give an exact definition of the critical $\mathbb{F}_d$. Therefore, $\mathbb{F}_d$ = 50 will be used as an order of magnitude indication for the critical $\mathbb{F}_d$. This would mean that the mixing distance is also independent of the initial density disparity for densimetric Froude numbers larger than 50. The experimentally observed variations of σ with L for buoyant jets and some comparable nonbuoyant jets are shown in Fig. 46. The average variation in mixing distance between the buoyant and nonbuoyant cases is more than 10 percent for a densimetric Froude number of 26 (Table 10). However, for densimetric Froude numbers larger than 50 the variation becomes insignificant (Table 10).

5.4.2 Numerical Work

In the case of a jet injected perpendicularly into a crossing pipe flow, an explicit analytical solution is impossible to obtain

Table 9

Variation of Jet Penetration with $\mathbb{F}_d$ and k for D_r = 96

$\mathbb{F}_d$	k	J_p[1]	$(J_p)_N/(J_p)_B$[2]
26 ∞	4	0.33 0.05	15%
52 ∞	8	0.42 0.42	100%
104 ∞	16	0.57 0.57	100%

[1]J_p jet penetration in pipe diameters

[2]N refers to a nonbuoyant jet ($\mathbb{F}_d = \infty$) and B refers to a buoyant jet ($\mathbb{F}_d < \infty$).

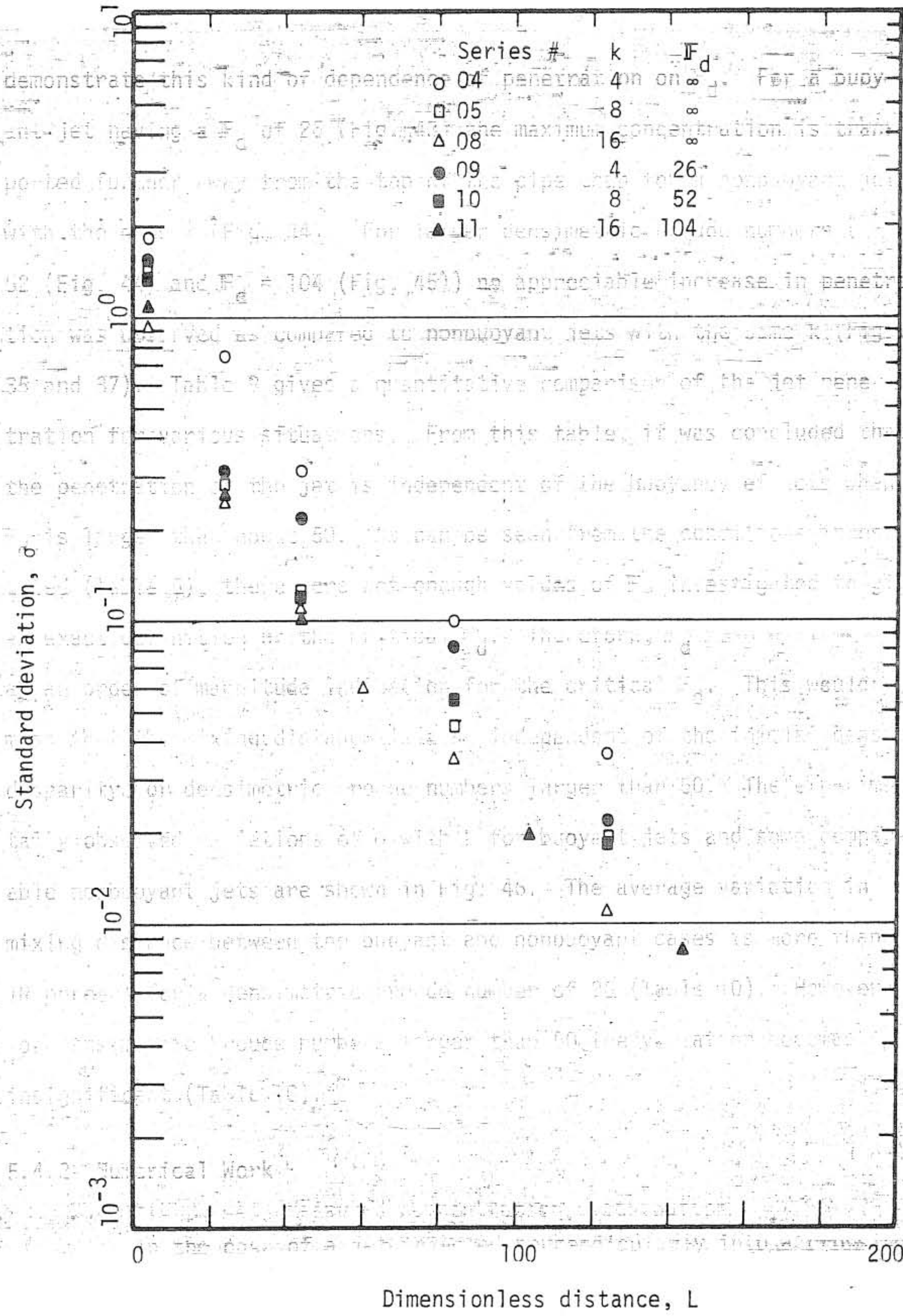

FIGURE 46: Effect of $\mathbb{F}_d$ on mixing

Table 10

Variation of L with $\mathbb{F}_d$, k, and σ for $D_r = 96$

k	σ	$\mathbb{F}_d$	L	$L_N - L_B/L_N$ [2]	Average Deviation in L
4	0.02	26 ∞	128 146[1]	12.3%	13.6%
	0.05	26 ∞	98 111	11.7%	
	0.10	26 ∞	70 84	16.7%	
8	0.02	52 ∞	122 123	0.8%	0.6%
	0.05	52 ∞	82 80	- 2.5%	
	0.10	52 ∞	52 52	0.0%	
16	0.02	104 ∞	103 103	0.0%	0.0%
	0.05	104 ∞	70 70	0.0%	
	0.10	104 ∞	47 47	0.0%	

[1]Extrapolated

[2]Subscripts N and B refers to nonbuoyant ($\mathbb{F}_d = \infty$) and buoyant ($\mathbb{F}_d < \infty$) jets, respectively.

(Chapter 3). Thus, a mathematical model, using a numerical integration scheme was developed to describe the behavior of the jet as discussed in Chapter 3. However, in addition to the geometric and dynamic characteristics of the jet and the pipe flow at the injection point, the model needs three empirical coefficients: α and C_D in the near field region, and η in the far field region. In Section 5.3.2, evaluation of η was presented. Evaluation of α and C_D is provided in Section 5.4.3, below.

For known α, C_D, and η, the mixing for a jet of known characteristics can be predicted by the model. The predictions of the model for several situations are provided in Section 5.5.4 (Figs. 49, 50, and 51), below, where the numerical predictions are compared with the experimental results.

5.4.3 Determination of α and C_D

The entrainment coefficient α (Eq. 2-5) and the drag coefficient C_D (Eq. 2-7) were determined by matching the theoretical and experimental results for the normalized concentration distributions at the first measurement station which was four pipe diameters downstream of the injection port. An independent evaluation of α and C_D was not possible. A two-step procedure as described below was used to evaluate α and C_D. In the first step, influence coefficient algorithm [Becker and Yeh, 1972] was employed to determine the α and C_D pair which yields the minimum standard error of discrepancy between the numerical and experimental concentration distributions. In the evaluation process, occasionally certain α and C_D values corresponding to the smallest error would produce numerically calculated concentration distributions which were obviously not in good agreement with the measurements. Therefore, in evaluating α and C_D, the subjective constraint was placed that the experimentally and numerically obtained jet centerline locations had to be in good agreement for the selected α and C_D pair. Thus, in the second step, a manually controlled trial and error process was used to obtain the best pair of α and C_D values in the neighborhood of the α and C_D pair determined in the first step of the evaluation process. Because the experiments were not designed for the determination of α and C_D and because of the subjectivity of obtaining the best α and C_D pair, the accuracy of this procedure is probably at most two significant digits for α and C_D.

The values of coefficient of entrainment, α, and drag coefficient, C_D, were obtained for several injection conditions. A direct comparison of these values with α and C_D values from past work is not possible since different definitions of these coefficients were employed by different investigators. However, some of the available data from the literature could be used to calculate α and C_D values in accordance with the technique of matching described above. The values of α and C_D thus obtained are summarized in Figs. 47 and 48, respectively. The entrainment coefficient α and drag coefficient C_D were both found to vary with the velocity ratio k and the injection densimetric Froude number $\mathbb{F}_d$.

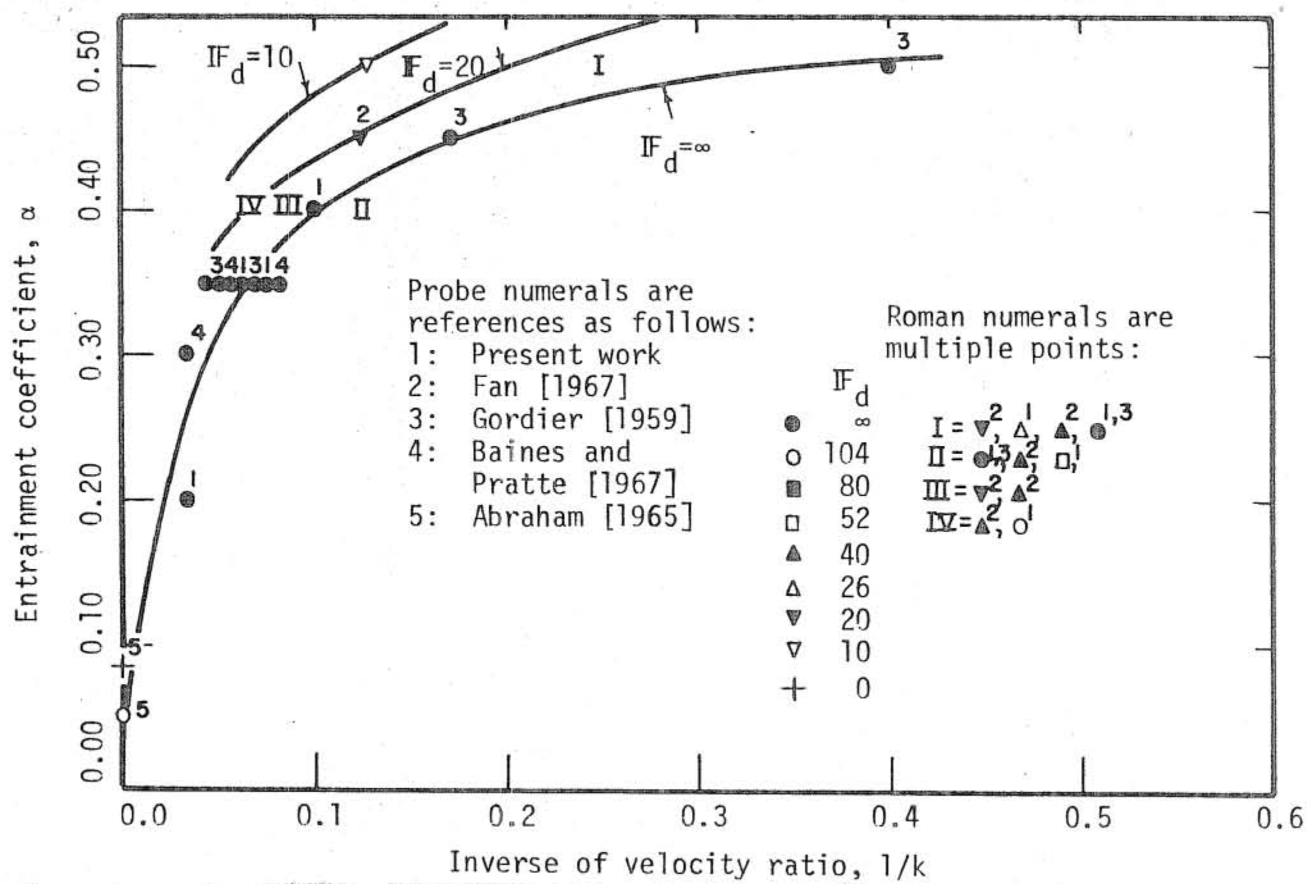

FIGURE 47: Variation of α with $\mathbb{F}_d$ and k

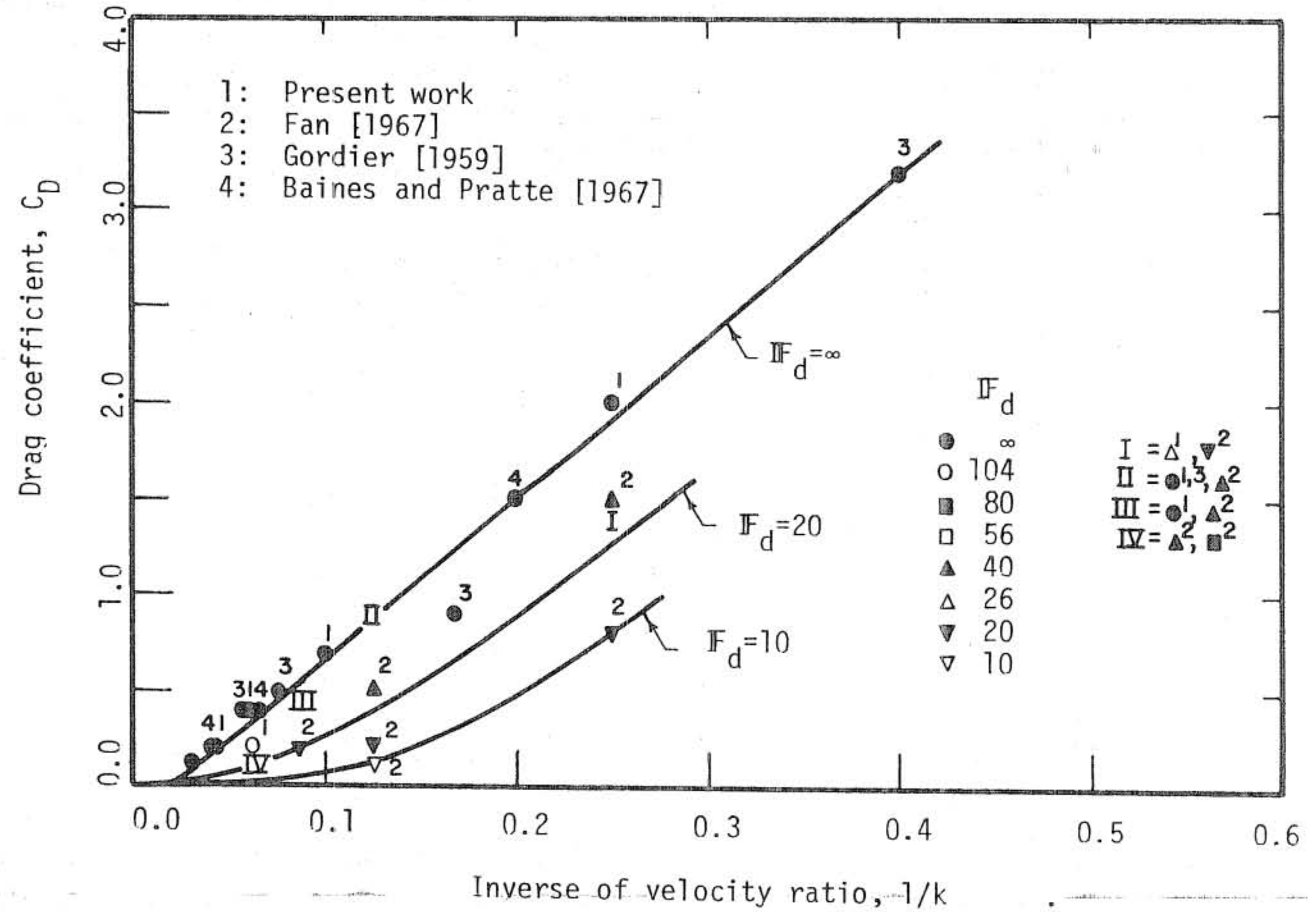

FIGURE 48: Variation of C_D with $\mathbb{F}_d$ and k

5.4.3.1 Entrainment Coefficient

The value of α varied from 0.3 to 0.5 for the range of conditions covered. These values are considerably larger than the values used for jets in stagnant environments, which are 0.082 and 0.057 for simple plumes ($\mathbb{F}_d = 0$) and simple jets ($\mathbb{F}_d = \infty$), respectively [Abraham, 1969]. The larger α values found here are mainly due to the increased entrainment due to interaction of the crossflow. The crossflow type entrainment (Section 2.1.2.2) is the main contributor to entrainment for the jets in crossflow. It is possible that the representation of the entrainment function (Eq. 2-5) could be changed to reduce the range of α values or ideally to give a constant α for all k and $\mathbb{F}_d$. This possibility was not investigated as part of this work since the detailed representation of entrainment was not the primary objective. The value of α decreases as the velocity ratio k increases for constant $\mathbb{F}_d$ (Fig. 47). In the limiting case when k approaches infinity (i.e., for a stagnant ambient fluid), α values of 0.057 and 0.082 for simple jets and simple plumes respectively, appear to be consistent with the values obtained here. The value of α also decreases slightly as the $\mathbb{F}_d$ increases for a constant k (Fig. 47).

5.4.3.2 Drag Coefficient

The drag coefficient C_D varies from 0.1 to 3.2 for the range of conditions covered. C_D decreases as the velocity ratio k increases and as the densimetric Froude number $\mathbb{F}_d$ decreases (Fig. 48). This variation of C_D, however, cannot be considered independently from that of α or from the form of the entrainment function used (Section 2.2.2.2). Chan and Kennedy [1972] have shown that for different forms of entrainment function, one would obtain different values of C_D for the same value of entrainment coefficient α.

5.4.4 Comparison of the Numerical Model with the Experiments

For a jet issuing perpendicularly into a crossing pipe flow, the experimentally observed variation of σ with L are compared with numerically obtained variations in Figs. 49 and 50. The model, in general, is in good agreement with the experimental observations. As is seen in Table 11, the maximum deviation in the predicted mixing distance for a given σ as compared to experimentally observed mixing distance is always less than 13 percent of the latter in absolute value, with the average deviation being only 3 percent.

The model not only gives satisfactory prediction of the ultimate mixing distances for different injection conditions, but it also successfully simulates the behavior of the jet issuing perpendicularly into crossing pipe flow. For example, in Figs. 49, 50, and 51, the predicted effect of k on mixing is compared with experimental observations. As is seen, the optimum k value corresponding to the fastest mixing is accurately predicted. Furthermore, the numerically predicted effect of $\mathbf{F}_d$ on the mixing is in good agreement with experimental observations. For example, Table 12 shows that for $\mathbf{F}_d > 50$ the mixing becomes essentially independent of initial density disparity, as observed experimentally (Table 10).

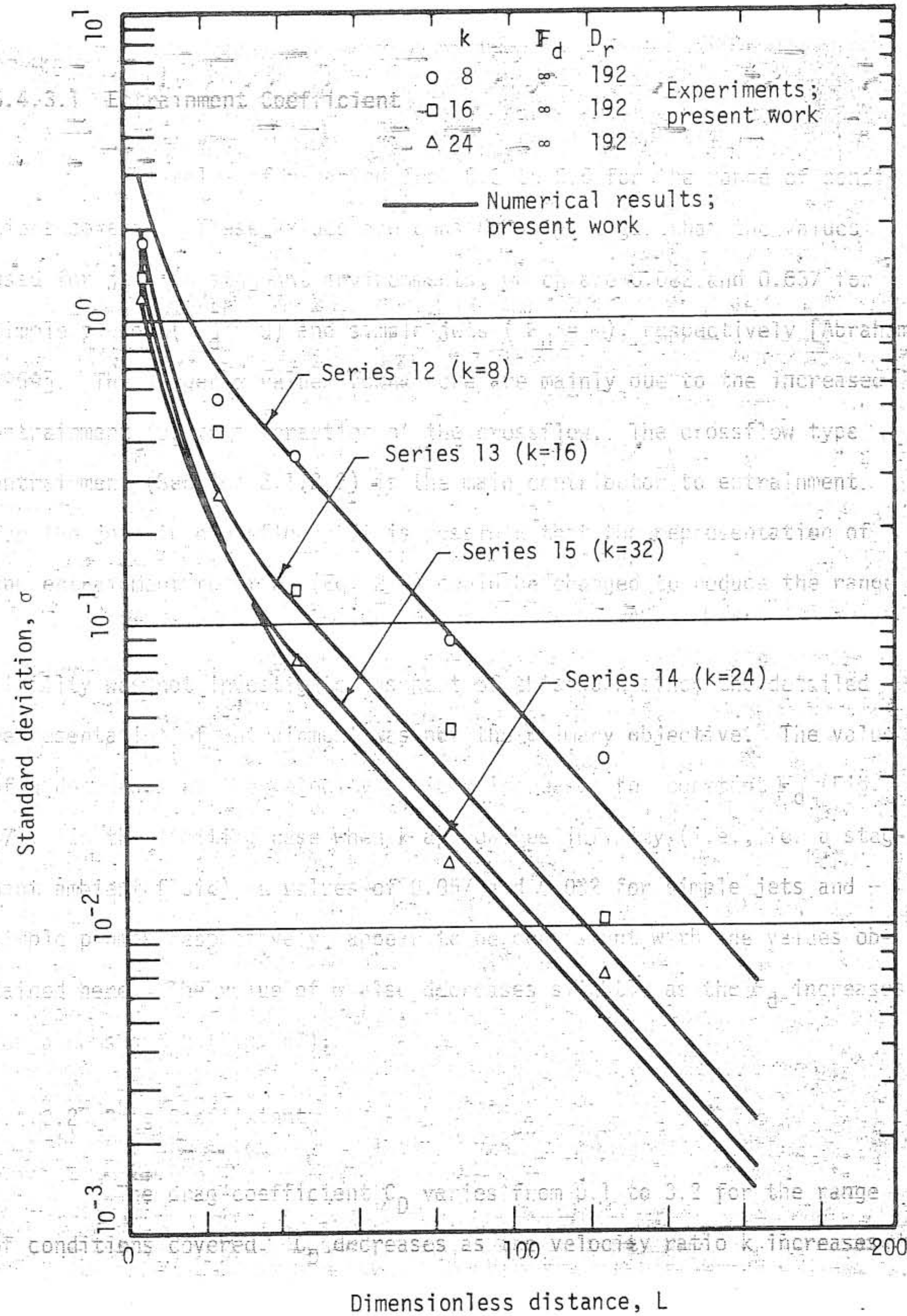

FIGURE 49: Numerical and experimental results for series 12, 13, 14, and 15

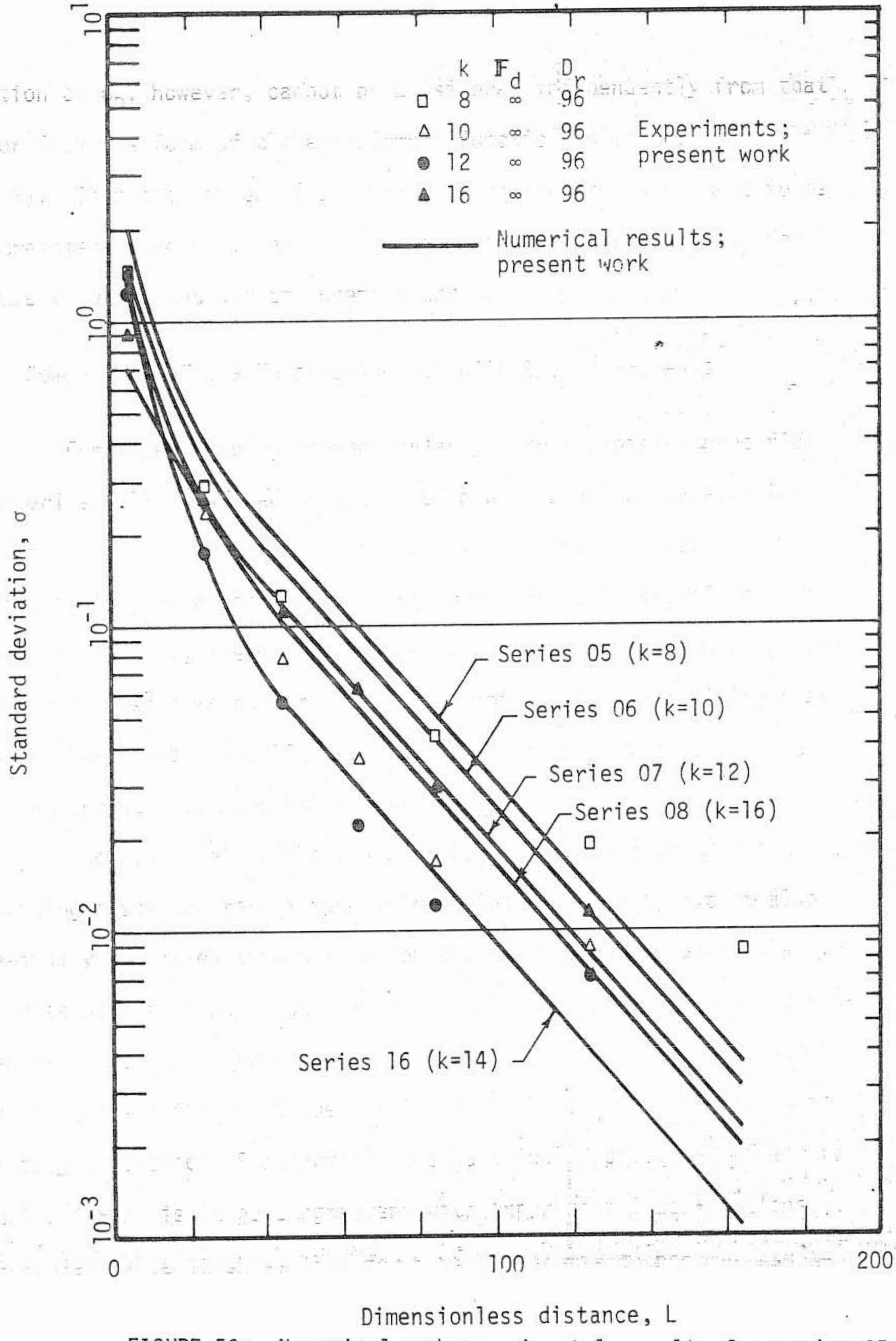

FIGURE 50: Numerical and experimental results for series 05, 06, 07, 08, 16

Table 11

Deviations in Observed and Predicted L

Series #	σ	L_e[1]	L_p[2]	$(L_e - L_p)/L_e \times 100$
05	0.01	148	134	9.4
	0.02	119	112	5.9
06	0.1	108	114	- 5.5
	0.02	83	93	-12.0
07	0.01	100	96	- 4.0
	0.02	70	75	- 7.1
08	0.01	127	128	- 0.8
	0.02	104	107	2.9
12	0.01	168	151	10.5
	0.02	146	130	12.3
13	0.01	132	118	10.6
	0.02	104	97	6.7
14	0.01	106	102	- 3.8
	0.02	82	81	1.2

[1]Subscript e refers to experimental results.

[2]Subscript p refers to numerical results.

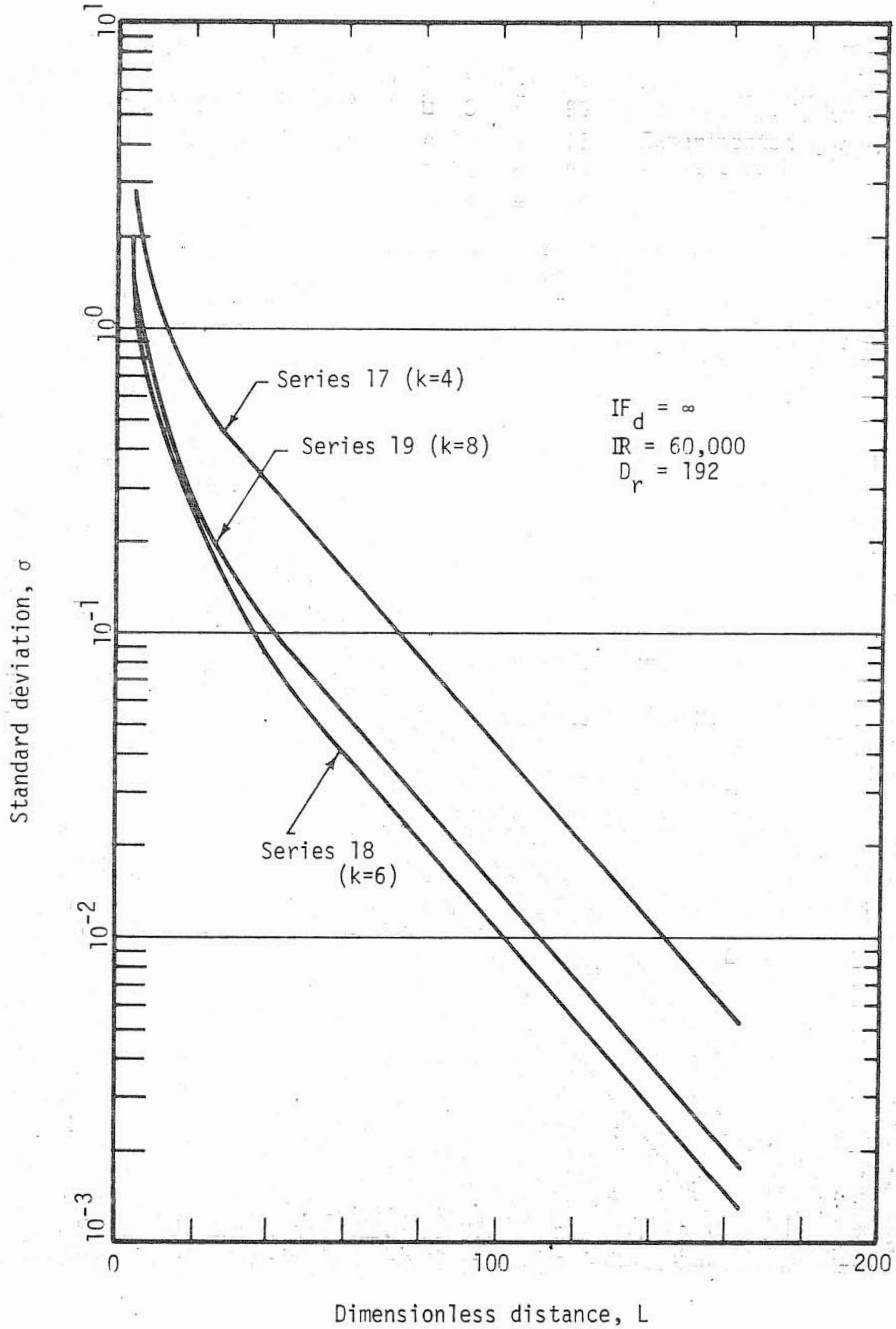

FIGURE 51: Predictions of numerical model for series 17, 18, and 19

Table 12

Variation of L with $\mathbb{F}_d$, k, and σ for $D_r = 96$ as Predicted by the Numerical Model

k	σ	$\mathbb{F}_d$	L	$L_N - L_B/L_N$ [1]	Average Deviation in L
8	0.01	52	134	-2.4%	-1.6%
		∞	132		
	0.02	52	112	-0.9%	
		∞	111		
16	0.01	104	128	+0.8%	+0.9%
		∞	129		
	0.02	104	107	+0.9%	
		∞	108		

[1]Subscripts N and B refers to nonbuoyant ($\mathbb{F}_d = \infty$) and buoyant ($\mathbb{F}_d < \infty$) jets, respectively.

5.4.5 An Empirical Formula for Mixing Distances Due to a Jet Injection

In Section 4.3.1, it has been shown that the dimensionless mixing distance L can be related to the jet and pipe flow characteristics by the following expression:

$$L = f_2 \left(D_r, k, \mathbb{F}_d, \mathbb{R}, \sigma\right) \tag{5-17}$$

In reference to the experimental evidence provided in this study and elsewhere [Nece and Littler, 1972], the effect of the densimetric Froude number is insignificant unless it is smaller than 50. Thus, dropping $\mathbb{F}_d$ as a parameter for large values of $\mathbb{F}_d$, Eq. 5-17 becomes

$$L = f_3 \left(D_r, k, \mathbb{R}, \sigma\right) \tag{5-18}$$

Any change in k for a given D_r (or in D_r for a given k) produces a corresponding change in the relative momentum flux of the jet. The optimum k (or D_r) for a given D_r (or k) actually corresponds to the optimum relative momentum flux of the jet. In other words, there exists an optimum momentum flux of the jet relative to the momentum flux of the crossing pipe flow for which the jet penetration relative to the pipe diameter is optimum and the mixing distance is the shortest. The ratio M of the momentum flux of the jet to that of the crossing pipe flow can be expressed in terms of k and D_r as

$$M = \left(\frac{k}{D_r}\right)^2 \tag{5-19}$$

Introducing M into Eq. 5-18, one obtains

$$L = f_4 \ (M, D_r, \mathbb{R}, \sigma) \tag{5-20}$$

In Eq. 5-20, M and D_r represent the effect of the jet on the mixing distance while $\mathbb{R}$ represents the effect of turbulent transport associated with the pipe flow. (Recall that the pipe roughness has been omitted from the dimensional analysis since only one pipe was used in the present experiments.)

For the case of simple source injections (Sections 5.2.1 and 5.3.1), it has been shown that Eq. 5-20 assumes the following form:

$$L = A \, \mathbb{R}^n \log \left(\frac{I}{\sigma}\right) \sqrt{f_{smooth}/f} \tag{5-21}$$

where I is the intercept, A is proportional to the slope of the linear part of the log σ vs. L graph, and $\mathbb{R}^n$ is derived from the variation of the inverse square root of the friction factor.

For the case of jet injection, it is assumed that the general form of the function f_4 (Eq. 5-20) remains unchanged, but the parameters A and I may be functions of M and D_r. In other words, for jet injection, it is assumed that

$$L = A(M,D_r) \, \mathbb{R}^n \log \left(\frac{I(M,D_r)}{\sigma}\right) \sqrt{f_{smooth}/f} \tag{5-22}$$

The logarithmic dependence of L on σ is supported by the straightline relation between L and log σ for small σ and large L (Figs. 49, 50, and 51).

The exponent n is assumed to be the same as that given previously for simple sources (Sections 5.2.1 and 5.3.1). This assumption is based on the following observations:

1. The near field region, where the jet is active, represents a relatively small fraction of the total mixing length.
2. The major part of the mixing is accomplished by turbulent diffusion associated with the far field region.
3. $\mathbb{R}^n$ is in Eq. 5-22 to represent the variation of the friction factor and the turbulent diffusivity with Reynolds number, and therefore should be the same with either simple sources or jets.

(The influence of the jet is represented in the dependence of A and I on M and D_r, as explained below.)

To find the dependence of I on M and D_r, the intercepts of the straightline parts of the log σ vs. L curves for all experimental and numerical runs were obtained (Table 13) from Figs. 49, 50, and 51 and are plotted in Fig. 52. As an approximation, it was assumed that I depends only on M and that this dependence could be represented by the curve in Fig. 52. With increasing momentum flux ratio M the intercept I decreases until the optimum momentum flux ratio (M = 0.0156) is reached. Further increase in M is followed by an increase in the intercept as the result of overpenetration of the jet.

Once the value of n and the relation between I and M were known, A could be computed using Eq. 5-22 and the available data. The

Table 13

Variation of I with D_r and M

Series	I	D_r	M
4E[1]	1.10	96	0.0017
5E	0.60	96	0.0069
6E	0.26	96	0.0109
7E	0.22	96	0.0156
8E	0.50	96	0.0278
12E	0.98	192	0.0017
13E	0.57	192	0.0069
14E	0.25	192	0.0156
5N[2]	0.79	96	0.0069
6N	0.43	96	0.0109
7N	0.24	96	0.0156
8N	0.64	96	0.0278
12N	1.42	192	0.0017
13N	0.46	192	0.0069
14N	0.29	192	0.0156
15N	0.32	192	0.0278
16N	0.50	96	0.0213
17N	1.11	48	0.0069
18N	0.27	48	0.0156
19N	0.38	48	0.0278

[1]E refers to experiments.

[2]N refers to numerical work.

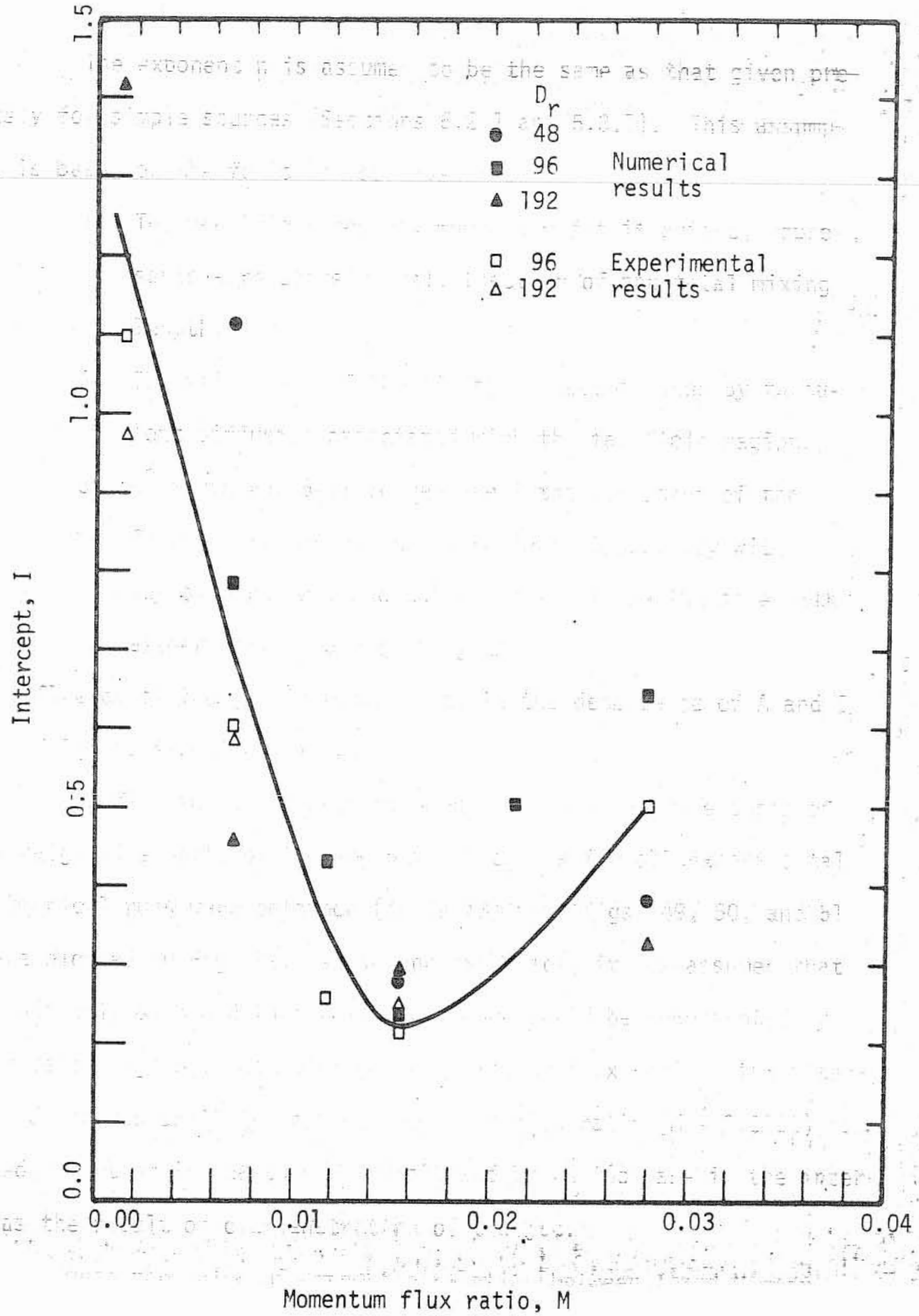

FIGURE 52: Variation of I with M and D_r

results are given in Table 14 and Fig. 53. It can be seen from Fig. 53 that there is no evidence to indicate a dependence of A on either M or D_r. Therefore A was assumed to be constant. $\overline{A}$, the average value of A, was found to be 24.70 with a standard deviation, σ_A, of 2.15. The $\overline{A} + \sigma_A$ value is larger than the 90 percent of all computed A values. Therefore, to be on the conservative side in predicting mixing distances associated with a jet injection, $\overline{A} + \sigma_A$ rather than $\overline{A}$ is used in Eq. 5-22.

Thus, Eq. 5-22 becomes

$$L = 26.9\,\mathbb{R}^{0.10} \log (I/\sigma) \sqrt{f_{smooth}/f} \qquad (5\text{-}23)$$

In using this expression the variation of the intercept I with M is obtained from the curve in Fig. 52. The mixing distances predicted by Eq. 5-23 are compared with the available numerical and experimental data as shown in Fig. 54. As is seen, the calculated curves are a good envelope of the points. For 90 percent of the cases, the predictions of Eq. 5-23 are larger than the numerically or experimentally obtained mixing distances. Furthermore, the cases for which the predictions are smaller than the observations are of less practical interest since the momentum flux ratio M is smaller than the optimum value. On the average, the predicted values of L from Eq. 5-23 are 10 percent larger than the mixing distances to be expected.

5.5 Comparison of Different Single-Point Injection Schemes

Figure 55 shows the variation of σ with L for three different

Table 14

Variation of A with M, D_r and σ as Computed from Eq. 5-22

Series	A	σ	D_r	M
4E[1]	27.26 27.00 26.09	0.01 0.02 0.05	96	0.0017
5E	27.11 26.11 23.79	0.01 0.02 0.05	96	0.0069
6E	23.32 22.26 22.09	0.01 0.02 0.05	96	0.0109
7E	24.84 22.41 24.48	0.01 0.02 0.05	96	0.0156
8E	24.92 24.80 23.33	0.01 0.02 0.05	96	0.0278
12E	26.94 27.37 26.09	0.01 0.02 0.05	192	0.0017
13E	24.18 22.82 23.79	0.01 0.02 0.05	192	0.0069
14E	24.88 26.26 26.96	0.01 0.02 0.05	192	0.0156
5N[2]	24.54 24.58 24.98	0.01 0.02 0.05	96	0.0069

Table 14 (Continued)

Series	A	σ	D_r	M
	24.61	0.01		
6N	24.94	0.02	96	0.0109
	26.04	0.05		
	28.85	0.01		
7N	24.02	0.02	96	0.0156
	24.88	0.05		
	25.11	0.01		
8N	25.51	0.02	96	0.0278
	26.00	0.05		
	24.21	0.01		
12N	24.37	0.02	192	0.0017
	24.64	0.05		
	21.61	0.01		
13N	21.29	0.02	192	0.0069
	20.52	0.05		
	25.34	0.01		
14N	25.94	0.02	192	0.0156
	27.48	0.05		
	21.19	0.01		
15N	20.51	0.02	192	0.0278
	19.33	0.05		
	26.60	0.01		
16N	27.45	0.02	96	0.0213
	29.46	0.05		
	26.37	0.01		
17N	26.77	0.02	48	0.0069
	27.95	0.05		

Table 14 (Continued)

Series	A	σ	D_r	M
18N	25.09 25.62 27.48	0.01 0.02 0.05	48	0.0156
19N	21.78 21.46 20.66	0.01 0.02 0.05	48	0.0278

[1]E refers to experiments.

[2]N refers to numerical work.

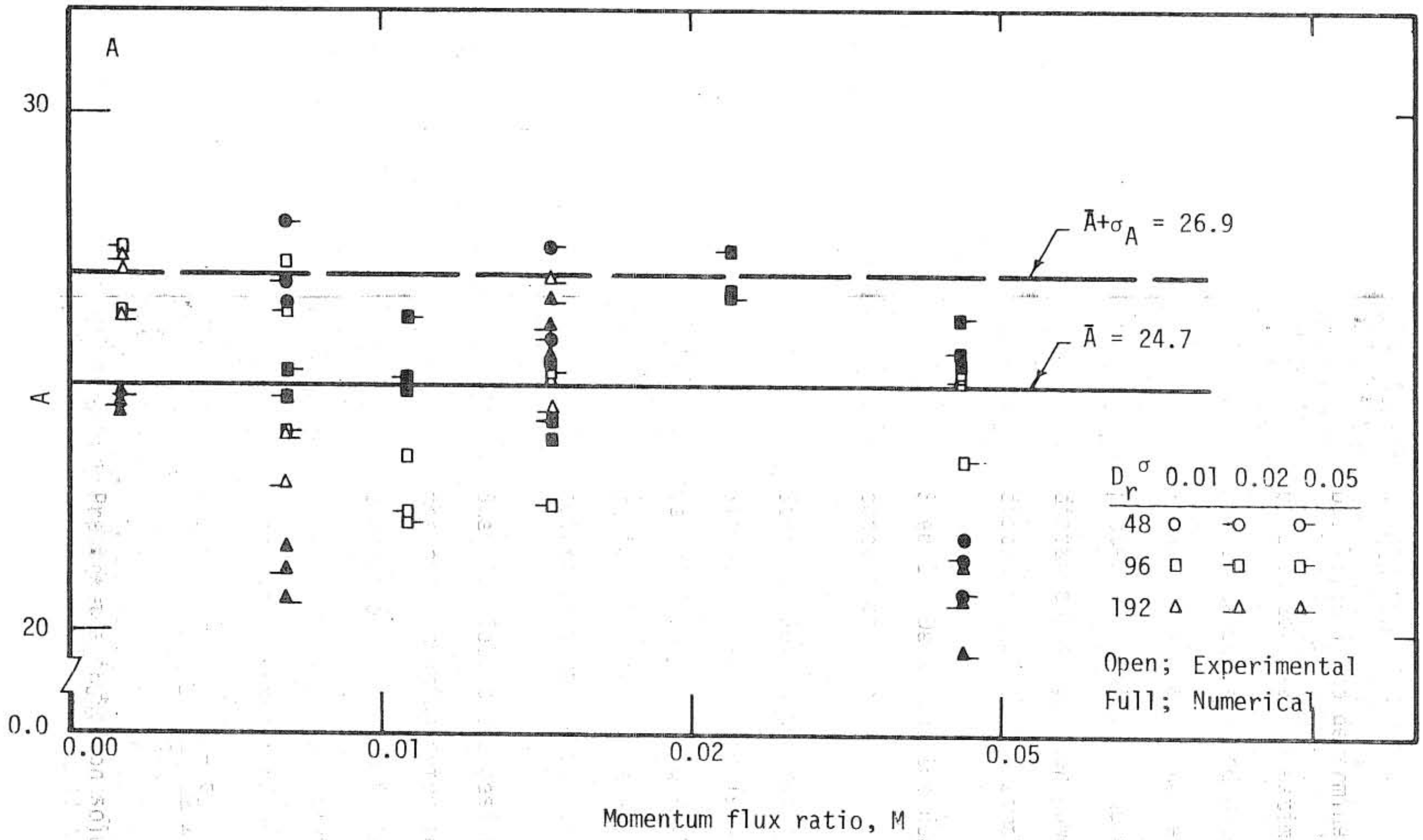

FIGURE 53: Variation of A with M and D_r

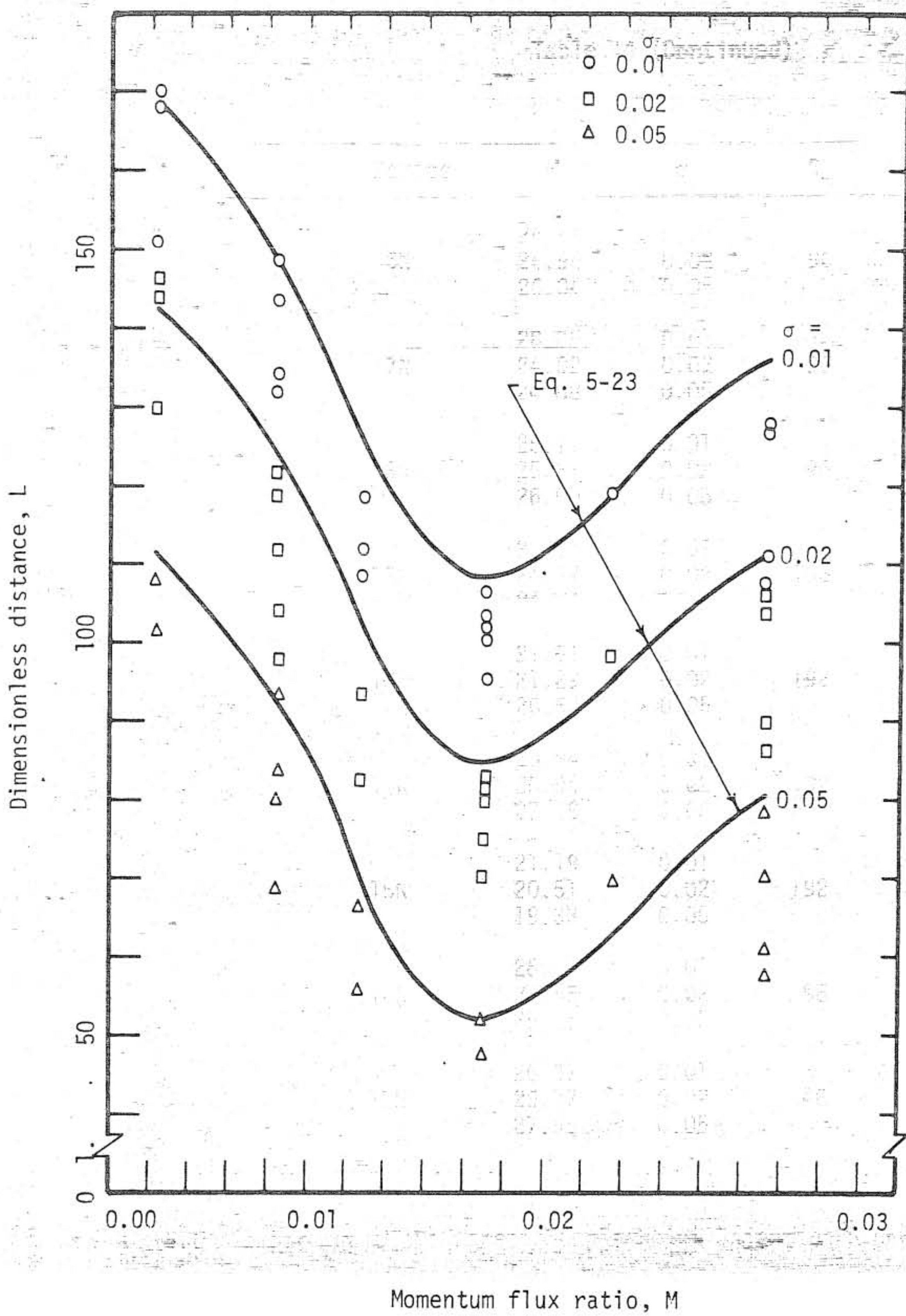

FIGURE 54: Comparison of Eq. 5-23 with experimental and numerical results

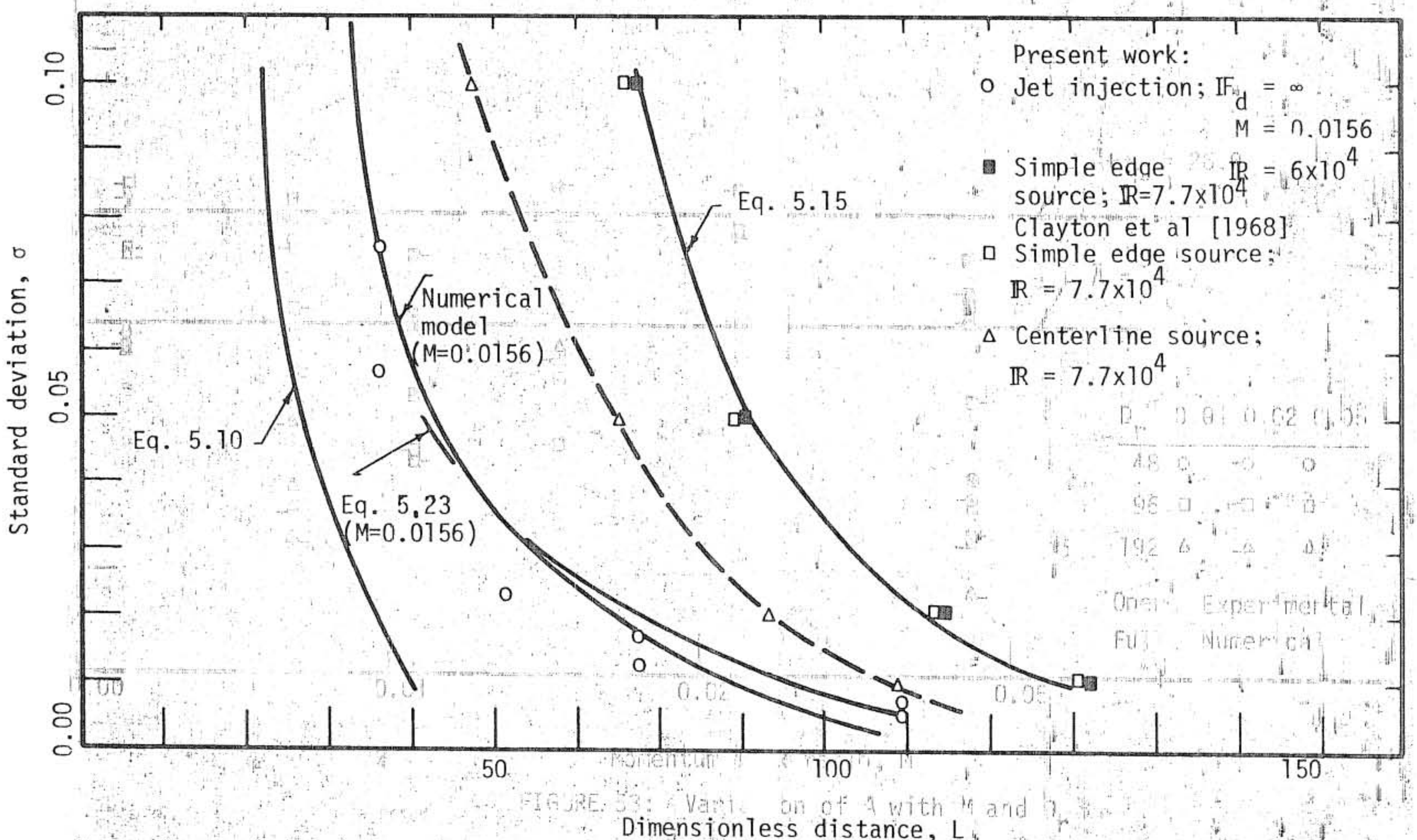

FIGURE 55: Comparison of mixing for different single-point injection schemes

types of single-point injections, namely a centerline source, a wall source, and a jet perpendicular to the pipe wall. For a centerline source, the figure shows both a calculated curve for an assumed axisymmetrical situation and an empirical curve.

The simplest tracer source is a simple source located at the pipe wall, but this results in the longest mixing distance as compared to mixing distances for other injection schemes (Fig. 55). The mixing distance can be reduced by using a simple centerline source. However, practical difficulties in obtaining perfectly axisymmetric conditions usually cause mixing distance to be greater than that calculated for a centerline source (Section 5.2.2). On the other hand, further reductions in mixing distance as compared to a wall source can be obtained by using a jet rather than a simple source located at the wall of the pipe. It has been shown that the mixing distance for a jet perpendicular to the wall could be minimized if the ratio M of momentum fluxes of the jet and the pipe flow is optimum. In Fig. 55, the mixing distance for a jet with optimum M is also shown. As is seen, the shortest mixing distance for the single-point injection considered is the jet injection at the optimum M ratio. The reduction in mixing distance of approximately 50 pipe diameters has been observed by using a jet as compared to a simple edge source. The mixing distance for the jet injection is not as small as that for the calculated curve for a centerline injection; however, the symmetrical case is very difficult to obtain and therefore should not enter a realistic comparison of physically achievable situations for practical applications.

The numerical model developed to simulate the behavior of a buoyant or a nonbuoyant jet located at the pipe wall and issuing perpendicularly into the crossing pipe flow successfully predicts the resulting mixing (Section 5.5.4). Furthermore, it was found that a relation of the form (Eq. 5-14)

$$L = A\,\mathbb{R}^{n} \log (I/\sigma) \sqrt{f_{smooth}/f} \tag{5-24}$$

can be used in predicting the mixing distance for each of the aforementioned injection schemes. The parameters A, I, and n corresponding to each injection scheme were either theoretically or empirically determined and are summarized in Table 15. The agreement between Eq. 5-14 and the experimental findings are good for a simple edge source and for a jet located at the pipe wall if $\mathbb{F}_d > 50$. As can be seen from Fig. 55, there are significant distances between the theoretical curve for a centerline injection and the experimental results. This is due to the fact that the theoretical representation assumes axisymmetry, whereas this is practically impossible to achieve physically (as previously mentioned in Section 5.2.2). Therefore, if the theoretical values for A and I are used in Eq. 5-24, the predicted values of L are too small as compared to the data. On the other hand, if Eq. 5-24 is used to give empirical values of A and I, it is found that these values are different for different investigators (and different centerline injection systems). Therefore, the use of Eq. 5-24 for the prediction of L for centerline injections is not recommended.

Table 15

Constants A, I, and n of Eq. 5-24

Type of Injection	A	I	n	σ_u
Simple Edge Source	20.50	2.4	0.10	0.10
Simple Centerline Source	6.80	2.37	0.104	0.10
Jet Injection	26.85	I = I(M); Figure 52	0.10	0.05

Since Eq. 5-24 gives a linear relation between L and log σ, it cannot be applied over the full range of L and σ values. See, for example, Figs. 22, 23, 49, 50, and 51. For large σ values (i.e., for small L) Eq. 5-24 cannot be applied. Table 15 gives upper limit, σ_u, for the applicability of Eq. 5-24 for each injection scheme. Furthermore, σ values which are calculated from Eq. 5-24 but which are smaller than the experimental accuracy of the concentration detection have no practical value. In other words, the accuracy of the measurement sets forth a lower limit of σ which should be calculated from Eq. 5-24.

6. APPLICATIONS

Knowledge of the behavior of a jet injected into a crossing, fully-established pipe flow has direct applications in numerous ways. In this chapter, the application to two major areas of practical interest is illustrated.

6.1 Use of Jet Injections in Discharge Measurements in Pipes

One major area in which the knowledge of the mixing distance for a jet injection has direct application is the use of tracer techniques for discharge measurements in pipes. As described earlier (Chapter 1), tracer techniques are based on the mass balance of tracer between the injection location and a section of the pipe where the tracer is adequately mixed so that measuring the concentration at any point in the cross section is equivalent to measuring the average concentration.

With reference to discussion in Chapter 1, the mass balance of tracer can be written as

$$Q = q \left[\frac{c_o - \bar{c}}{\bar{c} - c_p}\right] \qquad (6\text{-}1)$$

where Q is the unknown flow rate in the pipe, q is the volumetric injection rate, c_p is the background concentration of tracer in the pipe flow, c_o is the concentration of tracer in the injection solution, and $\bar{c}$ is the tracer concentration in the pipe flow after adequate mixing has been achieved. Equation 6-1 assumes that the tracer is conservative. If the available pipe length downstream from the injection point is longer than the mixing distance needed for adequate mixing to take place, Q can be obtained by measuring the concentration at only one point in the cross section. Since the mixing distance required for a jet injection has been shown to be shorter than that for a simple source at the wall (Chapter 5), the use of a jet as a tracer source can increase the applicability of the tracer technique in discharge measurements in pipes.

6.1.1 A Procedure for Short Pipes

If the available pipe length downstream of the injection point is too short to make use of a simple source, a jet injection can be used to shorten the required mixing distance. The shortest mixing distance for a jet injection is achieved when the jet is injected with optimum momentum flux ratio (M = 0.0156) as discussed in Chapter 5. However, unless the flow rate in the pipe is known, the optimum injection rate cannot be determined *a priori*. Therefore an iterative procedure (as described below) is needed to determine the optimum injection rate and the flow rate in short pipes.

Step 1. Select the desired degree of completeness of mixing σ. This, of course, influences the accuracy of determination of Q. Using the selected value of σ, the design capacity (or expected maximum flow rate in the pipe) Q_{max}, the pipe diameter D, and the smoother end of the possible range for wall roughness, estimate the mixing distance L (Eq. 5-26) for a jet injection with an assumed optimum flux ratio M = 0.0156.

Use Table 15 to determine the appropriate values of A, n, and I to be used in Eq. 5-26 in estimating L. The mixing distance L is the minimum distance required between the injection hole and the sampling port to assure the adequate level of mixing for the entire range of flows expected in the pipe. Therefore, the sampling port should be located a distance L or greater downstream from the injection port. The actual distance (L_1) to the sampling port should be as large as feasible.

Step 2. Determine the density ρ_a of the pipe fluid and the background concentration c_p.

Step 3. Select the ratio of injection rate q to the pipe flow rate Q. Since Eq. 5-26 which is used in estimating mixing distances has been verified only for $q/Q < 0.05$, q/Q should not be greater than 0.05. This ratio will, of course, ultimately influence the value of q and the required injection equipment.

Step 4. Select the desired value of $\bar{c}$ within the measurement range of the concentration detection device to be used. (The value $\bar{c}$ is the concentration of tracer in the pipe flow after adequate mixing has taken place.) Having $\bar{c}$ selected, the concentration c_o for the injection solution can be determined by rearranging Eq. 6-1 to give

$$c_o = \frac{\bar{c} - c_p}{q/Q} + \bar{c} \tag{6-2}$$

Prepare the injection solution so that the concentration of tracer in the solution is equal to c_o given by Eq. 6-2. Then determine ρ_o, the density of the injection solution.

Step 5. The momentum flux ratio M (Eq. 5-19) can be written as

$$M = \frac{\rho_o}{\rho_a} \left(\frac{q}{Q} D_r\right)^2 \tag{6-3}$$

Rearranging Eq. 6-3, one obtains

$$D_r = \frac{\sqrt{\rho_o/\rho_a \; M}}{(q/Q)} \tag{6-4}$$

Determine D_r from Eq. 6-4 for M = 0.0156 and q/Q of Step 3. Then, the injection hole diameter d is determined from Eq. 6-5;

$$d = \frac{D}{D_r} \tag{6-5}$$

Select the closest commercial pipe size to this d and correct D_r, q/Q, and c_o values. First, using the selected injection hole diameter, obtain D_r ratio from Eq. 4-4. Then using this D_r ratio and M = 0.0156 determine q/Q from Eq. 6-3. Finally, determine c_o from Eq. 6-2 for this q/Q.

Step 6. Estimate the discharge in the pipe. Call this first estimate Q_1. Q_1 is less than or equal to Q_{max} of Step 1. Then using q/Q of Step 3 and this Q_1 determine the first trial injection rate q_1.

Step 7. Inject the solution through the injection hole into the pipe flow at a rate q_1 of Step 6 for long enough to assure the concentration at the injection port has reached to a steady value. Measure $\overline{c}_1$ at the sampling port. This value of $\overline{c}_1$ is not necessarily equal to the true $\overline{c}$ since the actual M value for the injection may not have been equal to the optimum value and therefore the required degree of mixing may not have taken place.

Step 8. Replacing $\overline{c}$ in Eq. 6-1 by $\overline{c}_1$, calculate a second estimate Q_2 for the flow rate in the pipe. Then using this Q_2 and actual q_1 of Step 6 determine M_2 from Eq. 6-3. Check that $q_1/Q_2 < 0.05$ and the densimetric Froude number (Eq. 4-6) for q_1 is greater than 50.

Step 9. Calculate the mixing distance L_2 (Eq. 5-26) corresponding to Q_2 and M_2 of Step 8. The appropriate values of constants A, n, and I in Eq. 5-26 are given in Table 15. If L_2 is less than or equal to L_1 of Step 1, the prescribed degree of completeness of mixing was actually achieved and therefore Q_2 is the true discharge. On the other hand, if $L_2 > L_1$, replace Q_1 of Step 6 by Q_2 of Step 8 and repeat Steps 6 through 9. This can be done in as many cycles as necessary, but normally only two or three trial injection rates are needed in order to obtain Q.

The accuracy of this method depends on the steadiness and accuracy of q (as well as the accuracy of concentration and density determinations). Clayton et al. [1968] give detailed consideration to several aspects of the accuracy.

An example is provided below to demonstrate the procedure described above. In order to provide realistic numbers, the numerical values in the example are either taken directly from the actual measurements made during experimental program or are interpolated from the results of those measurements.

Step 1. $\sigma = 0.01$

$D = 0.5$ ft

$Q_{max} = 1.000$ cfs

Range of wall roughness: Smooth to 0.0001. Therefore

$f = f_{smooth}$.

For a jet injection with optimum momentum flux ratio ($M = 0.0156$) the values

$A = 26.9$

$n = 0.10$

$I = 0.22$

are read from Table 15. Therefore

$$L = 29.6\left[\frac{1.0 \times 0.5}{\frac{\pi}{4}(0.5)^2 \times 10^{-5}}\right]^{0.10} \log\left(\frac{0.22}{0.01}\right) = 124$$

(The sampling port was located so that $L_1 = 124$.)

Step 2. $\rho_a = 1$ g/cc

$c_p = 0$ mg/ℓ. (In the experimental program, the concentration detection equipment was balanced at the background level and therefore background reading was always equal to zero. Normally $c_p \neq 0$.)

Step 3. $q/Q = 0.0013 < 0.05$

Step 4. $\bar{c} = 30$ mg/ℓ

$$c_o = \frac{30.0 - 0.0}{0.0013} + 0.0 = 23000 \text{ mg/ℓ}$$

$\rho_o = 1$ g/cc. (In the experimental program, the density of injection solution was controlled and therefore $\rho_o = \rho_a$. Normally the density of injection solution would be greater than the ambient density because of addition of the tracer.)

Step 5. $D_r = \sqrt{0.0156 \times 1/1}\ /0.0013 = 96$

$d = \frac{0.5}{96} = 0.052$ ft = 1/16 in. (In the experimental program, the injection port was constructed so that the injection hole diameter was exactly 1/16 in.)

Step 6. $Q_1 = 0.313$ cfs < 1.0 cfs

$q = 0.0013 \times 0.313 = 0.00041$ cfs

Step 7. $\bar{c}_1 = 40.7$ mg/ℓ

Step 8. $$Q_2 = 0.00041 \frac{23000 - 40.7}{40.7 - 0.0} = 0.231 \text{ cfs}$$

$$M_2 = \left(\frac{0.00041}{0.231} \times 96\right)^2 \times 1/1 = 0.02893$$

$$\frac{q_1}{Q_2} = \frac{0.00041}{0.231} = 0.0018 < 0.05$$

$$\mathbb{F}_d = \frac{\dfrac{0.00041}{\frac{\pi}{4}(0.0052)^2}}{\sqrt{\dfrac{1-1}{1} \times 32.7 \times 0.0052}} = \infty > 50$$

Step 9. $L_2 = 26.9\left(\dfrac{0.231 \times 0.5}{\frac{\pi(0.5)^2}{4} \times 10^{-5}}\right)^{0.10} \log\left(\dfrac{0.55}{0.01}\right) = 140$

$L_2 > L_1 = 124$

Step 6a. $Q_2 = 0.231$ cfs

$q_2 = 0.0013 \times 0.231 = 0.00030$ cfs

Step 7a. $\bar{c}_2 = 29.1$ mg/ℓ

Step 8a. $Q_3 = 0.00030 \dfrac{23000 - 29.1}{29.1 - 0.0} = 0.237$ cfs

$$M_3 = \left(\frac{0.00030}{0.237} \times 96\right)^2 \times 1/1 = 0.0156$$

$$\frac{q_2}{Q_3} = \frac{0.00030}{0.237} = 0.00013 < 0.05$$

$$\mathbb{F}_d = \frac{\dfrac{0.0030}{\frac{\pi}{4}(0.0052)^2}}{\sqrt{\frac{1-1}{1} \times 32.2 \times 0.0052}} = \infty > 50$$

Step 9a. $L_3 = 26.9\left(\dfrac{0.237 \times 0.5}{\pi/4(0.5)^2 \times 10^{-5}}\right)^{0.1} \log\left(\dfrac{0.22}{0.01}\right) = 108$

$L_3 < L_1$

Therefore $Q_3 = 0.237$ cfs is the true discharge in the pipe. When the flow rate obtained by the procedure described above is compared with the discharge $Q = 0.235$ cfs given by the flow meter in the experiments, it is seen that the deviation is less than 1 percent of the latter.

The first assumed Q_1 made the actual M greater than the optimum. Thus, the jet actually overpenetrated and the measured $\bar{c}_1$ was therefore greater than the true $\bar{c}$ since in this example, the measurement port was located on the opposite side of the pipe from the injection port.

This procedure is somewhat complicated in that it may require the use of more than one injection rate and corresponding multiple measurements of $\bar{c}_1$. However, this method is needed only for cases where the mixing distance required for a simple source injection exceeds the available pipe length. Of course, the potential advantages of this method can be weighed against multi-point injections [Clayton et al. 1968] and other measurement techniques.

6.1.2 A Procedure for Long Pipes

If the available length downstream of the injection point is not restricted, a conventional simple source injection can safely be used. However, the use of a jet injection may be preferred since the initial mixing in the near field region adds a sort of safety factor to assure complete mixing in a shorter distance as compared to a simple source injection. A procedure is described below for the use of a jet as a tracer source when there is no restriction on the pipe length downstream of the injection point.

Step 1. Select the desired degree of completeness of mixing σ. Using the selected value of σ, the design capacity (or expected maximum flow rate in the pipe, Q_{max}), the pipe diameter D, and the smoother end of the possible range for wall roughness, estimate the mixing distance L for a simple source injection from Eq. 5-26. Use Table 15 to determine the appropriate values of A, n, and I to be used in Eq. 5-26 in estimating L. Because L is the longest mixing distance to be expected at all flow rates smaller than Q_{max} the complete mixing is assured at the sampling station. In other words, the sampling port should be located at least a distance L downstream from the injection hole.

Steps 2 through 7. Follow Steps 2 through 7 of the procedure described for short pipes in the preceding section.

Step 8. Using $\overline{c}_1$ of Step 7 as $\overline{c}$, calculate Q_2 as the flow rate in the pipe.

An example is provided below to demonstrate the procedure described above. The numerical values in the example are directly taken from the measurements made during the experimental program.

Step 1. $\sigma = 0.01$

$Q_{max} = 0.625$ cfs

$D = 0.5$ ft

Range of wall roughness: Smooth to 0.0001. Therefore

$f = f_{smooth}$.

For a simple edge source, the values

$A = 20.5$

$n = 0.10$

$I = 2.4$

are read from Table 15. Therefore

$$L = 20.50 \left(\frac{0.625 \times 0.5}{\pi/4(0.5)^2 \times 10^{-5}}\right)^{0.10} \log\left(\frac{2.4}{0.01}\right)\sqrt{f_{smooth}/f_{smooth}}$$

$$L = 164 \text{ pipe diameters}$$

Step 2. $\rho_a = 1 \text{ g/cc}$

$c_p = 0.0 \text{ mg/}\ell$

Step 3. $q/Q_p = 0.0013 < 0.05$

Step 4. $\bar{c} = 30.0 \text{ mg/}\ell$

$$c_o = \frac{30.0 - 0.0}{0.0013} = 23000 \text{ mg/}\ell$$

$\rho_o = 1 \text{ g/cc}$

Step 5. $D_r = \sqrt{0.0156 \times 1/1} / 0.0013 = 96$

$$d = \frac{0.5}{96} = 0.0052 \text{ ft} = 1/16 \text{ in.}$$

Step 6. $Q_1 = 0.156 \text{ cfs}$

$q_1 = 0.0013 \times 0.156 = 0.00021 \text{ cfs}$

Step 7. $\bar{c}_1 = 19.9 \text{ mg/}\ell$

Step 8. $Q_2 = 0.00021 \dfrac{1/1 \times 23000 - 19.9}{19.9} = 0.236 \text{ cfs}$

Therefore the flow rate in the pipe is 0.236 cfs. When the flow rate obtained by the procedure described above is compared with the discharge Q = 0.235 cfs given by the flow meter, it is seen that the deviation is less than 1 percent of the latter.

6.2 Use of a Pipe Segment as a Mixing Chamber

A second major area in which the knowledge of the mixing distance for a jet injection has direct applications is in using a pipe segment as a mixing chamber. For example, chlorination of a water supply can be performed in a segment of the main prior to any branching rather than in a specifically designed facility. The length of the pipe which is required prior to any branching in order to prevent excessive or deficient chlorination in branches can be determined from the present work. (Of course, required contact time must be considered in addition to the mixing distance.) Similarly the chemical neutralization of ecologically harmful waste materials from an industrial plant can be accomplished in a segment of pipe. The present work can be used to determine the length of the pipe required before discharging into a body of water or atmosphere. In what follows a typical design procedure for the use of a pipe segment as a mixing chamber is provided.

6.2.1 A Typical Design Procedure

This example considers a main water supply main which is 3.0 ft in diameter. The maximum flow rate is 50 cfs.

Step 1. Using the maximum Q, obtain the mixing distance L required for a jet injection with optimum momentum flux ratio of M = 0.0156. The mixing distance is calculated by using Eq. 5-26. The appropriate values of A, n, and I of Eq. 5-26 are found from Table 15 as

$A = 26.90$

$n = 0.10$

$I = 0.22$

Then select the required degree of completeness of mixing, say $\sigma = 0.01$. Using the smoother end of the range of the wall roughness determine the friction factor of the pipe for $Q = Q_{max}$. Say, in this particular example, that smoother end of the range of the wall roughness is a smooth boundary; therefore, select the pipe friction factor corresponding to the hydraulically smooth flow. For Q = 50 cfs and $\sigma = 0.01$, one obtains

$$L = 26.9 \log \left(\frac{0.22}{0.01}\right)\left(\frac{50 \times 3}{\frac{\pi}{4}(3)^2 \times 10^{-5}}\right)^{0.10}$$

$$L = 155 \text{ pipe diameters.}$$

Therefore, the first branching should not be before 155 pipe diameters downstream of the injection point. For some chemicals, a contact time is required, so that additional distance must be provided so that the chemical not only becomes adequately mixed but also has sufficient contact time before any branching. This additional distance L_c can be calculated from Eq. 6-7 using the required contact time t_c and the average pipe velocity $\bar{\bar{u}}$;

$$L_c = \bar{\bar{u}}\, t_c/D = Qt_c/(AD) \qquad (6\text{-}7)$$

Say, for the additive considered in this example t_c is 100 sec, then

$$L_c = \frac{10 \times 100}{\frac{\pi}{4}(3)^2 \times 3} = 47$$

Therefore, the injection port should be at least 155 + 47 = 202 pipe diameters upstream of the first branching.

Step 2. Select the ratio of injection rate q to the pipe flow rate Q. Since Eq. 5-26 which is used in estimating L has been verified only for $q/Q < 0.05$, q/Q should be smaller than 0.05. Say, a typical value of 0.001 is selected. Thus, for $Q = Q_{max}$, $q = 50 \times 0.001 = 0.05$ cfs.

Step 3. Determine the flow density ρ_a, say 1 g/cc, and the background concentration c_p, say 2 mg/ℓ. Then obtain the concentration of tracer in the injection solution for q/Q of Step 2 from Eq. 6-2; say $\bar{c}$ = 10 mg/ℓ, then

$$c_o = \frac{10 - 2}{0.001} + 2 = 8002 \text{ mg/ℓ}$$

This calculation implies that part of the necessary concentration $\bar{c}$ is being supplied by the background concentration c_p. Thus, if c_p is variable, the minimum c_p should be used.

Step 4. Obtain the relationship between the injection solution density ρ_o and the concentration of tracer c_o in the injection solution; say $\rho_o = \rho_a (1 + f_6(c_o))$ with $f_6(c_o) = 10^{-6}\ c_o$. Then determine D_r, for M = 0.0156, q/Q of Step 2, and c_o of Step 3 from Eq. 6-4 as

$$D_r = \sqrt{\frac{0.0156\ (1 + 8002 \times 10^{-6})}{1.0}}\ /\ 0.001 = 125.4$$

Then, calculate the injection hole diameter d from Eq. 6-5 as

$$d = 3/125.4 = 0.0239 \text{ ft} = 0.287 \text{ in.}$$

Select the closest commercial pipe size to this d and correct all previous values as shown below.

The closest commercial pipe size is 1/4 in. Using d = 0.250 in. = 0.0208 ft, obtain D_r ratio as

$$D_r = 3/0.0208 = 144$$

Then using M = 0.0156 and D_r = 144 obtain c_o and q/Q from Eqs. 6-2 and 6-4 by trial and error as

$$q/Q = 0.00087$$

$$c_o = 9200 \text{ mg}/\ell$$

Thus, for $Q = Q_{max}$

$$q = 50 \times 0.00087 = 0.0435 \text{ cfs.}$$

Therefore, for a maximum flow rate of 50 cfs with a background concentration of 2 mg/ℓ, an injection solution containing 9200 mg/ℓ tracer injected at a rate of 0.0435 cfs through an injection hole of 1/4 in. in diameter will provide a flow containing 10 mg/ℓ of additive plus a 100 sec contact time before any branching 202 or more pipe diameters downstream of the injection port.

This example has assumed that D is fixed. If a length of 202 diameters is not available, then the determination of D giving consideration to mixing and contact time could be part of the design process. A reduction in D would reduce the absolute length required for mixing but would increase the distance required for contact time since a smaller D would give a larger velocity for a fixed discharge. Thus, the question of whether D should be increased or decreased depends on whether mixing or contact time is the major contributor to the required length.

For many cases, the discharge in the main will vary with time. However, if the rate of variation with time is relatively small, the flow at a given time can be treated as steady. Thus for smaller flow rates (provided that the rate of variation in discharge is small), keeping the q/Q ratio at the design value will assure that the momentum flux ratio will always be equal to the optimum value. The q/Q ratio can be kept constant by varying the injection rate q with varying flow rate in the pipe. This can be achieved automatically by measuring the flow rate in the main and using an automatic control mechanism to regulate q. The discharge Q can be monitored by any of the standard hydraulic methods or the concentration after mixing can be used as an indication of Q as discussed previously. If the concentration is used, the stability of the control circuit would have to be analyzed considering the possible rate of change of Q and the flow (lag) time between the injection port and the location at which the concentration measurement is made. As is seen from Eq. 6-2, the concentration of additive in the injection solution need not be changed since c_o depends on q/Q rather than the absolute value of the flow rate in the pipe.

The power requirement of the pump to be used in pumping the injection solution into the pipe can be calculated by

$$HP = \frac{\gamma_o qH}{550} \tag{6-8}$$

where HP is the required horsepower, γ_o is the specific weight of the injection solution, q is the volumetric injection rate corresponding to Q_{max} and

$$H = \frac{p}{\gamma} + h_L + \Delta H \tag{6-9}$$

where p/γ is the piezometric head at the injection port in feet, h_L is the head loss in the injection circuit in feet, and

$$\Delta H = \frac{8q^2}{\pi^2 g d^4} \tag{6-10}$$

ΔH represents the additional head required to maintain the jet injection. The increase in power associated with ΔH can be determined from Eq. 6-8 by replacing H with ΔH. For this example, the increase in power requirement was found to be 1.25 horsepower.

7. CONCLUSIONS AND RECOMMENDATIONS

Experimental, analytical and numerical results are summarized in Chapter 5. Based on these results, the following conclusions about the behavior of a buoyant or nonbuoyant jet injected perpendicularly into a crossing, fully-established, turbulent pipe flow can be drawn.

1. The behavior of the jet is independent of the initial density disparity at the injection port for jet densimetric Froude numbers greater than about 50. (There were not enough experiments to determine precisely the critical densimetric Froude number.) In any event, unless the densimetric Froude number is close to unity, the primary governing parameter with respect to the jet behavior is the momentum flux ratio, which is defined as the ratio of momentum flux of the jet at the injection port to the momentum flux of the ambient flow. Therefore, in most cases, any additional expense of altering the natural buoyancy of the jet in order to add buoyancy to the momentum would not produce a significant change in the mixing distance.

2. By dividing the analysis into regions a good representation of the flow was achieved. The near field region in which the jet is active represents a very small fraction (less than 2 percent) of the total mixing distance. However, the initial jet mixing and the jet penetration (advection

of jet away from the wall of the pipe) in the near field region are responsible for the reduction in the mixing distance. The major part of the mixing is accomplished by turbulent diffusion associated with the far field region.

3. At a given pipe flow rate, the mixing distance is shorter than that for a simple source injection. This reduction in the mixing distance associated with the use of a jet as a tracer source depends on the momentum flux ratio M. There exists an optimum momentum flux ratio for which the reduction in mixing distance is maximized.
4. For momentum flux ratios of the order of magnitude of the optimum the jet in the near field region does not contact the pipe wall. As long as the jet in the near field region does not contact the pipe wall, the mathematical model based on the numerical integration of conservation of momentum flux, conservation of volume flux, and conservation of mass flux equations is capable of describing the behavior of a jet with or without buoyancy injected into a fully-established pipe flow. The model can be used in predicting mixing distances required for both buoyant and nonbuoyant jet injections.
5. The semi-empirical relation

$$L = A \log (I/\sigma) \mathbb{R}^n (f_{smooth}/f)^{1/2} \qquad (7\text{-}1)$$

can be used in predicting mixing distances required for a simple edge source and a nonbuoyant jet injections. The symbols are defined previously (Eq. 5-14) and appropriate values of A, I, and n are given in Table 15 and accompanying discussion.

6. The knowledge of the circumferential mass diffusivity is important in many respects. Assuming that the mass diffusivities in radial and circumferential directions have similar spatial variations the ratio of circumferential diffusivity to radial diffusivity was estimated to be 1.35. However, this result is far from being conclusive because of the fact that experiments were not specifically designed for evaluation of diffusivities.

Based on the results of this study the following investigations are suggested:

1. The mechanics of the interaction of a jet and a crossflow should be studied in a more detail to bring out a better understanding of the entrainment mechanism.
2. A more detailed study of the far field region could provide better information on the circumferential diffusivity.
3. Effects of bends and changes in pipe cross section in the far field region on the mixing distance should be studied.
4. In some practical cases of interest where a jet can be used as a tracer source the receiving flow is laminar. Therefore, the behavior of a jet injected into a laminar pipe flow should be studied.

LIST OF REFERENCES

Abraham, G., "Entrainment principle and its restrictions to solve problems of jets," J. of Hyd. Res., Vol. 3, No. 2, 1965, p. 1-23.

Abraham, G., "Round buoyant jet in corss flow," Delft Hyd. Lab. Pub. No. 514, 1969, p. 26.

Abramowich, G. N., The Theory of Turbulent Jets, The M.I.T. Press, Massachusetts, 1963.

Ames, W. F., Numerical Methods for Partial Differential Equations, Barnes of Nobley, Inc., N. Y., 1969.

Baines, D. W. and Pratte, B. P., "Profiles of the round turbulent jet in a crossflow," J. of Hyd. Div., ASCE, Vol. 93, HT6, Proc. Paper 5556, 1967, p. 53-64.

Becker, L. and Yeh, W. W-G., "Identification of parameters in unsteady open channel flows," Water Resources Research, Vol. 8, No. 4, 1972, p. 956.

Bernard, R. A. and Wilhelm, R. H., "Turbulent diffusion in fixed beds and packed solids," Chem. Eng. Prog., Vol. 46, 1950.

Bird, R. B., Stewart, W. E., and Lightfoot, E. N., Transport Phenomena, Wiley, N. Y., 1960, 780 p.

Bonnin, J., Dumas, H. and Lievre, R., "Étude de la diffusion saline en regime permanent une conduit circulaire," Proceedings of the IAHR, Lisbon, 1957.

Carslaw, H. S., and Jaeger, J. C., Conduction of Heat in Solids, Clarendon Press, Oxford, England, 1965, 510 p.

Carter, H. H., "A preliminary report on the characteristics of a heated jet discharged horizontally into a transverse current: part 1., constant depth," Tec. Rep. No. 61, Chesapeate Bay Inst., the Johns Hopkins Univ. Baltimore, Md., Nov., 1969.

Chan, T. L. and Kennedy, J. F., "Turbulent nonbuoyant or buoyant jets discharged into flowing or quiscent fluids," Iowa Inst. of Hyd. Res., The University of Iowa, Rep. No. 140, 1972.

Clayton, C. G., Ball, A. M. and Spackman, R., "Deispersion and mixing during turbulent flow of water in a circular pipe," Isotope Research Div., Wantage Research Lab., Wantage, Berkshire (U AERE-R 5569, 1968, 31 p.

Clayton, C. G. and Evans G. V., "The constant-rate-injection and velocity methods of flow measurement for testing hydraulic machines," Isotope Research Div., Wantage Research Lab., Wantage, Berkshire (U.K.), AERE-R 5872, 1968, 50 p.

Collatz, L., The Numerical Treatment of Differential Equations, Springer-Veriaz, Berlin, 1960, 568 pp.

Crank, J., The Mathematics of Diffusion, Clarendon Press, Oxford, England, 1964, 347 p.

Dryden, H. L., "A review of the statistical theory of turblence," NACA, Report No. 392, National Bureau of Standards, Washington, D. C., 1942.

Evans, G. V., "A study of diffusion in turbulent pipe flow," J. of Basic Eng., ASME, Paper 66-FE-A, 1966, 3 p.

Fahien, R. W. and Smith, J. M., "Mass transfer in packed beds," J. of AICHE, Vol. 1, 1955.

Fan, L. - N., "Turbulent buoyant jets into stratified or lowing ambient fluids," W. M. Keck Lab of Hyd. and Water Res., California Inst. of Tech., Report No. KH-R-15, 1967, 196 p.

Fan, L. - N. and Brooks, N. H., Discussion of "Horizontal jets in stagnant fluid of other density," by Abraham, G., J. of Hyd. Div. HY2, 1966, p. 423-429.

Filmer, R. W., and Yevdjevich, V., "Experimental results of dye disfusion in large pipelines," Proc. IAHR, 12th Congress, Vol. 4, 1967.

Ger, A. M., and Holley, E. R., "Turbulent jets in crossing pipe flow: Supplement," To be published.

Glover, J. R., "Multiple-channel conductometer for measuring salinity concentrations in laboratory flows," Iowa Ins. of Hyd. Res., Iowa, Report No. IIHR R.128, 1970.

Gordier, R. L., "Studies on fluid jets discharging normally into moving liquid," St. Anthony Falls Hyd. Lab., Tech. Paper 28, Ser. B, Univ. of Minn., 1959.

Harleman, D.R.F., et al., "Numerical Studies of Unsteady Dispersion in Estuaries," Jour. of the San. Div., ASCE, Vol. 94, SA5, 1960.

Hinze, J. O., Turbulence, McGraw-Hill, N. Y., 1959, 586 p.

Hirst, E., "Buoyant jets with three dimensional trajectories," J. of Hyd. Div., ASCE, Vol. 98, HY12, Paper No. 9378, 1972, p. 1999-2014.

Hoult, D. P., Fay, J. A., and Torney, L. J., "A theory of plume rise compared with field observations," Jour. of Air Poll. Control Assoc., Vol. 19, No. 8, pp. 585-590, 1969.

IBM Application Program, GH20-0205-4, Version III, 1972, 454 p.

Jordan, D. W., "A theoretical study of the diffusion of tracer gas in an airway," Quarterly J. of Mech. and Appl. Math, London, Vol. 14, p. 2, 1961.

Kantorovich, L. V., and Krylov, V. I. (trans. by C. D. Benster), Approximate Methods of Higher Analysis, Interscience Pub., Inc., N. Y., 1964, 681 p.

Keffer, J. F., "The round turbulent jet in a cross-wind," Ph.D. Thesis, University of Toronto, Toronto, Canada, 1962.

Keffer, J. F., "The physical nature of the subsonic jet in a cross stream," NASA, SP-218, 1969, p. 19-36.

Keffer, J. F. and Baines, W. D., "The round turbulent jet in a cross-wind," J. of Fluid Mech., Vol. 10, 1963, p. 481-496.

Laufer, J., "The structure of turbulence in fully developed pipe flow," NACA, Report No. 1174, National bureau of Standards, Washington, D. C., 1954.

Lin, J. T., "Three theoretical investigations of turbulent jets," Iowa Inst. of Hyd. Res., The University of Iowa, Rep. No. 127, 1971.

Milne, W. E., Numerical Solution of Differential Equations, Dever Pub., Inc., N. Y., 1970, 356 pp.

Monin, A. S. and Yaplow, A. M., Statistical Fluid Mechanics, Vol. 1, The MIT Press, Cambridge, 1972, 769 p.

Morton, B. R., "The ascent of turbulent forced plumes in a calm atmosphere," Intern. Jour. of Air Pollution, 1, pp. 184-197, 1959.

Motz, L. H. and Benedict, B. A., "Heated surface jet discharged into a flowing ambient stream," Dep. of Environ. and Water Res. Eng., Vanderbilt Univ., Nashville, Tenn., Rep. No. 4, 1970.

Naudascher, E., "On a general similarity analysis for turbulent jet and wake flows," Iowa Inst. of Hyd. Res., The Univ. of Iowa, IHHR Rep. No. 106, Dec., 1967, 47 p.

Nece, R. E., and Littler, J. D., "Round horizontal thermal-buoyant jet in a crossflow," Charles N. Harris Hydr. Lab., University of Washington, Tech. Rep. No. 34, June, 1973, 55 p.

Platten, J. L. and Keffer, J. F., "Entrainment in deflected axisymmetric jets at various angles to the stream," Univ. of Toronto, Mech. Eng., Report No. TP-6808, 1968.

Robertson, J. M., "A turbulence primer," University of Illinois Eng. Exp. Station Circular No. 79, March, 1965, 28 p.

Roley, G., "Gaseous diffusion at mode rate flow rates in circular conduits," M.S. Thesis, Ames Lab., Iowa State University, Ames, Iowa, 1960.

Seagrave, R. C., "Mass transfer in liquid streams," M.S. Thesis, Ames Lab., Iowa State University, Ames, Iowa, 1960.

Schlichting, H., Boundary Layer Theory, 6th Ed., McGraw-Hill, N. Y., 1968, 747 p.

Siemons, J., "Numerical methods for the solution of diffusion advestion equations," Delft Hyd. Lab. Pub. No. 88, 1970, 47 pp.

Stoy, R. L., and Ben-Haim, Y., "Turbulent jets in a confined cross-flow," ASME, Paper No. 73-FE-15, 6 p.

Taylor, G. I., "The dispersion of matter in turbulent flow through a pipe; Proceedings of the Royal Society, London, Series A, 1954, V. 223, p. 446.

Varga, R. S., Matrix Iterative Analysis, Printice Hall Series in Automatic Computation, 1962.

APPENDIX 1

I. Platinizing Procedure [Glover, 1970]

The circuits for cleaning and platinizing the electrodes are shown in Figure A1. The main difference between these two circuits is the polarity of the battery. Preparation of the solutions is described at the end of this section.

Preparation of the electrodes for the platinizing process consists of the following steps:

1. Heat the platinum-foil electrode white hot, permit the electrode to cool, and then thoroughly wash it with distilled water.
2. Wash the glass beaker and probe electrodes thoroughly with distilled water.
3. Fill the beaker with a 15 N sulphuric acid solution, and place the platinum-foil electrode in the beaker.
4. Adjust the variable resistor shown in Figure A1-a for maximum resistance.
5. Connect both electrodes of the probe as shown in Figure A1 and submerge the electrodes in the solution. After the electrodes are submerged, adjust the variable resistance until the meter indicates a current of 5 milliampers.
6. Continue the cleaning process for approximately two minutes and then remove the electrodes and platinum-foil and wash them thoroughly with distilled water.

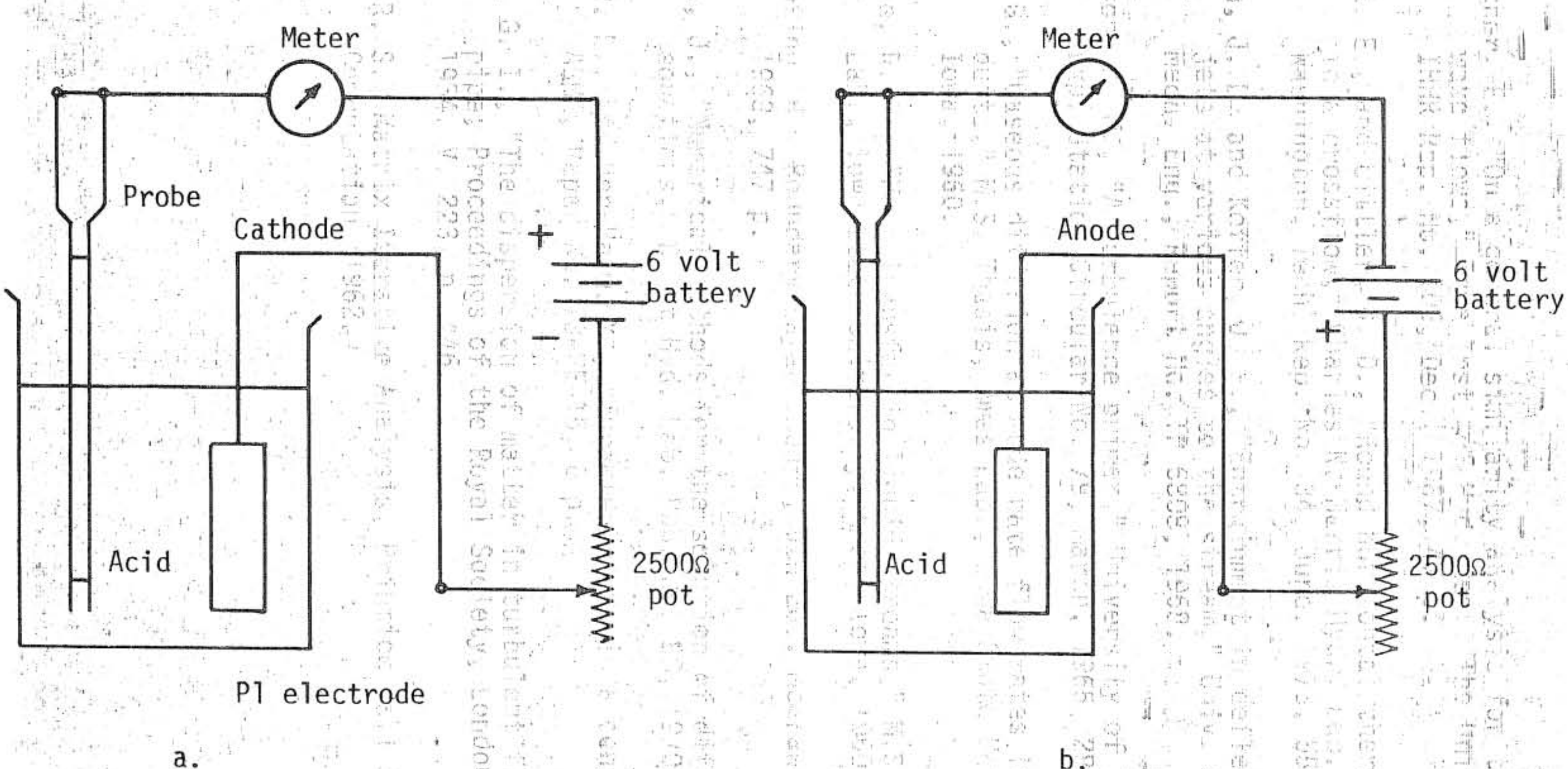

FIGURE A1. Circuits for cleaning (a) and platinizing (b) the electrodes

The steps involved in platinizing the probe electrodes are as follows:

1. Fill the glass beaker with chloroplatinic acid and install the platinum-foil and probe into the beaker.
2. Adjust the variable resistance to its maximum value and connect the electrodes as shown in Figure A1-b.
3. Adjust the variable resistor until the meter indicates a current of 3 milliamperes. Stir the fluid gently for 30 seconds and then remove the electrodes and immerse them in distilled water for a period of two hours before using them. When the platinized electrodes are not in use, they should be stored in distilled water.

Inadequate platinizing is indicated if the response of the probe is sluggish to rapid changes of concentration. If this is observed, wash the probe in distilled water and replatinize as described above. If after usage the probe becomes sluggish, then clean and platinize as described in the above procedures.

II. Preparation of the 15 Normal (15 N) Sulphuric Acid

Slowly pour one volume of concentrated (36 N) sulphuric acid into a 2.60 volumes of distilled water. Stir continuously while adding the concentrated sulphuric acid in order to avoid an explosion. The solution will get very hot as a consequence of the exothermix reaction.

III. Preparation of the Chloroplatinic Acid

Dissolve 1/8 oz. (3.45 g.) of chloroplatinic acid (platinic chloride crystal) and 20 mg. of lead acetate (crystal) in 100 cc. of distilled water. The platinic chloride crystals must not be exposed to air before use because they are very hygroscopic. Similarly, the prepared solution must be kept in a tightly closed container when not in use.